

<https://doi.org/10.15388/vu.thesis.510>
<https://orcid.org/0000-0001-6856-357X>

VILNIUS UNIVERSITY
CENTER FOR PHYSICAL SCIENCES AND TECHNOLOGY

Simona Pūkienė

Growth and Characterization of Bismide Alloys for Infrared Sensors

DOCTORAL DISSERTATION

Technological Sciences
Materials Engineering T 008

VILNIUS 2023

This dissertation was prepared between 2016 and 2022 in the Center for Physical Sciences and Technology. The research was supported by Research Council of Lithuania:
Scholarship – P-DAK-20-234.

Academic supervisor:

Dr. Renata Butkutė (Center for Physical Sciences and Technology, Technological Sciences, Materials Engineering – T 008).

Dissertation Defence Panel:

Chairman – Prof. Dr. Nerija Žurauskienė (Center for Physical Sciences and Technology, Technological Sciences, Materials Engineering – T 008);

Members:

Prof. Dr. Ramūnas Aleksiejūnas (Vilnius University, Natural Sciences, Physics – N 002);

Prof. Habil. Dr. Piotr Wojnar (Institute of Physics Polish Academy of Sciences, Technological Sciences, Materials Engineering – T 008);

Dr. Arūnas Kadys (Vilnius University, Technological Sciences, Materials Engineering – T 008);

Prof. Dr. Tomas Tamulevičius (Kaunas University of Technology, Technological Sciences, Materials Engineering – T 008).

The dissertation shall be defended at a public meeting of the Dissertation Defence Panel at 2 p.m. on 8th September 2023 in room A101 of the Center for Physical Sciences and Technology.

Address: Saulėtekio av. 3, A101, Vilnius, Lithuania. Tel. +37052648884;
e-mail: office@ftmc.lt.

The text of this dissertation can be accessed at the libraries of Center for Physical Sciences and Technology and Vilnius University, as well as on the website of Vilnius University:

www.vu.lt/lt/naujienos/ivykiukalendorius

<https://doi.org/10.15388/vu.thesis.510>
<https://orcid.org/0000-0001-6856-357X>

VILNIAUS UNIVERSITETAS
FIZINIŲ IR TECHNOLOGIJOS MOKSLŲ CENTRAS

Simona Pūkienė

Infraraudoniesiems jutikliams skirtų bismidinių junginių auginimas ir tyrimas

DAKTARO DISERTACIJA

Technologijos mokslai
Medžiagų inžinerija T 008

VILNIUS 2023

Disertacija rengta 2016–2022 metais Fizinių ir Technologijos mokslų centre. Mokslinius tyrimus rėmė Lietuvos mokslo taryba:
Stipendija – P-DAK-20-234.

Mokslinis vadovas:

dr. Renata Butkutė (Fizinių ir technologijos mokslų centras, technologijos mokslai, medžiagų inžinerija – T 008).

Gynimo taryba:

Pirmininkė – prof. dr. Nerija Žurauskienė (Fizinių ir technologijos mokslų centras, technologijos mokslai, medžiagų inžinerija – T 008).

Nariai:

prof. dr. Ramūnas Aleksiejūnas (Vilniaus universitetas, gamtos mokslai, fizika – N 002);

prof. habil. dr. Piotr Wojnar (Lenkijos mokslų akademijos Fizikos institutas, technologijos mokslai, medžiagų inžinerija – T 008);

dr. Arūnas Kadys (Vilniaus universitetas, technologijos mokslai, medžiagų inžinerija – T 008);

prof. dr. Tomas Tamulevičius (Kauno technologijos universitetas, technologijos mokslai, medžiagų inžinerija – T 008).

Disertacija ginama viešame Gynimo tarybos posėdyje 2023 m rugsėjo 8 d. 14 val. Fizinių ir technologijos mokslų centro A101 auditorijoje.
Adresas: Saulėtekio al. 3, Vilnius, tel. +37052648884; el. paštas: office@ftmc.lt .

Disertaciją galima peržiūrėti Fizinių ir technologijos mokslų centro bei VU bibliotekose ir VU interneto svetainėje adresu:
<https://www.vu.lt/naujienos/ivykiu-kalendorius>.

ACKNOWLEDGEMENT

First of all, I am grateful to my supervisor, Dr. Renata Butkutė, for her invaluable support. She taught me that science is interdisciplinary and helped developing my skills as an epitaxial growth specialist. Thank you for not only being a supervisor but also a friend, offering guidance and support through both joyful and challenging moments.

Secondly, I extend my gratitude to my colleagues who provided me with measurement results and shared valuable ideas and insights. Thank you for Prof. Eugenijus Gaubas for always checking on me .

I am also deeply thankful to my husband, Kornelijus, and my children, Albertas and Agota, for their immense patience and unwavering support throughout this journey.

Lastly, I am truly grateful to my mother Eugenija for her constant encouragement and support throughout this work.

LIST OF ABBREVIATIONS

AFM	Atomic Force Microscope
BEPR	Beam Equivalent Pressure Ratio
CB	Conduction Band
CW	Continuous wavelength
DC	Direct Current
DPSS	Diode Pumped Solid State laser
E_g	Band Gap
EL	Electroluminescence
IR	Infrared spectral range
FDS	Fractional-dimensional Space approach
FIB	Focused Ion Beam
HBT	Hetero-junction Bipolar Transistor
HR-XRD	High-resolution X-Ray Diffraction
IVBA	Inter-Valence Band Absorption
LD	Laser diode
LED	Light Emitting Diode
MBE	Molecular Beam Epitaxy
MCRW	Metal-Clad Ridge Waveguide
MIR	Mid-Infrared spectral range
MOCVD	Metal-Organic Chemical Vapor Deposition
MOVPE	Metal-Organic Vapour Phase Epitaxy
MQW	Multi-Quantum Well
NIR	Near-Infrared spectral range
PAAG	Pulsed analog alloy grading
PGB	Parabolically Graded Barrier
PL	Photoluminescence
PQW	Parabolic Quantum Well
QW	Quantum Well
RHEED	Reflection High Energy-Electron Diffraction
RMS	Root Mean Square
RSM	Reciprocal Space Mapping
RT	Room Temperature
RTPL	Room Temperature Photoluminescence

RQW	Rectangular Quantum Well
SEM	Scanning Electron Microscopy
SI	Semi-Insulating
SQW	Single-Quantum Well
STEM	Scanning Transmission Electron Microscopy
TEM	Transmission Electron Microscopy
TST	Two Substrate Temperature method
UHV	Ultra-High Vacuum
UV	Ultraviolet spectral range
VB	Valence Band
VBA	Valence Band Anticrossing
Δ_{so}	Spin-Orbit Splitting Energy

TABLE OF CONTENTS

1	INTRODUCTION	11
	Objectives of research	12
	Relevance and scientific novelty	13
	Statements in defence	14
	Author's contribution	14
	Publications	15
2	PROPERTIES AND APPLICATION OF GaAsBi ALLOYS	19
2.1	Investigations of III-V-Bi semiconductor alloys	19
2.2	Properties of GaAsBi alloys	21
2.2.1	Band-gap engineering	21
2.2.2	The Valence Band Anti-Crossing model	22
2.2.3	Localisation effect	24
2.3	Growth of GaAsBi	26
2.3.1	Bi as a surfactant	26
2.3.2	Bi surface droplets	27
2.3.3	GaAsBi growth models	29
2.3.4	Influence of growth parameters	32
2.4	Compound semiconductors for optoelectronic applications	37
2.4.1	Lasers and LEDs	37
3	MBE GROWTH AND CHARACTERIZATION TECHNIQUES	42
3.1	MBE technique	42
3.1.1	The employed MBE system	43
3.1.1.1	SVT-C-V-2 instrumentation	44
3.1.1.2	Veeco GENxplor R&D instrument	45
3.1.2	Substrate preparation	46
3.1.3	Procedures of the GaAsBi growth	47
3.2	Techniques for the <i>in situ</i> monitoring	47
3.2.1	Surface and growth rate control by RHEED technique	47
3.2.2	Beam flux measurement	49
3.3	Techniques of the <i>ex situ</i> characterisation	50

3.3.1	High-resolution X-ray diffraction	50
3.3.2	Atomic force microscopy	51
3.3.3	Scanning transmission electron microscopy	52
3.3.4	Photoluminescence spectroscopy	53
3.3.5	Electroluminescence spectroscopy	54
3.3.6	Measurements of voltamperic characteristics	55
4	RESULTS ON GROWTH OF 100 NM GaAsBi/GaAs HETEROSTRUCTURES	56
4.1	Growth of heterostructures	56
4.2	Results and discussion	59
4.2.1	Structure analysis	59
4.2.2	Optical characteristics	68
4.3	Conclusions of the chapter	69
5	GROWTH AND CHARACTERIZATION OF THE QW GaAsBi/(Al)GaAs STRUCTURES	71
5.1	Growth and analysis of the rectangular GaAsBi quantum well structures	71
5.1.1	Photoluminescence characteristics of rectangular GaAsBi QWs	74
5.2	Growth and analysis of parabolic GaAsBi quantum well structures	77
5.2.1	Parabolic quantum wells	77
5.2.1.1	Growth of the AlGaAs/GaAs parabolic quantum wells	79
5.2.1.2	Growth of the parabolic GaAsBi quantum wells	84
5.2.2	Characteristics of the parabolic GaAsBi QWs	88
5.2.2.1	STEM imaging	88
5.2.2.2	Morphology characterisation	88
5.3	Comparison of QW structure characteristics with different barrier design	93
5.3.1	Characteristics of the room temperature photoluminescence	94
5.3.2	Temperature and excitation power dependent photoluminescence	96

5.4	Modeling of the main characteristics	100
5.5	Conclusions for the chapter	104
6	GAASBI/GAAS BASED NEAR-INFRARED EMITTING QUANTUM DEVICES	105
6.1	Growth and fabrication of laser diode structures	105
6.1.1	Growth of laser diode structures	105
6.1.2	Fabrication of laser diodes	108
6.2	Characterization of the fabricated laser diode structures .	112
6.3	Conclusions for the chapter	116
7	CONCLUSIONS OF THE STUDY	118
8	SANTRAUKA	120
	Author's contribution	123
8.1	GaAsBi apžvalga	126
8.2	Eksperimentinės metodikos	126
8.3	Pagrindiniai rezultatai ir apibendrinimas	127
8.3.1	100 nm GaAsBi epitaksinių sluoksnių auginimo sąlygos ir rezultatai	127
8.3.2	GaAsBi/GaAs kvantinių duobių auginimo sąlygos ir rezultatai	132
8.3.3	GaAsBi/GaAs NIR lazeriniai diodai	137
8.4	Pagrindiniai rezultatai ir išvados	139
	REFERENCES	141
9	CURRICULUM VITAE	157

1. INTRODUCTION

The infrared spectral range (IR) has gained significant importance and attractiveness for various applications due to the absorption or emission bands related to the vibrational properties of different organic molecules. However, commercially available detectors integrated into these systems lack sufficient sensitivity. Laser diodes (LD) and light emitting diodes (LED) are hindered by losses caused by Auger non-radiative recombination and the temperature sensitivity of the radiation wavelength. While a significant number of publications concentrate on fabricating and studying devices operating in the mid-infrared (MIR) (where the absorption of molecules is more pronounced), commercially available devices suitable for integration into sensing systems lack sufficient sensitivity. In contrast, devices operating in the near-infrared (NIR) exhibit more desirable characteristics, with sensitivity magnitudes that are a hundred times higher. Moreover, NIR radiation is safe for the human body and enables spectroscopic investigations for assessing skin tissue, blood analyses, glucose, oxygen, and hemoglobin concentration. The importance of fulfill the requirements for the devices is crucial due to the increasing use of noninvasive preventive medical, chemical, and biological sensors that utilize light to stimulate molecules [1–3]. Scientists continually seek new methods to enhance the characteristics of infrared sensors, aiming for improved parameter stability, extended lifetimes, and expanded application possibilities. Thus, the development of IR emitters and detectors is still relevant and the engineering of new materials suitable for the production of these IR devices is necessary.

A significant progress has been made in the development of growth technology for GaAsBi quantum structures, which have the potential

for various optoelectronic applications, including lasers [4, 5], light-emitting diodes [6], photodetectors [7], spintronic devices [8] and solar cells [9]. Bismides have attracted significant attention because of their unique physical properties, such as a large band-gap (E_g) reduction, spin-orbit splitting, and lower temperature sensitivity compared to traditional III-V semiconductor band-gap [10–12]. It was found that E_g value of GaAsBi alloy decreases up to 90 meV per 1% of Bi [8, 10, 26, 43]. It is expected that applying of dilute bismide alloys in the formation of an active area of devices enables fabrication of the efficient laser diodes for the range of long wavelengths. The GaAs_{0.975}Bi_{0.025} laser, realized for the first time by photo-pumping, fabricated using bulk material grown by molecular beam epitaxy (MBE), was proposed by Tominaga *et al.* in 2010 [4]. Additionally, the first successful operation of a GaAs_{0.978}Bi_{0.022} single quantum well (SQW) laser, fabricated using material grown by metal-organic chemical vapor deposition (MOCVD), was reported by Ludewig *et al.* in 2013 [5], while Butkutė *et al.* reported electrically driven lasing from the GaAsBi multi quantum well (MQW) diode, grown by MBE with 6% of Bi, in 2014 [13].

The challenges outlined above require the development of GaAsBi alloys and the investigation of a wide range of parameters to modify the properties of advanced materials. This dissertation focuses on optimization of growth conditions using MBE. The study includes the analysis of 100 nm thick GaAsBi epitaxial layers with ultra-thin GaAs buffers. This research concentrates on investigating the impact of material composition and quantum structure geometry on optical properties. The developed novelties include the parabolic analog alloy grading technique, which has been proven to be a powerful tool for enhancing the optical properties of quantum structures and establishing a basis for GaAsBi laser diodes designed for the NIR wavelength range.

Objectives of research

The aim of this research is the development of III-V-Bi nanostructure-based MBE growth technology on the GaAs platform. This includes analyzing the impact of material composition and architecture on

the epitaxy and properties of quantum structures. The research also focuses on the development of infrared laser diode technology. A comprehensive study of bismide quantum nanostructures and epitaxial layers is carried out to reveal critical technological growth parameters. To achieve this objective, the following tasks were undertaken:

1. Development of technology for growth of 100 nm GaAsBi layers on GaAs substrates using the molecular beam epitaxy technique. Experimental investigation of the structural and optical properties of the 100 nm GaAsBi layers.
2. Development of growth technology of GaAsBi quantum well (QW) structures using various designs of quantum wells: single and/or multiple rectangular (RQW), step-like and parabolic (PQW) quantum wells. Investigation of the analog alloy grading technique implementation for PQW formation.
3. Development of the laser diode growth technology using AlGaAs and GaAsBi active regions, enabling operation in the spectral range of 780 – 830 nm and 1000 – 1100 nm, respectively.
4. Fabrication and characterization of GaAsBi and AlGaAs QWs-based laser diodes using different type of active region design.

Relevance and scientific novelty

This thesis presents a comprehensive study on the molecular beam epitaxy growth of GaAsBi layers and quantum structures on GaAs substrates. The study focuses on optimizing the growth parameters to control the structural and optical properties of the material. The research successfully identifies the optimal growth conditions of almost fully strained 100 nm thick GaAsBi epitaxial layers with up to 10% Bi concentration, which can be used for the fabrication of GaAsBi detectors operating in the range of about 1 – 1.5 μm .

Extensive research has been carried out in the demonstration of using the analog alloy grading technique for growing PQW GaAsBi structures. It has been shown that the PQW GaAsBi structures exhibit more than 50 times increase in photoluminescence intensity compared

to the RQW GaAsBi structures. This study has also established the optimal growth parameters for parabolic quantum well formation both AlGaAs and GaAsBi-based laser diodes. A laser diode with parabolic graded QW GaAsBi active area has been demonstrated for the first time.

Statements

The statements to defend:

1. The 100 nm thick GaAsBi layers containing 2–8% of Bi, grown under stoichiometric conditions on ultra-thin GaAs buffer (up to 20 nm), exhibit an insignificant relaxation of about 0.5 – 3%.
2. The analog alloy grading technique is promising for the implementation of a parabolic GaAsBi quantum well potential profile. A graded AlGaAs barrier can be achieved by varying the Al source temperature while keeping the Ga source temperature constant.
3. The application of parabolic quantum well design in the active area of a laser diodes allows for a reduction in the quantum well number, therefore lowering the threshold current density.

Author's contribution

The author performed all the MBE growth procedures, including substrate preparation, growth monitoring, and structure formation. The author also assisted in most of the measurements for material characterization, data analysis, and the interpretation of results. The author implemented the experimental data analysis and carried out the primary preparation of scientific publications. The author presented the research findings at conferences, either through oral or poster sessions. All the non-original work was appropriately referenced.

The results presented in Chapter 4 has also been published in article of **S. Pūkienė**, A. Jasinskas, A. Zelioli, S. Stanionytė, V. Bukauskas, B. Čechavičius, E. Dudutienė, R. Butkutė, Influence of an ultra-thin buffer layer on the growth and properties of pseudomorphic GaAsBi layers, Lithuanian Journal of Physics, **62**, 93 (2022).

The results presented in Chapter 5 has also been published in article of **S. Pūkienė**, M. Karaliūnas, A. Jasinskas, E. Dudutienė, B. Čechavičius, J. Devenson, R. Butkutė, A. Udal and G. Valušis Enhancement of photoluminescence of GaAsBi quantum wells by parabolic design of AlGaAs barriers, *Nanotechnology*, **30**, 455001 (2019) and M. Karaliūnas, E. Dudutienė, A. Čerškus, J. Pagalys, **S. Pūkienė**, A. Udal R. Butkutė, G. Valušis, High precision parabolic quantum wells grown using pulsed analog alloy grading technique: Photoluminescence probing and fractional-dimensional space approach, *Journal of Luminescence*, **239**, 118321 (2021). The results from this article can be found in E. Dudutienė's dissertation. It is important to highlight that the author's contribution to these paper are the MBE processes, specifically using the analog alloy grading method for the growth of quantum wells. E. Dudutienė performed optical measurements and analyzed the photoluminescence results in her thesis.

The results presented in Chapter 6 has additionally been published as article of S. Armalytė, J. Glemža, V. Jonkus, S. Pralgauskaitė, J. Matukas, **S. Pūkienė**, A. Zelioli, E. Dudutienė, A. Naujokaitis, A. Bičiūnas and R. Butkutė Low-Frequency Noise Characteristics of (Al, Ga)As and Ga(As, Bi) Quantum Well Structures for NIR Laser Diodes, *Sensors*, **23**, 2282 (2023) and J. Glemža, S. Pralgauskaitė, J. Matukas, **S. Pūkienė**, A. Zelioli, A. Bičiūnas, B. Čechavičius, V. Nargelienė and R. Butkutė Low frequency noise study for developing of AlGaAs and GaAsBi QW structures for NIR LDs , *IEEE Xplore: 24th International Microwave and Radar Conference (MIKON)*, Gdansk, Poland, 2022, pp. 1-4.

Publications

The main results of this study have been published in 5 scientific articles and presented personally at 12 national and international conferences and schools for PhD students. The author was also a co-author of more than 30 other conference papers. Publications are listed below:

Publications

- P1 **S. Pūkienė**, M. Karaliūnas, A. Jasinskas, E. Dudutienė, B. Čechavičius, J. Devenson, R. Butkutė, A. Udal, G. Valušis, Enhancement of photoluminescence of GaAsBi quantum wells by parabolic design of AlGaAs barriers, *Nanotechnology*, **30** 455001 (2019).
- P2 M. Karaliūnas, E. Dudutienė, A. Čerškus, J. Pagalys, **S. Pūkienė**, A. Udal R. Butkutė, G. Valušis, High precision parabolic quantum wells grown using pulsed analog alloy grading technique: Photoluminescence probing and fractional-dimensional space approach, *Journal of Luminescence*, **239**, 118321 (2021).
- P3 **S. Pūkienė**, A. Jasinskas, A. Zelioli, S. Stanionytė, V. Bukauskas, B. Čechavičius, E. Dudutienė, R. Butkutė, Influence of an ultrathin buffer layer on the growth and properties of pseudomorphic GaAsBi layers, *Lithuanian Journal of Physics*, **62**, 93 (2022).
- P4 J. Glemža, S. Pralgauskaitė, J. Matukas, **S. Pūkienė**, A. Zelioli, A. Bičiūnas, B. Čechavičius, V. Nargelienė and R. Butkutė Low frequency noise study for developing of AlGaAs and GaAsBi QW structures for NIR LDs , *IEEE Xplore: 24th International Microwave and Radar Conference (MIKON)*, Gdansk, Poland, 2022, pp. 1-4.
- P5 S. Armalytė, J. Glemža, V. Jonkus, S. Pralgauskaitė, J. Matukas, **S. Pūkienė**, A. Zelioli, E. Dudutienė, A. Naujokaitis, A. Bičiūnas and R. Butkutė Low-Frequency Noise Characteristics of (Al, Ga)As and Ga(As, Bi) Quantum Well Structures for NIR Laser Diodes, *Sensors*, **23**, 2282 (2023)

Presentations at conferences and PhD schools:

- C1 **S. Pūkienė**, A. Jasinskas, S. Stanionytė, B. Čechavičius, R. Butkutė, A. Krotkus. Thick Epitaxial GaAsBi Layers for Infrared Components, *Advanced Materials and Technologies 2018*, 27-31 August, Palanga.

- C2 **S. Pūkienė**, A. Jasinskas, S. Stanionytė, B. Čechavičius, S. Tumėnas, E. Pozingytė, J. Devenson, R. Norkus, R. Butkutė, A. Krotkus. Thick epitaxial GaAsBi layers for infrared components, APROPOS – 16, Vilnius, Lietuva, 2018 m. spalio 10-12 d.
- C3 **S. Pūkienė**, A. Jasinskas, S. Stanionytė, B. Čechavičius, E. Pozingytė, R. Butkutė. GaAsBi sluoksnių auginimo ypatumai; FizTech 2018 spalio 17-18, Vilnius.
- C4 **S. Pūkienė**, B. Čechavičius, J. Devenson, R. Butkutė, Different QW structures with Bi for infrared-emitting semiconductor lasers, 62nd Scientific Conference for Students of Physics and Natural Sciences Open Readings 2019 (Vilnius, 2019), (Vilnius University, 2019).
- C5 **S. Pūkienė**, M. Karaliūnas, A. Jasinskas, E. Dudutienė, B. Čechavičius, A. Udal, G. Valušis R. Butkutė, A3-B5 QW structures with Bi for IR range optoelectronic devices, Advanced Materials and Technologies 2019, 19-23 August, Palanga.
- C6 **S. Pūkienė**, J. Devenson, V. Agafonov, A. Jasinskas, E. Dudutienė, B. Čechavičius, K. Stašys and R. Butkutė; Low-power, temperature-resistant IR range semiconductor laser diodes for automotive applications; in Frontiers in Optics + Laser Science APS/DLS, OSA Technical Digest (Optica Publishing Group, 2019), paper JTu3A.13.
- C7 **S. Pūkienė**, A. Jasinskas, V. Bukauskas, V. Agafonov, M. Kamarauskas, A. Bičiūnas, B. Čechavičius, A. Šetkus, R. Butkutė; Near IR light emitting sources electro-optical characteristics 63rd Scientific Conference for Students of Physics and Natural Sciences Open Readings 2020 (Vilnius, 2020).
- C8 **S. Pūkienė**, A. Jasinskas, V. Bukauskas, V. Agafonov, M. Kamarauskas, A. Lukša, A. Bičiūnas, B. Čechavičius, A. Šetkus, R. Butkutė; Electro-optical response of near-infrared light emitting sources; Advanced Materials and Technologies 2020, 24-28 August, Palanga. (Best presentation award).

- C9 **S. Pūkienė**, A. Jasinskas, V. Bukauskas, V. Agafonov, M. Kamarauskas, A. Lukša, A. Bičiūnas, B. Čechavičius, A. Šetkus, R. Butkutė; Electro-optical Characteristics of NIR Light Emitting Sources for High Resolution Sensing Systems; in *Frontiers in Optics + Laser Science APS/DLS, The Optical Society (Optical Society of America, 2020) Virtual USA*.
- C10 **S. Pūkienė**, A. Jasinskas, V. Bukauskas, V. Agafonov, M. Kamarauskas, A. Lukša, A. Bičiūnas, B. Čechavičius, A. Šetkus and R. Butkutė; A3-B5 QW structures for IR range optoelectronic devices; APROPOS – 17, Vilnius, Lithuania, 2020 m. 30 September – 1 October.
- C11 **S. Pūkienė**, A. Jasinskas, V. Bukauskas, V. Agafonov, M. Kamarauskas, A. Lukša, A. Bičiūnas, B. Čechavičius, A. Šetkus, R. Butkutė; Influence of A3-B5 QW structures on parameters of NIR light emitting devices; FizTech 2020 22-23 October, Vilnius.
- C12 **S. Pūkienė**, A. Jasinskas, V. Bukauskas, V. Agafonov, M. Kamarauskas, A. Lukša, A. Bičiūnas, B. Čechavičius, A. Šetkus, R. Butkutė; Electro-optical characteristics of NIR light emitting sources; Functional Materials and Nanotechnologies; FM&NT 23-26 November 2020, Virtual Vilnius.

2. PROPERTIES AND APPLICATION OF GAsBi ALLOYS

2.1 Investigations of III-V-Bi semiconductor alloys

The research on III-V-Bi alloys dates back to 1969 when the first study on InSbBi structures was published [14, 15]. This study was motivated by the interest in the semi-metallic behaviour of InBi, which allowed InSbBi to cover the 8 – 14 μm infrared spectral range. Initially, the InSbBi alloy was grown using bulk growth techniques. It has been shown that incorporation of bismuth (Bi) into InSb lattice reduced the band-gap of material by 36 meV per percent of Bi [14]. Later, successful growth of $\text{InAs}_{1-x}\text{Bi}_x$ with Bi composition larger than 2.6% was demonstrated by Oe *et al.* [16]. Photoluminescence (PL) spectroscopy showed a peak intensity at 10 K. Also a band-gap reduction of 55 meV/% Bi in InAsBi was unveiled [16]. The solubility of InBi in InSb is limited to 2.6% [15]. This poses a challenge for the growth of alloy structures using pulling methods like the Czochralski method. The most relevant growth techniques for InSbBi, InAsBi, and InAsSbBi fabrication appeared to be molecular beam epitaxy and metal-organic vapor-phase epitaxy (MOVPE) [16–19]. However, the research has shown that incorporation of Bi into III-V group compounds during epitaxial growth by MBE or MOVPE might be challenging. The limitations are due to the low growth temperature and surface coverage of InBi and InBi_2 droplets [16–20]. The prospects of III-V-Bi structures in fabricating the telecommunication range laser diodes are determined by the nearly temperature-insensitive band-gap characteristics of these materials [21]. However, Oe and Asai noted that the most challenging

aspect would be finding the material suitable for the active region with a band-gap insensitive to temperature fluctuations [22]. Oe and Asai suggested [22] the InGaAsBi alloy as the most suitable material for this purpose.

InGaAsBi structures on InP substrates have been investigated in order to extend emission wavelengths beyond those achievable using InGaAs alloys grown on InP [23, 24]. GaSbBi has also been researched [25]. In the 1970-90s, the dilute bismide alloys such as InSbBi and InAsSbBi were researched addressing to applications of the MIR spectral range photodetectors. After the discovery of the giant energy bowing effect in GaAsBi [26], it was realized that Bi incorporation could effectively reduce the band-gap of GaAsBi and increase the valence-band (VB) offset of GaAsBi/GaAs. The Japanese scientist group revealed that the temperature coefficient of the band-gap ($\Delta E_g/\Delta T$) variations in GaAsBi comprises about 1/3 of that in GaAs [11, 21, 27]. However, this finding was not confirmed in other publications. There it was found that the temperature coefficient of the band-gap variations is essentially the same as that for GaAs [10, 28]. This discrepancy might be explained by the role of the localised states near the top of the VB associated with Bi alloying [28, 29].

GaAsBi with 2% Bi was first grown in 1998 by MOCVD by Oe *et al.* [21]. This material was later grown by MBE technique in Canada, and in Japan, [26, 30]. Oe *et al.* investigated the PL spectra of these materials and observed that the temperature dependent shift of the spectral peak was relatively small: 0.1 meV/K [21]. Problems with metallic surface droplets were encountered of GaAsBi alloys during the growth.

Higher bismuth fractions ($> 10\%$) have been achieved when MBE growth is performed using a rather low operating temperature of 200 °C [31, 32]. A study of the band-gap and optical absorption edge of GaAsBi, grown by MBE with 17.8% Bi, has been reported [33]. Furthermore, a demonstration of 22% Bi fraction has been made [34]; however, the latter samples suffered from metallic droplets on the surface and did not exhibit good structural quality.

The quality of the surface is a crucial factor in the performance of light-emitting devices.

2.2 Properties of GaAsBi alloys

The III-V-Bi compound semiconductors are important for optoelectronic applications due to their properties such as direct band-gap, the enhanced spin-orbit splitting energy (Δ_{SO}). These compound materials exhibit the reduced non-radiative Auger recombination. The GaAsBi alloys are the most important III-V compound semiconductors that have been extensively studied for applications in production of solid state lasers, LEDs, solar cells, photodetectors, biosensors, and etc. [35–37].

2.2.1 Band-gap engineering

The material band-gap engineering is the most important procedure in the design of photo-electronic devices. The incorporation of Bi into the GaAs lattice results in a reduction of the band-gap by approximately 83 meV/%Bi [10]. This reduction is much higher than the one obtained by introducing In or Sb (11 meV/% In [38], 19 meV/% Sb [39]). However, Bi incorporation leads to a smaller effect than the one obtained when N is incorporated (125 meV/% N [40]). Figure 2.1 illustrates the band-gap energy variations as a function of lattice constant for III-V semiconductors within the range of 5.6 – 6.5 Å of lattice constants. A NIR light-emitting device intended for the 1.31 – 1.55 μm wavelength spectral range needs a material with a band-gap energy of values between 0.95 – 0.8 eV. Figure 2.1 shows the III-V materials that fit the mentioned E_g range, where the ternary alloys are implied using connections of the binary material points. The blue and red lines represent experimental data attributed to GaAsBi [40] and GaAsN [32] alloys, respectively. Although the GaBi compound has never been synthesized, it can be predicted as having a negative band-gap value of -1.45 eV [41].

From Figure 2.1, it is evident that incorporating of Bi into GaAs lattice leads to a reduction in the band-gap values. This highlights the potential of bismide alloys to engineer a wide range of band-gap values ($0 < E_g < 1.42$ eV) when using the GaAs substrates with small strain.

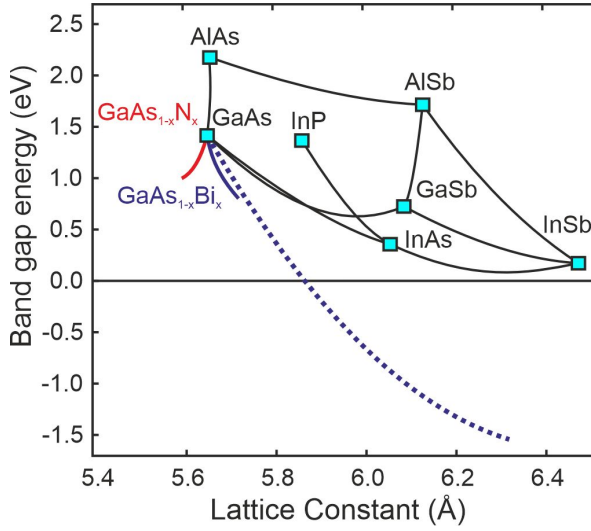


Figure 2.1 Band-gap energy as a function of lattice constant for the III-V compound semiconductors. Results are adopted from [41].

2.2.2 The Valence Band Anti-Crossing model

The observed non-linear decrease in E_g with enhancement of bismuth content in GaAs is significant. The reported values of the band-gap reduction vary in the range from 42 meV/% [42] through 88 meV/% [11] up to 90 meV/% [8,10,26,43]. The obtained band-gap modification by Bi incorporation makes bismide alloys highly attractive for use in devices that operate in the near- or mid-infrared wavelength range.

The nonlinear behaviour of E_g in GaAsBi, similar to that observed in dilute nitrides, was first demonstrated and explained by Shan *et al.* [44]. In GaInNAs compounds, the peculiarities of the conduction band (CB) structure are attributed to the differences in the atomic radius of nitrogen and arsenic atoms. Alberi *et al.* applied this model to GaAsBi and proposed that the band-gap structure is determined by a difference in the atomic radius of Bi and As atoms. However, the valence band anticrossing (VBA) model is often used to describe the composition-dependent band-gap in highly mismatched alloys such as GaAsN and GaAsBi. The VBA model is valid only for small concentrations of bismuth when Bi is considered an isoelectric impurity [43]. This model includes interaction between the edge states either of the conduction or valence band.

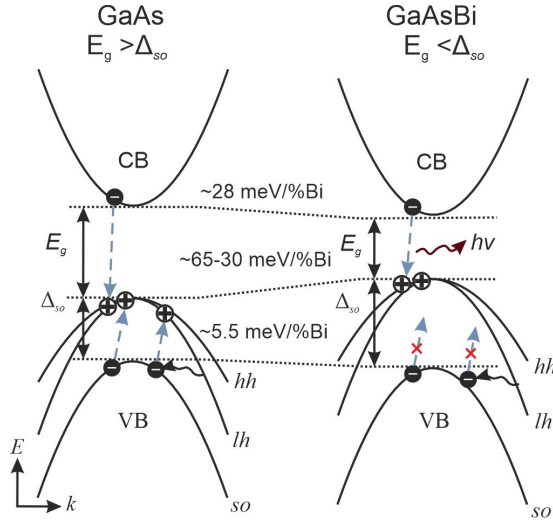


Figure 2.2 The band structure of GaAs and GaAsBi schematically shows the Auger, CHSH, and IVBA non-radiative recombination channels. The schemes are adopted from reference [45].

Bi is the largest atom in the V element group and has the largest spin-orbit energy splitting [46]. III-V-Bi structures can be used in production of the high-temperature devices, such as semiconductor lasers. These applications are based on the material narrow band-gap and large spin-orbit splitting. The Auger recombination processes can be eliminated when Δ_{SO} is larger than E_g in III-V-Bi structures. Auger recombination is a non-radiative process that occurs when the energy and momentum from an electron-hole pair is transmitted to the secondary electron or hole. The latter is subsequently excited into spin-orbit split-off states, as sketched in Figure 2.2. The additional charge carriers are thereby generated by Auger recombination those heat up the lattice during relaxation. Lattice heating degrades the performance of light-emitting devices by increasing the threshold current density and decreasing the internal quantum efficiency. In materials with relatively high bismuth concentrations (above 10% Bi) and a spin-orbit splitting of states greater than the band-gap energy, inter-valence band absorption (IVBA) and Auger recombination might be eliminated [47, 48]. The large spin-orbit splitting in Bi-containing materials can be useful in spintronic devices, as well.

The calculated values of E_g and Δ_{SO} are illustrated in Figure 2.3 as a

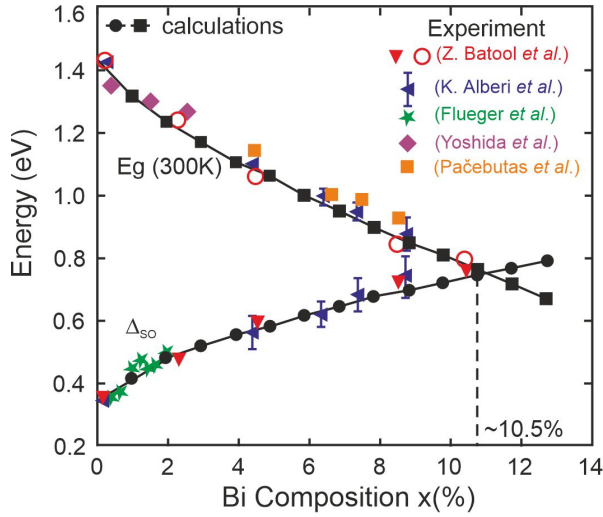


Figure 2.3 Band-gap and spin-orbit splitting energy values as a function of Bi concentration in GaAsBi materials. Adopted from Ref. [45].

function of Bi content [45]. These E_g and Δ_{SO} values are shown along with experimental data from various research groups [8, 11, 43, 49]. The results of both theoretical and experimental studies demonstrate a crossover of E_g and Δ_{SO} at approximately 10.5% Bi concentration.

Studies of the electron transport properties of the bismide alloys revealed that the incorporation of Bi does not strongly affect electron mobility [9,50], unlike to N incorporation. This makes Bi a promising candidate for use in low threshold voltage heterojunction bipolar transistors (HBTs). A significant power consumption reduction can be achieved by reducing the turn-on voltage of HBTs.

2.2.3 Localisation effect

The large difference between Bi and As atomic radius determines the optical and structural properties of GaAsBi materials. The short-range disordered alloys can be synthesized by non-traditional GaAsBi growth conditions. This disordering effect is visible due to the interaction of carriers on light-hole band edge states with those on Bi energy levels [51]. Short-range alloy disorder is characterized by microscopic fluctuations in the GaAsBi layer across the growth direction, which results in non-uniform perturbations to the lattice's periodic potential. This leads to

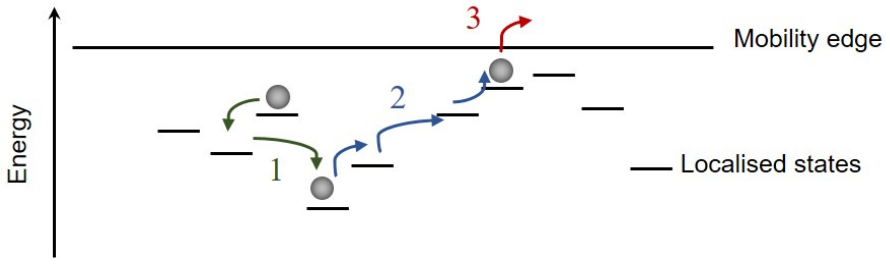


Figure 2.4 The hopping of excitons between localised states due to thermal excitation: 1 – excitons trapped by deeper level localised states; 2 – blue-shift is observed; 3 – excitons are delocalised.

the formation of localised energy states related to the band-gap and formed below the mobility edge.

In literature, the short-range disorder in GaAsBi is considered as the S-shape (red-blue-red shift) temperature-dependent PL spectral variations [52–55]. Gogineni *et al.* suggested that the localised states exhibit an exponential distribution. Therefore, the PL spectra show an Urbach tail inherent variations, due to the extension of the localised states [56]. Imhof *et al.* modeled the PL of GaAsBi by analyzing the behaviour of the localised states with exponential and Gaussian distributions on two energy scales [52]. Shafka *et al.* also reported that a combination of exponential and Gaussian distributions can be employed to explain and describe the GaAsBi PL quenching effects [57]. Wilson *et al.* performed various temperature-dependent PL measurements under different excitation conditions to investigate the nature of the localised states in GaAsBi [58].

Routinely, the GaAsBi PL spectra exhibit the S-shape temperature dependent spectral variations. The exciton localisation at low temperatures is there inferred particularly at lower excitation levels. The S-shape spectral variations can be characterized by three main phases, illustrated in Fig. 2.4. First, at extremely low-temperature (10 K) electron-hole pairs are located at a local energy minimum. Due to the low temperature, carriers undergo a rather small thermal excitation and remain trapped until they recombine. In the range of relatively elevated temperatures (of $> 10 - 80$ K), the red-shift of the PL spectral band is observed, and excitons gain enough thermal energy to escape

and become trapped by deeper localised states (1 step). Further (2 step), the PL band blue-shift is observed in the range of 80 – 150 K when thermal energy mobilizes previously localised excitons. These excited excitons are able to make multiple hops between the states. The excitons become delocalised and excess carriers have enough thermal energy to distribute themselves randomly for temperature range of > 150 K. This leads to the PL band red-shift. The considered PL variations are determined by the temperature-dependent band-gap changes (3 step).

The Varshni equation describes the temperature-dependent band-gap variation as:

$$E_g(T) = E_0 - \frac{\alpha T^2}{T + \beta}. \quad (2.1)$$

Here α and β are the fitting parameters and E_0 is the band-gap energy at 0 K temperature. For the band-tail states, a deviation from Varshni's law appears. This deviation is related to charge carriers localisation. The equation 2.1 is then modified to:

$$E_g(T) = E_0 - \frac{\alpha T^2}{T + \beta} \frac{\sigma^2}{kT}, \quad (2.2)$$

where σ is the localisation parameter.

In this way, the localisation of charge carriers can be quantified by analysis of interactions of the localised carriers with the non-radiative recombination centres. This results in the decrease of the localisation probability while the probability of non-radiative recombination increases. The extent of the localisation is determined by the MBE growth conditions [55].

2.3 Growth of GaAsBi

2.3.1 Bi as a surfactant

The distribution of Bi in GaAsBi is non-uniform, and fluctuations, clusters, or droplets may be observed. Norman *et al.* theoretically predicted a weak Ga-Bi bonding. Therefore, phase segregation leads to anisotropic structures [59]. Transmission electron microscopy (TEM) images, considered by Luna *et al.*, demonstrate quasi-periodical nano-

columns of Bi atoms along the growth direction [60]. Furthermore, Wu *et al.* employed TEM images to observe segregation during annealing and found Bi clusters [60].

As a surfactant, bismuth atoms can smooth the surface. This improves the coherence of the GaAs matrix and interfaces heterostructure during layer growth. Due to large size, bismuth atoms increase surface tension [61] and enhance adatom diffusion [62]. This determines Bi suitability to be a surfactant in III-V alloy growth. Thereby, Bi, acting as a surfactant, might lead to a reduction of point defect and impurity density in GaAs, consequently decreasing the non-radiative recombination. However, the incorporation of Bi is usually non-uniform, resulting in a broad PL spectra.

2.3.2 Bi surface droplets

The incorporation of even a small amount of Bi into the GaAs lattice causes a significant lattice perturbation. Low growth temperature and reduced As flux is necessary to prevent bismuth evaporating and to ensure Bi incorporation, due to weak Ga-Bi bonding energy. Bi atoms tend to segregate onto the GaAsBi surface at high temperatures forming bismuth droplets. The excess Bi atoms can diffuse on the layer surface. This also leads to droplet formation, as sketched in Figure 2.5. Too low As flux additionally enhances the probability of Ga droplet formation. Therefore, it is crucial to control the As and Bi flux ratio in order to grow the droplet-free GaAsBi.

The behaviour of Bi atoms during the MBE process depends on growth parameters such as As/Ga flux ratio, growth temperature, and growth rate. Any changes in these parameter values can affect the crystal morphology and surface of the resulting structure. Figure 2.5 illustrates the possible processes of Bi incorporation during the GaAsBi growth. There are three main processes: (1) the desorption when Bi atoms might evaporate from the surface, (2) Bi droplet formation due to adsorbed Bi diffusion across the layer surface, and (3) GaAsBi alloy growth when Bi atoms are appropriately incorporated into GaAs lattice. The incorporated Bi atoms also can additionally be ejected onto the layer surface, although, remaining adsorbed (4). Breaking of the

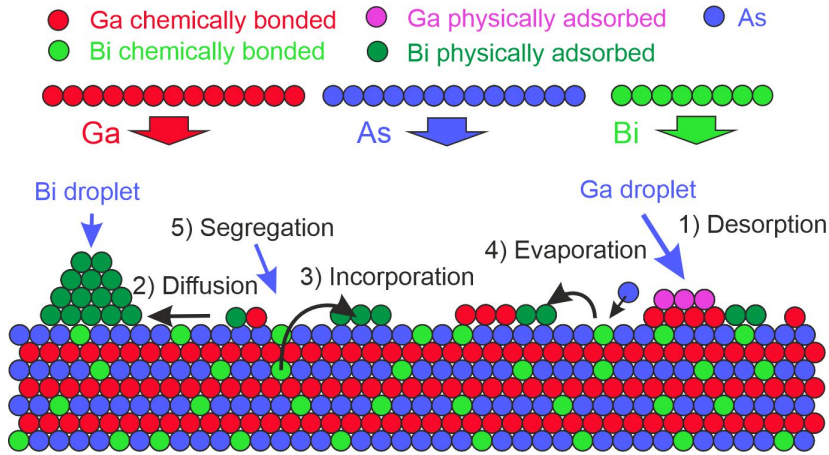


Figure 2.5 Schematic illustration of processes of Bi atoms incorporating into GaAs lattice [63].

Ga-Bi bonds due to thermal activation may lead to surface structure segregation (5).

Bi atoms on GaAs also lower the crystal surface energy, acting through the surfactant effect, where weak van der Waals bonding ensures easier Bi surface diffusion. Metallic Bi droplets can form on the layer surface when a big amount of Bi is incorporated. This droplet formation is a thermodynamically driven process that can be controlled by manipulating the MBE growth parameters. The formation of droplets also depends on film thickness. Therefore, the growth of droplet-free GaAsBi QWs appears to be more advantageous than depositing GaAsBi films. Growth parameters, such as growth temperature, the Ga/As beam equivalent pressure ratio (BEPR), and growth rate strongly impact the droplet formation. At low growth temperatures, Bi droplets tend to distribute inhomogeneously on the surface due to weak atom diffusion. While high-temperature annealing can be applied to remove droplets through enhanced evaporation of Bi [64]. Ptak *et al.* demonstrated [65] that growth rate also strongly affects droplet formation when surface diffusion of Bi is facilitated by either high Bi flux or high growth temperature. Droplet formation can be suppressed by applying either high As flux or low growth temperature. Krotkus *et al.* successfully formed the droplet-free surfaces of GaAsBi films by capping Be-doped GaAs on GaAsBi [66].

This growth technology is based on small atomic radius of Be which compensates for the large atomic size of Bi.

There is also a probability for the ejection of Bi atoms from the bulk crystal to the layer surface. This is caused by the As-Bi exchange during GaAsBi growth. As-Ga binding is stronger within GaAs crystal than Bi-Ga in GaAsBi material. Therefore, the As atoms replace the incorporated Bi. Alternatively, the accumulated strain in GaAsBi and the Bi surfactant effect lead to the occupation of the lower energy states by the incorporated Bi atoms. Ciatto *et al.* demonstrated [67] that Bi droplet formation depends on the incorporated Bi content. In structures with Bi content lower than 3%, a rather homogeneous droplet formation is obtained. While, in the case of Bi content above 5.4%, the random distribution of Bi droplets appears on the sample surface.

2.3.3 GaAsBi growth models

Bi atoms are larger than As and Ga atoms. Therefore, bismuth tends to segregate towards the surface during GaAsBi growth. Generally, under typical GaAs growth conditions: As/Ga ratio at 7:1 and growth temperature at 580 °C, the incorporation of bismuth into the GaAs lattice is negligible. In early research made on GaAsBi growth by Oe *et al.* [17], it was demonstrated that low growth temperatures and III/V group ratios close to unity were necessary for Bi incorporation. Growth models were proposed by Tiedje's group [68] to explain the processes during MBE growth. The GaAsBi model suggests that the source for Bi incorporation comes from the Bi surface wetting layer. This coverage can be modeled with a Langmuir adsorption isotherm, and the curve can be derived from the reflection high energy-electron diffraction (RHEED) characteristics [68].

Lu *et al.* alternatively suggested the GaAsBi growth model that explains the dependence of the incorporated Bi content on the growth conditions [69]. Lu *et al.* identified three different processes, sketched in Figure 2.6. The first process includes the formation of a Bi-Ga-As bond, where a Ga atom is placed between the Bi surface wetting layer and the GaAs film layer. Bi atoms are incorporated due to the strong Bi segregation effect on the surface and low Bi vapour pressure. The second

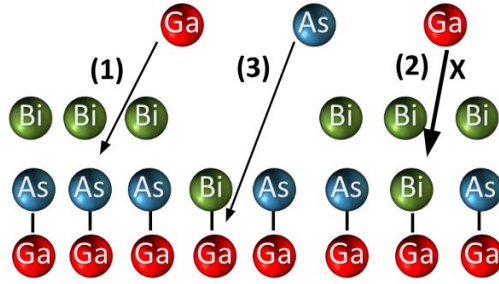


Figure 2.6 Lus' model schematic illustration [69].

process involves the Ga atom insertion between two Bi atoms, where one of them is bonded to the Ga site and the other sticks to the surface. Lu assumed that Bi-Ga-Bi formation is forbidden due to significant strain. The third process involves Bi evaporation, where incorporated Bi is ejected back to the surface and replaced by an As atom. The Ga-Bi bond is thermally activated within this process. Combining these processes, the following rate equation has been derived:

$$\frac{dx}{dt} = \theta_{Bi}F_{Ga}(1-x) - \alpha F_{As}e^{(-U_1/KT)}x. \quad (2.3)$$

Here α is the fitting parameter, F_{Ga} is the Ga flux, x is the Bi content, F_{As} is the As flux, U_1 is the thermal activation energy, θ_{Bi} is the Bi surface coverage according to Langmuir model [70]. Under the steady state $\frac{dx}{dt} = 0$, this equation reads as:

$$x = \frac{b(F_{Bi} - xF_{Ga})e^{(U_0/KT)}}{1 + b(F_{Bi} - xF_{Ga})e^{(U_0/KT)}}. \quad (2.4)$$

Here F_{Bi} is the Bi flux, b is the fitting constant and U_0 is the desorption energy. In Eq. 2.4 x represents the incorporated Bi concentration dependence on temperature and it fits rather well the experimental characteristics.

The characteristics, simulated using Lu's model are represented by dashed lines in Figure 2.7, while experimental data are shown by symbols. The correlations between Bi concentration and As flux are shown by the solid line in Figure 2.7. It can be concluded (from Figure 2.7) that the concentration of incorporated Bi increases reciprocally to As flux, for fixed growth temperature. Keeping other parameters fixed, it

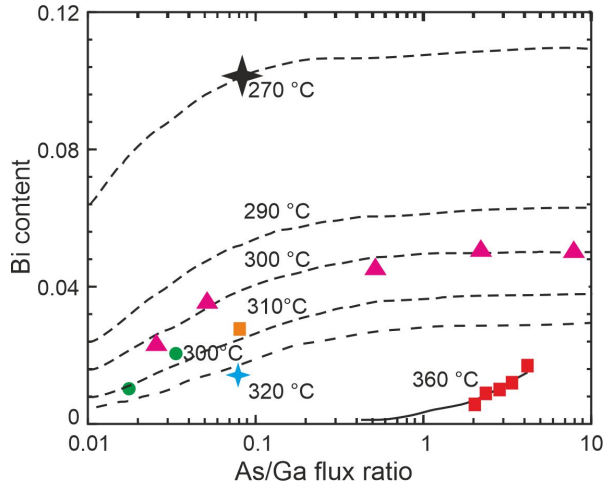


Figure 2.7 Lu's theoretical model comparison with experimental results [69].

has been obtained that Bi concentration increases with Bi flux and saturates at high Bi fluxes. Additionally, the Bi content can be enhanced by lowering the growth temperature. The Bi incorporation, according to Lu's model, is also dependent on As replacing the Bi component. Lu's model explains the effects of cross-related variations of Bi flux, As flux, and growth temperature. Experimentally, the As/Ga flux ratio was determined to be the most sensitive parameter for governing the GaAsBi growth [69]. Nevertheless, it appeared that Lu's model is no longer valid for large amount of Bi incorporation.

Lewis *et al.* alternatively proposed a model which considers that the Bi incorporation depends on As/Ga surface coverage ratio [34]. Therefore, the As/Ga ratio should be carefully controlled during GaAsBi growth. The Bi incorporation rate according to Lewis' model is described by the following equation:

$$\frac{dx}{dt} \propto \theta_{Ga}\theta_{Bi} - \alpha_1 x F_{Ga} - \alpha_1 x e^{\frac{-U_1}{k_B T}}. \quad (2.5)$$

Here, x is the incorporated Bi content, θ_{Ga} and θ_{Bi} are the Ga-terminated and Bi-terminated surface coverage, respectively, α_1 and α_2 are the model constants, U_1 is the activation energy for the Bi atom breaking within the Bi-Ga bond, and k_B is the Boltzmann constant.

Three components of the equation 2.5 correspond to three processes, those are sketched in Figure 2.8. The first step is the Bi incorporation

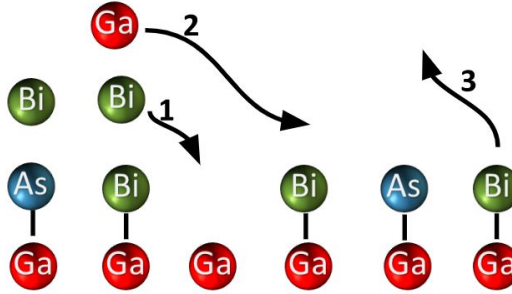


Figure 2.8 Lewis' model schematic illustration [34].

process, the rate of which is proportional to $\theta_{Ga}\theta_{Bi}$. The second process is the Bi atom attachment to the free Ga atom, which results in a reduction of the surface Bi content. Lewis *et al.* rejected this process, explaining that it has a minor impact compared to other processes [34]. The third process includes the evaporation of the incorporated Bi atoms back to the surfactant layers. The activation energy U_1 is the energy difference ascribed to an incorporated Bi atom and to a surfactant Bi atom. In Lewis's model, the θ_{Ga} parameter is the essential term. The Lewis model assumes that Bi atom site behaves like an As site when an As atom settles on a Bi site. This assumption excludes As occupation of the Bi site. Likewise, Bi is assumed to act like a Ga site when a Ga atom settles on it. Applying these assumptions and choosing appropriate values of P_A , P_G , U_1 , α_1 , and α_2 , Lewis's model fits rather well the experimental characteristics. The Bi% content variations versus As/Ga BEPR and Bi/Ga BEPR are illustrated in Figures 2.9 (a) and (b), respectively.

Lewis' model focuses on As/Ga flux ratio stoichiometry conditions for Bi incorporation. This model is not valid for large As/Ga flux ratios, as the Ga coverage quickly approaches to zero. In this case, Lu's model is more appropriate.

2.3.4 Influence of growth parameters

A window for optimal growth conditions is very narrow in order to achieve the high-quality growth without droplets on the surface and with high Bi content. This requires starting the growth process at low temperatures with precise control of As, Ga, and Bi fluxes. The depen-

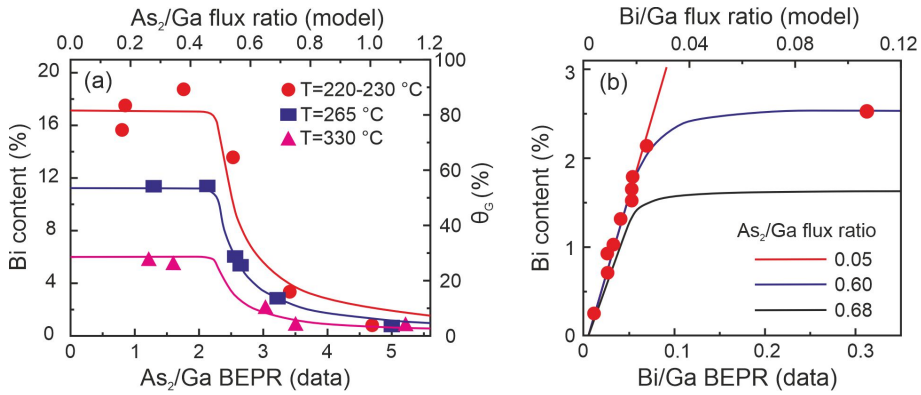


Figure 2.9 (a) Bi% content plotted versus As/Ga BEPR with solid curves representing the fitting of Lewis's model, and (b) the Bi% content plotted versus Bi/Ga BEPR. Reproduced from Ref. [34].

dence of Bi incorporation on growth parameters, such as As/Ga ratio, Bi flux, growth temperature, and growth rate, is elaborated below.

The role of the As/Ga flux ratio parameter

As and Bi are both group V atoms that have a tendency to bond with III group atoms such as Ga. Since the Ga-As bond is stronger than the Ga-Bi bond, an excess of As atoms compete with Bi for bonding to Ga. Therefore, the possibility of Ga-Bi bonding is increased, resulting in higher Bi content in the structure, when As/Ga flux ratio decreases. However, a reduction of the As/Ga flux ratio increases the risk of forming Ga droplets, as the excess Ga atoms cannot be evaporated. Because of this, it is necessary to control the As/Ga flux ratio carefully in order to achieve high Bi concentration and to avoid Ga droplet formation. The relation between Bi% concentration and As/Ga flux ratio is illustrated in Figure 2.9 (a) There, the employed structures were grown at different substrate temperatures, as 220 – 230 °C, 265 °C, and 330 °C and using the 0.47, 0.35, and 0.09 Bi/Ga BEPR, respectively [34]. Bi content was evaluated using high-resolution X-ray diffraction (HR-XRD) data, and it was inferred that Bi concentration increases with a reduction of As/Ga flux ratio.

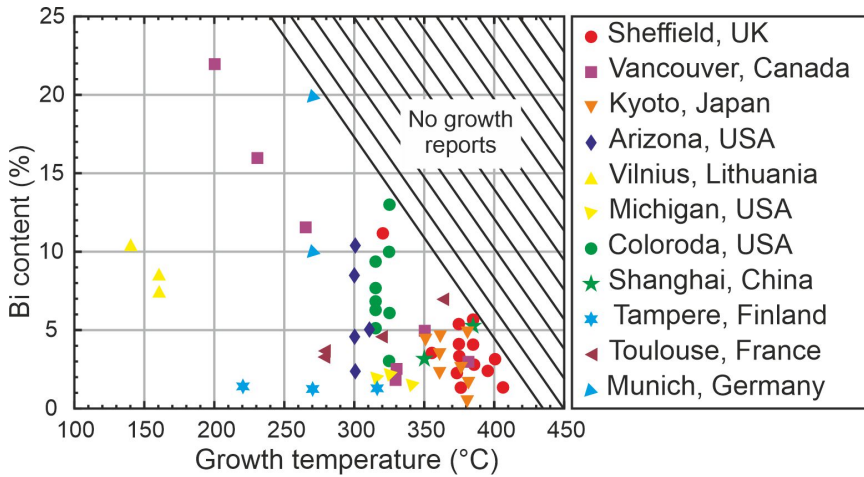


Figure 2.10 Bi contents obtained at different MBE growth temperatures reported by different research groups: Sheffield, UK [71–73]; Vancouver, Canada [26,34,74]; Kyoto, Japan [30,75]; Arizona, US [56,76]; Vilnius, Lithuania [13]; Michigan, US [77]; Colorado, US [59,65]; Shanghai, China [78]; Tampere, Finland [79]; Toulouse, France [80]; Munich, Germany [81].

The impact of the Bi flux

Both Lu's and Lewis's models predict that the Bi content increases with Bi flux when all other parameters, such as As and Ga flux and growth temperature, are fixed. According to Lewis' model, the maximum Bi content can be achieved when the As/Ga flux ratio is close to unity. On the other hand, Lu's model anticipates the saturation of the incorporated Bi amount, and Bi content reaches its maximum when the surface is covered by Ga atoms. Ptak *et al.* showed that Bi content linearly increases with Bi flux while these Bi values also depend on growth rates, as illustrated in Figure 2.11.

Dependence on growth temperature

The alloy growth temperature is a crucial parameter in MBE technology since it influences several physical processes on the surface. The prevailing processes would be as follows: the desorption of As and Bi atoms, surface diffusion of atoms, Bi segregation, reconstruction, and dislocation of Ga-Bi bonds. The percentage incorporation of Bi atoms increases reciprocally to the growth temperature. It was found that 22% Bi can be introduced at a growth temperature of 200 °C [34]. How-

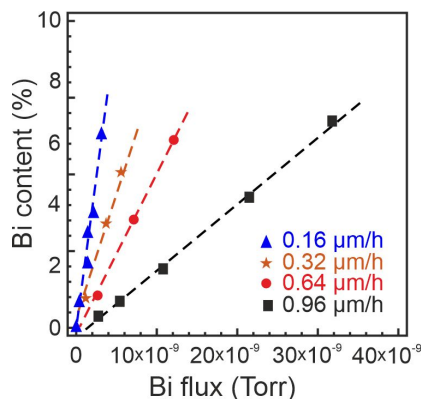


Figure 2.11 Bi content as a function of Bi flux grown at different growth rates [65].

ever, the increase of the growth temperatures above 350 °C leads to the reduction of the Bi content due to the strong desorption of Bi at high temperatures. The Bi% amounts reached using different MBE growth temperatures and reported by various research groups are summarized in Figure 2.10.

The impact of the growth rate

The growth rate is important in order to avoid the formation of Bi droplets. There is enough time at a low growth rate for the excess Bi atoms to be evaporated. This prevents the formation of Bi droplets. Lu *et al.* demonstrated that 10% Bi amount was reached at low density of Bi droplets ($1.7 \times 10^6 \text{ cm}^{-2}$) by keeping the growth rate at $0.07 \mu\text{m/h}$ and growth temperature of 270 °C. Lewis *et al.* also showed that samples grown at $1 \mu\text{m/h}$ rate contain the higher Bi content relative to those grown at $0.13 \mu\text{m/h}$. Considering the kinetically-limited growth regime in the approaches of Lu's and Lewis's models, Ptak *et al.* proposed a new viewpoint on growth rate.

Figure 2.11 illustrates the relations between the Bi content and Bi flux at different growth rates, such as 0.16, 0.32, 0.64, 0.96 $\mu\text{m/h}$ from Ref. [65]. This graph demonstrates that the Bi concentration doubles when the Bi flux is doubled, while doubling the growth rate reduces the Bi concentration to half. It is important to note that Ptak's model obeys for a low Bi flux of 3×10^{-8} Torr.

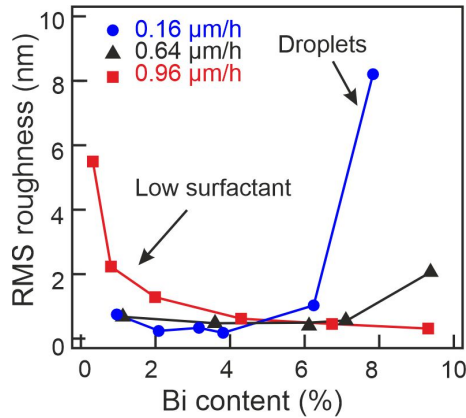


Figure 2.12 The RMS dependence on Bi content obtained at different growth rates. Reproduced from Ref [65].

The Bi fluxes considered here are significantly lower than those involved within Lu's and Lewis's models. Nevertheless, a smooth and droplet-free Bi surface alloys can be grown over a large range of Bi concentrations, by properly adjusting the Bi flux and growth rate parameters.

The specifics of compositions and surface quality can be revealed using atomic force microscopy (AFM) examination of the deposited alloys. The root-mean square (RMS) roughness values as a function of Bi content are shown in Figure 2.12. These characteristics have been extracted using $5 \times 5 \mu\text{m}^2$ AFM scans, performed on alloys grown using different growth rates. It has been shown that a low growth rate ($0.16 \mu\text{m/h}$) and a rather small amount of Bi ($x < 6\%$ Bi), lead to the formation of smooth surfaces [65]. However, the formation of Bi droplets is inevitable for alloys of $x > 6\%$ Bi content. Contrarily, the samples grown using an enhanced growth rate of $0.96 \mu\text{m/h}$ exhibit the formation of Bi droplets at low Bi content ($x < 2\%$ Bi), and the surface gets smoother for alloys containing the higher Bi content ($x > 2\%$ Bi). This hints that the high growth rate weakens Bi atom diffusion on the layer surface, and droplets are consequently formed. For the intermediate growth rate $0.64 \mu\text{m/h}$ the surface appears to be smooth up to 7% Bi amounts. The difference in Lu's and Ptak's results appears to be dependent on Bi surface coverage. In Lu's model, Bi flux is large, and, therefore, Bi droplet formation appears. Lowering the growth rate re-

sults in Bi atom evaporating, and a smoother surface is formed due to the higher Bi content. In Ptak's model, the small Bi flux is assumed. Thereby, Bi atoms can reach higher amounts at the retention of smooth layer surface when even higher growth rates are employed.

2.4 Compound semiconductors for optoelectronic applications

GaAsBi is a promising material in optoelectronic applications for around two decades. The band-gap engineering by only a few percent of bismuth amount variations makes GaAsBi attractive for the fabrication of THz emitters, telecommunication spectral range lasers, photodetectors, and other devices. GaAsBi is also attractive material for spintronic applications due to the presence of localised states induced by bismuth introduction. A material with a nearly temperature insensitive band-gap is very suitable in the production of NIR and MIR spectral range for LEDs. This subsection is devoted to an overview of the GaAsBi material application for lasers and light emitting diodes.

2.4.1 Lasers and LEDs

Light emission wavelengths in the range from 1.3 μm and 1.55 μm are crucial for the telecommunication spectral range. The InGaAsP quantum well lasers based on the InP material platform are commonly used for emission of this radiation. However, drawbacks such as threshold current and internal radiation loss are inherent in these devices. The appearance of these deficiencies strongly depends on the ambient temperature (above room temperature (RT)) due to the impact of the Auger recombination [82]. Therefore, extra cooling is necessary for the proper functioning of these commercially available lasers. However, this increases the overall energy consumption. The GaAs-based semiconductors are also very attractive due to their direct band-gap and relatively low price. The technologically needed GaAs substrates are much cheaper than the InP substrates.

Sweeney *et al.* in 2013 performed calculations concerning GaAsBiN/GaAs structures, by considering the parameters such as

band-gap, splitting energy, strain, and band offsets [83]. They reported that the GaAsBiN alloy with 12% Bi amount and 6% N content covers a wide range of 0.2 – 1.4 eV, and the lattice of such a quaternary compound is well matched to GaAs substrate. As discussed in Chapter 2.2.2, the VBA model suggests that in Bi-containing alloys the condition $\Delta_{SO} > E_g$ can be achieved. This leads to suppression of the non-radiative Auger recombination. Such a quaternary GaAsBiN alloy grown on a GaAs substrate enables the engineering of material band structure, with subsequent emission energy tune-up in the range of 450 – 850 meV (1.5 – 2.7 μm). This has the potential to cover the MIR spectral range with flexible control of the energies of material band-gap and of spin-orbit split.

In 2012, Lewis *et al.* first reported manufacturing of the GaAsBi LEDs with 1.8% Bi amount, those emitted IR light peaked at 987 nm [34]. The active region of these LEDs consisted of a 50 nm thick GaAsBi layer, and the LED exhibited stable emission over 100 – 300 K temperature range. In 2016, Richards *et al.* reported a GaAsBi LED fabricated using 6% Bi content. These LEDs emitted 1200 nm radiation [84]. Patil *et al.* [6] used the so-called two-substrate temperature (TST) method to make the LED structures. There, the quantum well layer was grown using a rather low temperature ($T_{\text{GaAsBi}} = 350\text{ }^\circ\text{C}$), while the barriers were formed at the elevated temperature ($T_{\text{GaAs}} = 550\text{ }^\circ\text{C}$). Thereby, manufacturing of GaAsBi QW LED with 4% Bi was reported. Such a LED emitted 1230 nm radiation at room temperature [6]. The TST method fabricated LED operated at a turn-on voltage of 3.3 V and injection current of 120 mA under current density values of 1.0 kAcm^{-2} .

In 2010, Yoshimoto *et al.* produced an optically-pumped GaAsBi/GaAs Fabry-Perot cavity laser. This GaAsBi/GaAs laser was formed by MBE growth using the 2.5% Bi amount. Such laser operated at room temperature and emitted radiation peaked at 982.8 nm wavelength [4]. In 2013, the same group improved the growth technology to deposit the GaAsBi active layer with 5.8% Bi content. The latter laser emitted radiation peaked at 1204 nm under room temperature ambient [85]. In the same year, Ludewig *et al.* demonstrated the first electrically-pumped GaAsBi laser formed by

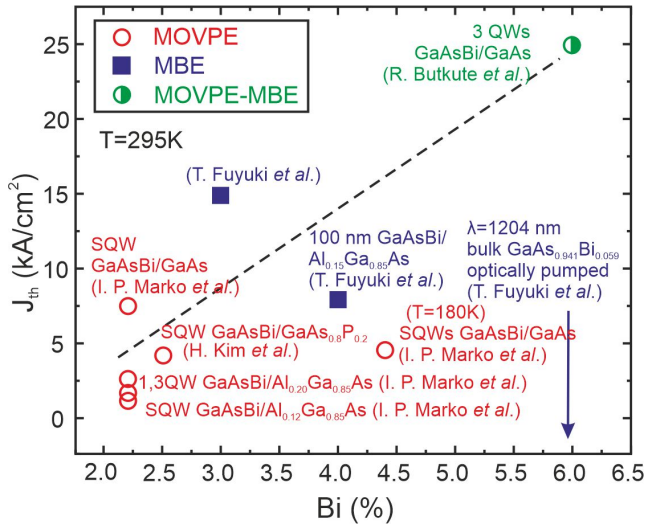


Figure 2.13 Threshold current density for GaAsBi based lasers as a function of Bi amount, summarized using Refs. [13, 85–87, 93, 94].

MOVPE technology and using 2.2% Bi incorporation [5]. This laser consisted of a 6.4 nm thick GaAsBi single quantum well structure sandwiched between two AlGaAs layers of 150 nm thickness. The latter layers were covered by 1.4 μm AlGaAs n- and p-doped materials. The 947 nm wavelength has been emitted by this electrically-pumped IR laser able to function at room temperature. The operation threshold current density there was 1.56 kA/cm^2 . Sweeney's group also reported the electrically-pumped GaAsBi/GaAs lasers grown by MOVPE. Fuyuki *et al.* reported similar devices with 3% and 4% Bi grown by MBE, with emission up to 1045 nm [86,87]. Butkutė *et al.* demonstrated GaAsBi QW laser with 6% Bi, grown using a combination of MBE and MOVPE growth techniques. In 2019, Glemžka *et al.* investigated the low-frequency noise characteristics of the GaAsBi/GaAs lasers containing 8% Bi amount. Such structures are grown by MBE enabled lasing at 1142 nm wavelengths. The top parameters of GaAsBi lasers are summarized in Table 2.1. Although the GaAsBi based lasers and LEDs of proper performance have been reported in literature, some problems, such as an extending of the emission wavelength range and improving of material optical as well as electrical properties, are still under research.

Table 2.1 Characteristics of the GaAsBi based lasers reported in literature.

Reference	Year	Growth technique	Structure	Bi content, (%)	λ , nm (at RT)	Current threshold density / emission energy density
Tominaga [4]	2010	MBE	Bulk	2.5	982.8; 986.2	2.5 (mJ cm ⁻²)
Fuyuki [85]	2013	MBE	Bulk	4.2	947	1.56 (mJ cm ⁻²)
Ludewig [5]	2013	MOVPE	SQW	2.2	1088.6; 1204	0.36 (kAcm ⁻²)
Fuyuki [87]	2014	MBE	Bulk	3; 4	976; 1045	15; 8 (kAcm ⁻²)
Marko [86]	2014	MOVPE	QW	4.4	1038	4.5 (kAcm ⁻²) at 180 K
Butkutė [13]	2014	MBE; MOVPE	QW	6.5	1060	30 (kAcm ⁻²)
Broderick [88]	2015	Theoretical	QW	13	1550	-
Wu [89]	2017	MBE	QW	5.8	1135; 1142	3.89 (kAcm ⁻²)
Liu [90]	2017	MBE	SQW	-	1141	4.54 (kAcm ⁻²)
Glemža [91]	2019	MBE	QW	8	1090	-
Liu [92]	2019	MBE	QW	5.8	1276; 1407	-

Various types of the active layer structures have been employed to fabricate the GaAsBi-based laser diodes, as summarized in Figure 2.13. There, the characteristics of the threshold current density of GaAsBi lasers as a function of the incorporated Bi amount, borrowed from Refs [85–87,93,94], are represented. It can be deduced from Figure 2.13, that the device performance worsens with enhancement of the incorporated Bi fraction. The large threshold current density, necessary for operation of bismide laser diodes, based on materials containing the elevated Bi amounts, needs further improvement and optimization of the growth technologies, to fabricate the GaAsBi based devices, suitable for practical applications.

3. MBE GROWTH AND CHARACTERIZATION TECHNIQUES

Various techniques for epitaxial growth exist, including liquid phase epitaxy, molecular beam epitaxy, and metal-organic vapour phase epitaxy. The MBE is commonly used in the production of single semiconductor devices and quantum structures, while MOVPE is widely used within the commercial industry. Both MOVPE and MBE are employed in the growth of the bismide layers. In this chapter, the MBE growth method used for the GaAsBi alloy formation is discussed including growth conditions and substrate preparation. Also, the *in situ* and *ex situ* characterisation techniques employed for measurements of the optical and electrical properties on the epitaxial structures are briefly reviewed.

3.1 MBE technique

MBE is an epitaxial growth process at the atomic or molecular scale, carried out under ultrahigh vacuum (UHV) conditions on a crystalline surface. This technique was first approved by A.Y. Cho at Bell Laboratories, and the first demonstration of GaAs growth using MBE was reported in 1971 [95,96].

The fundamental principle of MBE is that ultra-pure source materials are heated, and through thermal evaporation, beams of molecules are generated. These beams are directed towards a heated substrate where the molecules can be adsorbed, settled down, or desorbed from the surface. These molecules can also migrate across the surface. The substrate temperature should be carefully controlled during the growth

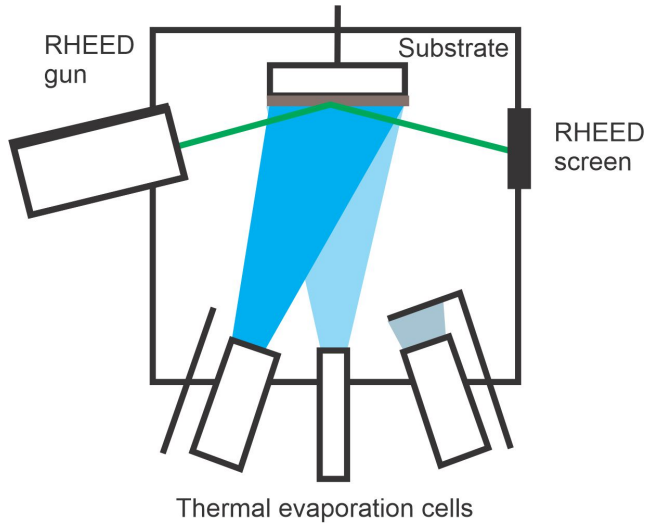


Figure 3.1 Schematic diagram of molecular beam epitaxy main chamber [97].

procedure to enhance the mobility of the atoms and minimize thermal desorption. The optimal growth temperature is determined based on the source materials employed during the growth process. The growth process is monitored *in situ* using a technique of reflection and high-energy electron diffraction. Additionally, a pump is used to remove waste heat from the vacuum chamber and reduce the pressure in the system. A schematic diagram of the MBE main chamber is shown in Figure 3.1. The operation principles of the MBE system will be elaborated in this chapter.

3.1.1 The employed MBE system

One of the most important features of MBE instrumentation is the requirement of UHV, with a partial pressure of 10^{-12} Torr without heating and $10^{-7} - 10^{-8}$ Torr during growth. The latter procedure is implemented under cooling with liquid nitrogen. The achievement of UHV is a critical factor for ensuring high-quality growth.

The growth of structures is performed in an MBE chamber where the substrate is placed on a heated and rotating holder to ensure the homogeneity of the deposited layer. The system is equipped with various types of pumps, including a rotary pump, a turbomolecular pump, an ion-titanium pump as well as closed-cycle helium cryopump, which

maintains a very high general vacuum level within the system.

MBE systems are equipped with Knudsen cells those are filled with pure materials of 7N5 (of 99.999995% purity). These cells have a specific shape that ensures a sufficiently small dispersion of vaporized materials. The materials in the cells are heated to the temperatures at which they reach evaporation or sublimation. The fluxes of different sources are combined. These fluxes are monitored at specific times by the shutters, and the size of the flux is changed by altering the temperature of the Knudsen cell. Different beam fluxes can be turned on and off to implement the high precision deposition of mono-layers using mechanical shutters positioned in front of each source. The epitaxial layer is formed through the precipitation of atoms on the substrate. Atoms of the deposited precursors settle on the substrate forming mutual bonds, as sketched in Figure 2.5. The arsenic source consists of two parts: the sublimator and the cracker. The temperature in the range of 350 – 460 °C is typically set. The cracker thermally fractures the molecules As_4 or As_2 at a temperature of 800 – 1000 °C. The As_2 is preferential relative to As_4 , as As_2 needs lower growth temperatures compared to As_4 [98], while the better light-emitting materials are also formed using As_2 .

RHEED technique is used to monitor the layer structure *in situ* throughout the growth process. The 10 kV electron beam is split and directed onto the sample surface at a slight angle ($<3^\circ$). The image of the reflected beam is modulated on a phosphor screen and recorded by a computer. The recorded oscillation of the RHEED signal intensity enables the tracking of surface morphology. This characteristic provides a valuable information on growth kinetics, on monolayer coverage, and layer growth rate.

In this work, the GaAsBi/AlGaAs quantum well structures and laser diodes were grown using a solid-source MBE system *Veeco GENxplor R&D*. Bulk 100 nm thick GaAsBi/GaAs layers were grown using SVT-C-V-2 (USA) and *Veeco GENxplor R&D* instruments.

3.1.1.1 SVT-C-V-2 instrumentation

The bulk 100 nm GaAsBi/GaAs layers were grown using the SVT III-V MBE System Model C-V-2 (USA) instrumentation. The

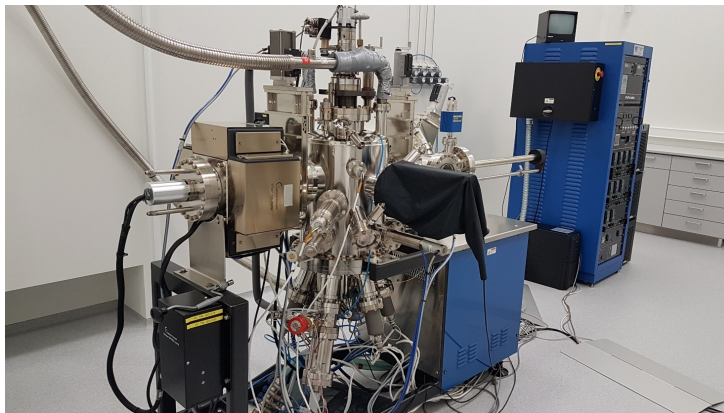


Figure 3.2 Photo of the SVT-C-V-2 Molecular Beam Epitaxy system.

MBE device comprises load lock and growth chambers cooled by liquid nitrogen and water equipped with independent UHV pumping channels, isolated from each other by gate valves. The growth module contains an integrated ion and titanium sublimation pump system, which provides a base vacuum level of 5×10^{-9} Torr. The load lock is equipped with a turbo molecular pump (to maintain the base vacuum level 5×10^{-8} Torr). The rotary pre-pumps are routinely employed in vacuumation procedures. The MBE system is equipped with In, Ga, Al, Bi, and As precursor sources, and an As_2 valved cracker. Si and Be dopants are available for n-type and p-type doping, respectively. The layer structure and growth thickness are monitored *in situ* using RHEED in instrumentation. The temperature of the substrate is measured using a thermocouple. Throughout the growth process, the substrate is rotated to achieve uniformity of temperature and layer thickness across the entire substrate. The system is also equipped with Fast Action Shutters (with <150 msec duration for Open/Close operations) and uses the RoboMBE process automation system.

3.1.1.2 Veeco GENxplor R&D instrument

The GaAsBi/AlGaAs quantum well structures and 100 nm bulk layers were grown using a solid-source Veeco GENxplor R&D MBE system (USA), which is equipped with standard cells for metallic precursors of In, Al, $2 \times$ Ga, and Bi, As, Sb within bulk evaporator, and

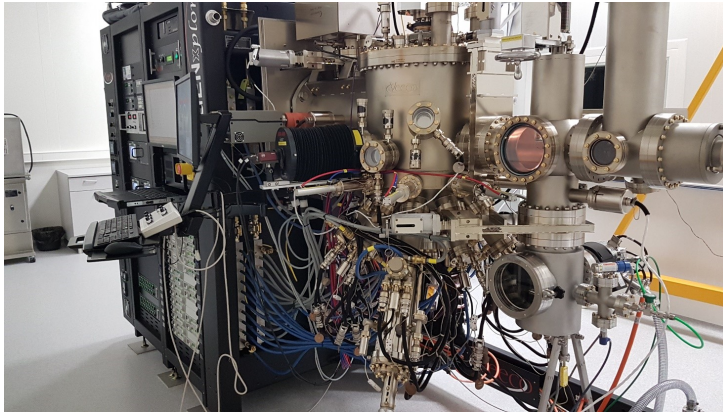


Figure 3.3 Photo of the *Veeco GENxplor R&D* Molecular Beam Epitaxy.

a cracking head for generating fluxes of pure As_2 and Sb. Growth of n-type materials is implemented using Si and Te sources, while for deposition of p-type materials, Be dopant is used. The growth chamber is equipped with integrated ion and Titanium sublimation pumps (with base vacuum level 5×10^{-12} Torr) as well as a closed-cycle helium cryogenic pump. On the other hand, the preparation chamber has an ion pump, and the loading chamber has a turbomolecular pump (base vacuum level 5×10^{-8} Torr). This powerful and efficient ultra-high vacuum pumping system helps maintain an extremely clean vacuum environment in the growth and preparation chambers, enabling the growth of high-quality materials suitable for optoelectronics. The system is capable of growing on substrates up to 3 inches in diameter. This system is also equipped with Fast Action Shutters (<150 msec Open/Close), allowing for the precise control of growth procedures.

3.1.2 Substrate preparation

Prior to GaAsBi growth, proper substrate preparation is necessary. The 2-inch diameter wafers are routinely cleaved into quarters to fit the mounting holders. The cleaving process is performed by scribing an edge on the wafer while it is held in a special holder.

The cleaved quarter of the substrate is mounted to the holder and loaded into the load lock. It is heated to 200°C for 4 hours to remove the ambient made humidity. Once completed, the holder is loaded into

the growth chamber, and the wafer is outgassed at approximately 680 – 700 °C temperature to remove native oxides (Ga_2O_3 and As_2O_3). The vacuum pressure is monitored using an ion gauge with a fully opened arsenic valve. The RHEED response is studied during the outgassing to verify oxide removal. The oxide removal process roughens the substrate surface. Then the GaAs buffer is deposited to recover a smooth surface, to be suitable for the GaAsBi growth.

3.1.3 Procedures of the GaAsBi growth

After depositing the GaAs buffer layer, the substrate temperature is reduced from approximately 665 °C to 320 – 425 °C, in order to start the growth of GaAsBi. The As/Ga BEPR is adjusted by changing the arsenic valve. The As, Ga, and Bi fluxes are monitored using an ion gauge. Prior to GaAsBi growth, the sample surface is pre-deposited with Bi for 10 seconds and then allowed to settle for 10 seconds in order to reduce Bi segregation during GaAsBi growth. The growth of quantum well structures is performed by Bi pre-deposition implemented only before the first QW deposition. The entire growth process is monitored using RHEED. Finally, after GaAsBi growth, a thin GaAs cap layer is grown using the same growth temperature (320 – 425 °C) in order to avoid annealing of the grown structure.

3.2 Techniques for the *in situ* monitoring

This section describes the *in situ* techniques employed in characterisation of the epitaxial growth processes.

3.2.1 Surface and growth rate control by RHEED technique

Reflection high-energy electron diffraction technique is an *in situ* MBE control tool that provides information about the surface structure, layer quality, and growth rate. The instrumentation consists of two parts: a phosphor screen and an electron gun. The electron beam strikes the sample at an angle of 1 – 3 °, forming visible diffraction patterns on the screen. RHEED is performed in UHV to minimize electron scattering. RHEED is a highly surface-sensitive method as

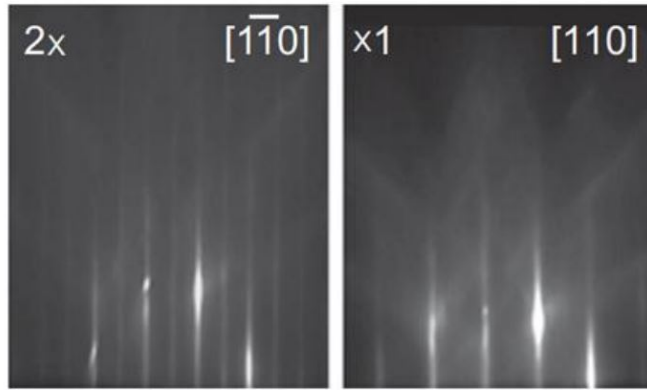


Figure 3.4 Images of GaAsBi surface reconstructions observed during growth: (a) $\times 2$ $[1\bar{1}0]$ and (b) $\times 1$ $[110]$ direction.

the electron beam penetrates only one or two monolayers into the substrate. The pattern is a periodicity of atoms that are related to surface reconstructions of the sample. The RHEED pattern is described as the $n \times m$ imaging, where n and m are surface reconstructions from $[110]$ and $[1\bar{1}0]$ planes, respectively. The preferred reconstruction for GaAsBi epitaxial growth is (2×1) (see Figure 3.4).

In the picture, $2 \times$ indicates that the periodicity of the surface reconstruction in $[1\bar{1}0]$ direction is twice that of the bulk and $\times 1$ indicates that the reconstruction is the same as the bulk in the $[110]$ direction. High quality GaAs exhibit (2×4) surface reconstructions. The surface reconstruction phase maps for GaAs and GaAsBi are illustrated in Figure 3.5.

It is important to understand how images of reconstructions are related to Bi incorporation. Typically, the standard (2×1) reconstructions are observed, in Figure 3.5. However, a recent study reported by Cornil *et al.* [80] the (1×3) and (2×1) RHEED reconstructions were related to Bi incorporation and it was found that Bi incorporation imaged by (1×3) reconstruction was more efficient. It has also been shown that at low As/Ga ratio (close to unity) the (1×3) reconstruction is shortly modified into (2×1) reconstruction.

The RHEED oscillations also enable measurements of the layer growth rate. The intensity of RHEED responses depends on surface

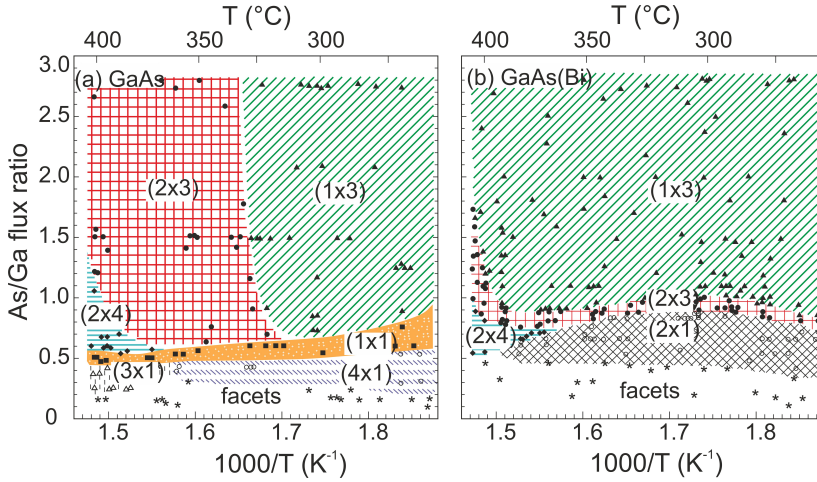


Figure 3.5 Surface reconstruction maps of (a) GaAs and (b) GaAsBi. According to Ref. [99].

roughness, which changes due to the deposition of an atom monolayer on the surface. At the start of growth, the surface is smooth, the layer is flat, and the RHEED signal appears as a peak of oscillation. The RHEED intensity decreases because the surface is no longer smooth when material islands begin to form on the surface. The lowest intensity point is reached when half of the monolayer is grown. Then, the intensity increases as the surface becomes flat again due to the formation of the complete monolayer. The formation of this characteristic is illustrated in Figure 3.6.

3.2.2 Beam flux measurement

Precise measurements of the MBE precursor source are crucial within growth of GaAsBi layers. Flux is defined as the number of atoms per unit area per time unit, and their ratio is calculated according to equation 3.1:

$$\frac{F_x}{F_y} = \frac{BEP_x \eta}{BEP_y \eta} \sqrt{\frac{T_x M_y}{T_y M_x}}. \quad (3.1)$$

Here beam equivalent pressure (BEP) is the particle pressure measured by an ion gauge, η is the ionization activity of particles, T is the temperature of particles and M is the molecular (atomic) mass. The

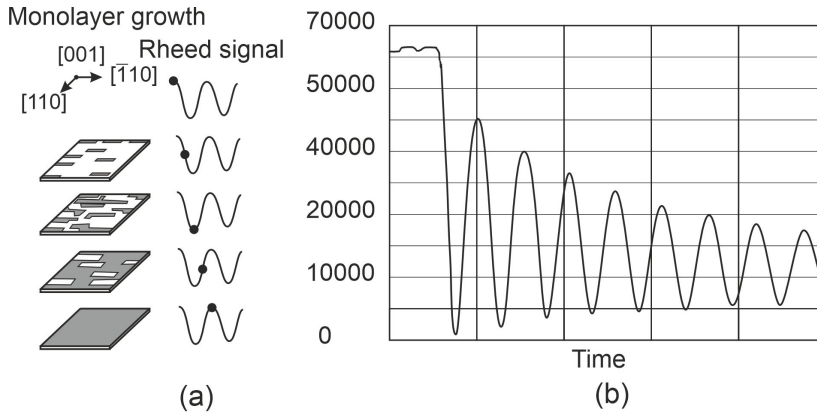


Figure 3.6 RMS dependence for Bi content at different growth rates. Reproduced from Ref. [65].

BEP parameter is only measured during the growth. BEP is measured by a Bayard-Alpert Style Ionization Gauge each time before the growth of the structure, in order to set the As/Ga flux ratio. For the As-rich growth of GaAs, the growth rate is determined by the Ga flux, since Ga evaporation is negligible under normal conditions [100]. All the BEPs monitoring the Ga, Bi, As, and Al precursors were measured. Then $BEPR = P_x/P_y$ was calculated. In the case of a lack of As the GaAsBi structures with a high concentration of defects/metallic Ga droplets formed on the surface are obtained. Therefore, it is crucial to precisely control fluxes of the III group elements because they are also responsible for the layer deposition velocity.

3.3 Techniques of the *ex situ* characterisation

This section describes the *ex situ* techniques those were used to characterise various structural, optical, and electronic properties of the grown quantum structures, films, and devices.

3.3.1 High-resolution X-ray diffraction

High-resolution X-ray diffraction is a powerful non-destructive tool for the *ex situ* monitoring of fabricated structures which provides information on crystal parameters, crystalline quality, layer thickness, alloy composition, mismatch, and interface roughness. The most common

HR-XRD characteristic is the rocking curve registered by ω - 2θ scan reflexes diffracted off the (004) plane. The lattice parameter is routinely determined by applying Bragg's law:

$$n\lambda = 2d \sin \Theta_B, \quad (3.2)$$

where n is an integer denoting a diffraction order, λ is the wavelength of the X-ray, d is the distance between adjacent parallel atomic planes, and Θ_B is Bragg's angle. For fully relaxed or stressed materials, a represents the actual lattice constant of the layer, from which the alloy composition can be evaluated.

The chemical composition of GaAsBi films is typically determined by analyzing the peak position of the XRD (001) reflexes within rocking curve scans and using Vegard's law. However, for a more precise measurement of the Bi content and better understanding of the lattice structure, it is necessary to quantitatively separate and analyze the effects of strain and composition using reciprocal space mapping (RSM). RSM involves the crystal lattice Fourier transforms, where each point corresponds to a set of crystal planes. The compressive strain relaxation is defined from RSM scanned for the (004) reflex and using grazing incident angle geometry for detection of the (115) reflex.

The HR-XRD measurements were performed using a SmartLab Rigaku diffractometer. The shift of the (004) diffraction peak is routinely monitored with respect to its position within GaAs diffraction patterns. The Cu $K\alpha 1$ line serves as the X-ray source and a Ge(200) $\times 2$ monochromator is employed for spectral rectification of X-ray beams. The diffraction signals are recorded using a point X-ray detector SC-70. The obtained diffractograms were analyzed using the GlobalFit data analysis program and assuming the lattice constants of GaAs and GaBi to be $a_{GaAs} = 5.653 \text{ \AA}$ and $a_{GaBi} = 6.324 \text{ \AA}$ [41], respectively.

3.3.2 Atomic force microscopy

Atomic force microscopy is a powerful tool used to monitor the surface topography and mechanical properties scanned within the nanometer scale. This microscopy technique enables the evaluation of the sample quality through the measurement of the surface roughness

parameters. The tapping mode technique was used to investigate the surface profiles of the samples. The latter technique is implemented when a small needle mounted on the AFM cantilever vibrates up and down at a frequency close to the mechanical resonance frequency. The cantilever oscillation amplitude is kept constant by changing the distance between the probe holder and the examined surface, and the sample topography is mapped using the raster scans. The roughness (RMS) of the surface can be estimated by using such a relation:

$$RMS = \sqrt{\frac{\sum (z_i)^2}{i}}. \quad (3.3)$$

Here z_i is the height of the material surface determined at the mapping point, i is the number of scanned points.

Atomic force microscopy measurements in this research were carried out using a Dimension 3100 SPM AFM system with a Nanoscope IVa controller (Veeco Instruments Inc., USA). Silicon probes (model NCHV from Bruker) with tip radius 8 nm were used.

3.3.3 Scanning transmission electron microscopy

Scanning transmission electron microscopy (STEM) is widely used to investigate structural quality with high spatial resolution. This technique is commonly applied to visualize structures grown using MBE. Special preparation of the samples of minute dimensions are necessary to perform STEM measurements. In this study, GaAsBi structures were specially prepared for TEM measurements using the FEI Helios Nanolab 650 microscope with an Omniprobe manipulator, where the structure is processed using the focused ion beam (FIB) method.

The FEI Technai G20 transmission electron microscope was employed for TEM measurements. The electron beam probe in this microscope was generated using a Schottky field emission electron source. Detectors, such as the 16 Mpix Gatan Orius CCD camera or the Fishione 3000 HAADF STEM detector, were used.

3.3.4 Photoluminescence spectroscopy

Photoluminescence spectroscopy is nearly a standard technique for inspection of the dynamics of charged carriers. Recordings of the radiative recombination photon spectra characterise the excess carrier occupied states with activation energies slightly lower than the energy band-gap. The released energy is additionally converted into lattice vibrations and heat, i.e., phonons when carriers recombine via defect states. Hence, PL spectra recorded on samples containing a high density of defects exhibit the quenched PL intensity due to lattice vibrations. The non-radiative Auger recombination is the most common reason leading to the radiative recombination losses, which limit the luminescence efficiency and restrict applications of PL technique in control of the light emitting devices.

The room temperature photoluminescence (RTPL) spectra were recorded using proprietary made lab equipment. The schematic diagram of the photoluminescence spectroscopy setup is shown in Figure 3.7. The excitation source was a DPSS 532 nm wavelength laser operating with 200 Hz repetition rate and output power up to 200 mW (5 kWcm^{-2}). The third harmonic of this laser radiation at 266 nm wavelength is used for excitation of AlGaAs structure. The excitation intensity is varied in the range of 0.02 Wcm^{-2} to 120 Wcm^{-2} by using spectrum neutral density filters.

The PL signals were detected by a lock-in amplifier synchronized with the laser signal modulation frequency at 193 Hz. The luminescence from the sample was focused using lenses of focus lengths L1 (150 mm) and L2 (325 mm), and directed onto the entrance slit ($d = 3 \text{ mm}$) of an Andor SR500i ($f = 0.5 \text{ m}$, $f/6.5$) monochromator. A 0.42 m focal length monochromator (SPM-2) and a thermoelectrically cooled InGaAs detector was also used for the spectral display of the PL signals. Spectra were recorded keeping fixed the experimental parameters, and this measurement method enabled to compare the recorded spectra in order to evaluate the material quality.

The temperature-dependent photoluminescence characteristics were also examined in the temperature range from 3 K to 300 K. The stabilized temperatures were measured using a LakeShore 335

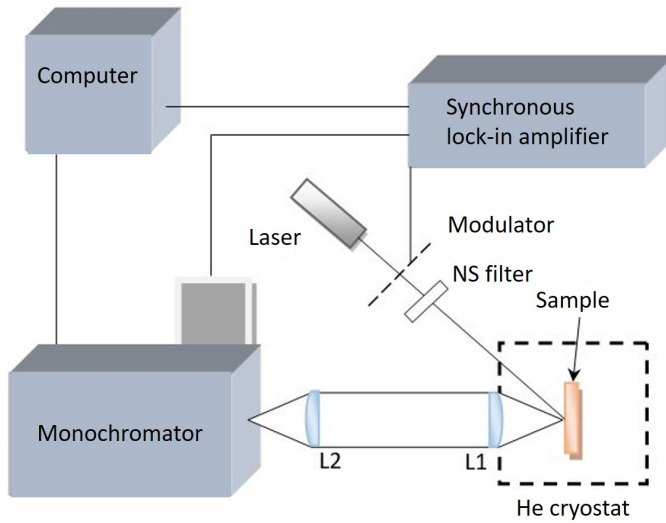


Figure 3.7 Schematic diagram of photoluminescence setup.

temperature controller on samples mounted within a closed-cycle liquid He cryostat.

3.3.5 Electroluminescence spectroscopy

Electroluminescence (EL) is the result of the electrically stimulated radiative recombination of electrons and holes. It is fast and the most convenient method to control of the light-emitting diodes. The structures with p-n junction are necessary to perform material characterisation by electroluminescence spectroscopy. The electrical contacts are routinely made by carefully soldering an In paste on top of the electrode and on the substrate side of the structure under examination. To record the electroluminescence signals, the junction is turned on by applying voltage.

The electroluminescence in this research was examined using the proprietary made lab-equipment. The sample under test was mounted on a Peltier element to keep a fixed temperature. Spectra were examined by varying injection current from 50 mA to 120 mA. Both, the continuous wave (CW) (using a steady-state voltage source) and pulsed (applying short electrical pulses) measurements were performed. The dispersed luminescence signals using either Andor

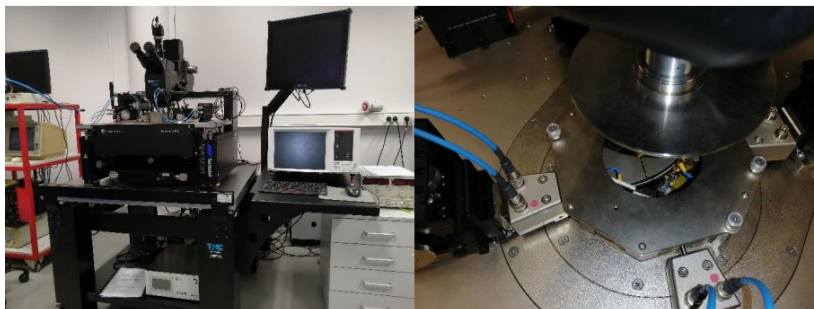


Figure 3.8 Picture of Keithley SCS-4200 probe-station for the I-V measurements.

SR500i or SPM-2 monochromators were recorded using a synchronous DSP lock-in amplifier SR830.

3.3.6 Measurements of voltamperic characteristics

The direct current (DC) electrical measurements on junction structures were carried out at room temperature in a dark chamber. These measurements were implemented using a Keithley 4200-SCS Parameter Analyzer (Keithley Instruments, Inc.) (see Figure 3.8) and a Summit Probe Station 11000B-AP (Cascade Microtech, Inc.) instrument. To minimize noise levels, being less than 10 fA at 10 V, the DC I-V measurement system was connected using triaxial cables and adapters between the probe tips and the Keithley 4200-SCS. Coaxial probes with tungsten core etched to a radius of 5 μm were employed to connect to the top electrode on the sample. The DC voltage was swept in the range of -4 V to 8 V (or lower if the current limit value of 0.1 – 1 A was reached) during the I-V records. The state of the surface of the sample under test was additionally controlled on the LCD screen of the optical microscope.

4. RESULTS ON GROWTH OF 100 NM GaAsBi/GaAs HETEROSTRUCTURES

The sets of 100 nm-thick GaAsBi layers with Bi content ranging from 0.6 % to 11.2 % were grown by molecular beam epitaxy on semi-insulating (SI) GaAs(100) substrates. These layers were buffered with an ultra-thin, up to 20 nm thick GaAs layer. A comprehensive study was conducted to elucidate the relaxation effect on the structural, morphological, and optical properties of the bismide layers. Optical measurements showed a significant reduction of the energy band-gap from 1.40 eV to 0.92 eV for the epitaxial GaAsBi layers. The optimization of GaAsBi growth parameters and analysis of the resulting layers are revealed in this chapter.

4.1 Growth of heterostructures

GaAsBi samples were grown using two solid source molecular beam epitaxy systems: *Veeco GENxplor R&D* (samples marked as VGA series) and *SVT-C-V-2* (samples marked as B series). SI GaAs(100) 2-inch substrates were cleaved into quarters. Initially, the native oxide from the SI-GaAs substrate was outgassed at 700 °C under the maximum arsenic flux for 20 minutes. The sample temperature was then lowered to 680 – 670 °C for VGA samples and to 600 °C for B samples in order to grow a buffer layer. A thin, up to 20 nm GaAs buffer layer was grown, keeping the growth rate of 300 – 500 nm/h, to provide an atomically flat surface for epitaxial growth. The thickness of the buffer layer was determined from the changes in RHEED image from the bulk substrate pattern of (1×1) towards the determined surface reconstruction

of (2×4) . Source temperatures were set to $T_{Ga} = 886$ °C and $1045 - 1055$ °C, as well as $T_{As} = 380$ °C and $440 - 450$ °C as well as $T_{Bi} = 630 - 640$ °C and $565 - 575$ °C for VGA and B set of samples, respectively. The substrate temperature was lowered to the GaAsBi growth temperature in the range of $320 - 425$ °C (Table 4.1). The reduced As/Ga flux ratio varied from 0.922 to 1.091 by changing the As crack valve position (Table 4.2). Structures were grown at low temperatures to prevent segregation of bismuth towards the surface. To improve Bi incorporation, samples were exposed to a Bi flux for 10 seconds, resulting in partial coverage of the buffer with a Bi wetting layer which acted as a surfactant. The growth temperature was monitored using thermocouple readings. During the growth process, surface quality and growth mode were continuously monitored *in situ*, layer by layer, using RHEED. The GaAsBi layer growth rate was evaluated from RHEED oscillations. This rate was estimated to be 460 nm/h for VGA samples and 730 nm/h and 845 nm/h for B samples. The obtained difference is related to T_{Ga} , lower Ga source temperature, and lower growth rate. The layer thickness of 100 nm for all samples was calculated according to the growth rate from RHEED intensity oscillations. During GaAs buffer growth, the (2×4) surface reconstructions were observed, indicating the group V termination of the surface. For GaAsBi layer growth at lowered temperatures, (2×1) reconstructions were observed, indicating group V atom termination of the surface, which is called the As-rich GaAsBi growth regime [70, 99]. In the case of samples VGA0101 and VGA0102, the (2×3) reconstructions initially indicate an excess of As [99]. For samples VGA0108, VGA0109, B838, B846, and B847 the observed (2×1) reconstructions were merged.

Table 4.1 Conditions on the 100 nm GaAsBi layers growth: denoting temperatures of the Ga, As, Bi sources: T_{Ga} , T_{As} , T_{Bi} °C ; the layer growth temperature (T_{growth}) and growth rates (v , nm/h).

	T_{Ga} , °C	T_{As} , °C	T_{Bi} , °C	T_{growth} , °C	v , nm/h
VGA0099	886	380	640	425	460
VGA0101	886	380	635	425	460
VGA0102	886	380	630	425	460
VGA0108	886	380	640	370	460
VGA0109	886	360	640	370	460
B838	1045	440	575	320	730
B839	1045	440	570	320	730
B846	1055	450	570	350	845
B847	1055	450	565	360	845

Table 4.2 Parameters of the 100 nm GaAsBi growth including source flux and beam equivalent pressure ratio.

	Ga flux, Torr $\times 10^{-7}$	As flux, Torr $\times 10^{-7}$	Bi flux, Torr $\times 10^{-7}$	As/Ga	Bi/Ga
VGA0099	3.15	3.39	1.02	1.076	0.323
VGA0101	3.29	3.51	1.17	1.068	0.356
VGA0102	3.16	3.37	1.03	1.066	0.326
VGA0108	3.08	2.95	1.45	0.957	0.470
VGA0109	3.08	2.84	1.45	0.922	0.472
B838	3.04	3.21	1.86	1.056	0.612
B839	3.09	3.34	1.56	1.081	0.505
B846	3.50	3.77	1.46	1.077	0.417
B847	3.51	3.83	1.27	1.091	0.362

The Bi content in the grown material was evaluated using HR-XRD measurements. Optical properties were determined using temperature dependent photoluminescence spectroscopy. The *ex situ* surface morphology and crystalline structure of the samples were characterized using AFM. The extracted parameters are presented in Table 4.3. Detailed descriptions of the applied methods are presented in Chapter 3.

Table 4.3 Main technological parameters of the 100 nm GaAsBi layers: E_{PL} - peak position of GaAsBi PL band obtained within 3K and room temperature. Bismuth content has been evaluated from XRD ω - 2θ rocking curves and RSM measurements (%). Relaxation has been evaluated by mapping the parameters of reciprocal lattice and RMS has been determined from AFM measurements.

	E_{PL} RT, eV	E_{PL} 3K, eV	x_{Bi} , % from XRD ω - 2θ	x_{Bi} , % from RSM	Relax- ation, %	RMS, nm
VGA0099	1.09	-	1.1	0.95	0.6	5.878
VGA0101	-	-	0.6	-	-	3.365
VGA0102	1.12	1.19	0.9	-	-	3.648
VGA0108	1.09	-	2.2	2.18	2.3	3.522
VGA0109	1.40	-	0.9	-	-	4.890
B838	0.95	0.74	11.2	10.8	3.3	3.514
B839	1.20	1.1	2.9	3.2	2.9	27.68
B846	0.92	-	7.9	7.55	2.4	6.884
B847	0.99	-	5.9	5.9	3.1	4.378

4.2 Results and discussion

4.2.1 Structure analysis

The lattice parameters of the GaAsBi layer and the Bi amount have been evaluated using the high resolution X-ray diffraction ω - 2θ measurements. Employing a different set of structure growth temperature, As/Ga BEPR, and bismuth flux, layers with Bi content ranging from 0.6% to 11.2% are obtained. Variations of the HR-XRD ω - 2θ rocking curves obtained on the 100 nm thick epitaxial GaAsBi layers with different Bi content grown on GaAs (100) are illustrated in Figure 4.1. The sharp peaks, visible at $2\theta = 66^\circ$ correspond to the GaAs substrate reflections, while peaks on the left are attributed to the epitaxial GaAsBi layers inherent for each sample. The perpendicular lines marking the Bi concentration in the strained GaAsBi compound are shown as guides for the eye. The separation of two peaks within HR-XRD ω - 2θ rocking curves is determined by the mismatch between the GaAsBi layer and

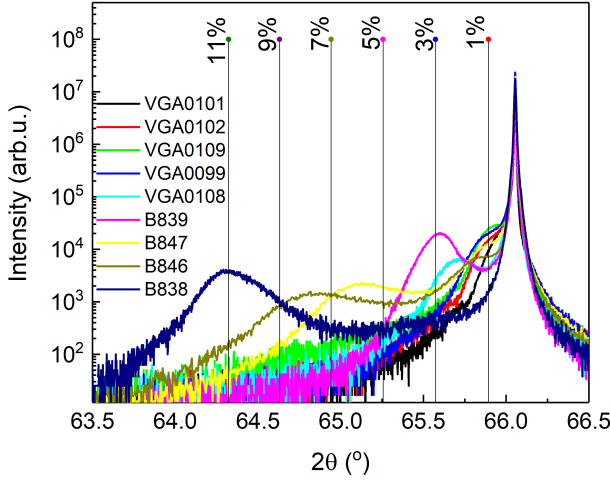


Figure 4.1 HR-XRD ω - 2θ rocking curves of the (004) diffraction peak of 100 nm-thick GaAsBi layers grown onto the GaAs substrate. The vertical lines mark the fully strained GaAsBi bulk compound reflex containing Bi content from 0.6% to 11.2%.

GaAs substrate lattice. Dynamical simulations of XRD scans were used for determination of the layer composition. These simulations were made by assuming the absence of tetragonal distortion. To determine the Bi content (x) within GaAsBi layers the Vegard's law:

$$a_{\text{GaAsBi}} = (1-x)a_{\text{GaAs}} + xa_{\text{GaBi}}, \quad (4.1)$$

relating the lattice constants was employed. Also, the known expressions of strain-tensor components:

$$\epsilon_{xx} = -\frac{\Delta a}{a}, \epsilon_{zz} = 2\frac{C_{12}}{C_{11}}\frac{\Delta a}{a}, \quad (4.2)$$

was assumed. The a_{GaBi} and a_{GaAs} are the lattice constants for $a_{\text{GaBi}} = 6.324 \text{ \AA}$ and $a_{\text{GaAs}} = 5.653 \text{ \AA}$ [35], respectively, x denotes the Bi content, ϵ_{xx} and ϵ_{zz} are the strain components along the x and z axis, respectively. C_{11} and C_{12} are the elastic constants [35]. Thereby, $C_{11} = 12.42 \text{ GPa}$, $C_{12} = 5.14 \text{ GPa}$ for GaAs material and $C_{11} = 7.30 \text{ GPa}$, $C_{12} = 3.27 \text{ GPa}$ for GaAsBi, respectively.

In the XRD scans of the samples with higher Bi concentrations (sam-

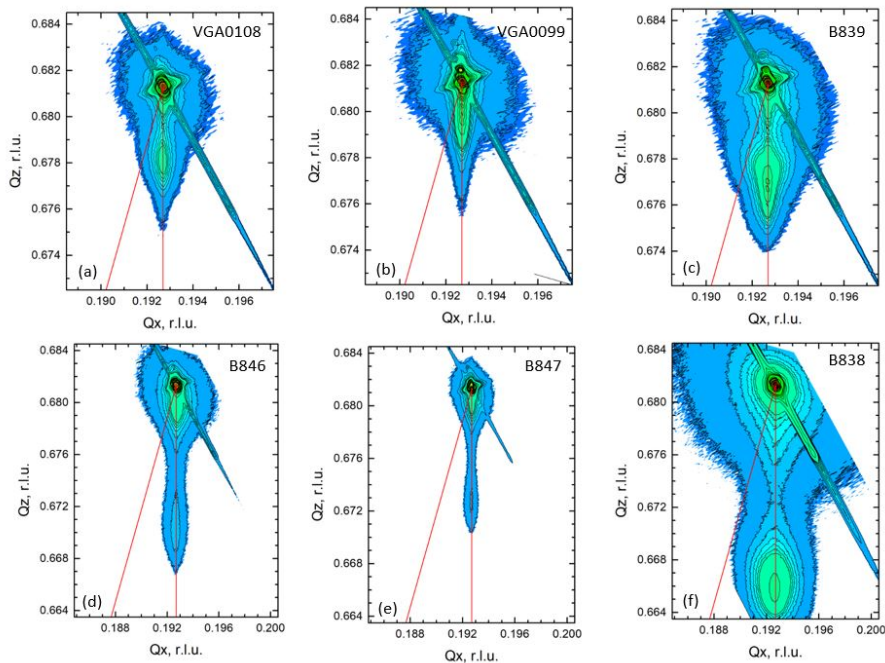


Figure 4.2 HR-XRD reciprocal space maps of the (115) plane measured for GaAsBi layers with (a) 2.2%, (b) 1.1%, (c) 2.9%, (d) 7.9%, (e) 5.9% and (f) 11.2% bismuth content. The perpendicular and tilted solid red lines on this plot correspond to the fully strained and fully relaxed states, respectively. An insignificant shift of the layer peak from vertical lines is due to low relaxation.

ples B838, B846, B847), the peak of the HR-XRD ω - 2θ rocking curves related to the GaAsBi layer appeared to be significantly broader, indicating that either Bi is distributed inhomogeneously or this broadening is related to the lower relaxation of a layer. Weakness of X-ray fringes interference, debated in the literature [69], supports the assumption of the non-uniformity of the Bi content along the growth direction. The relaxation values of GaAsBi layers were obtained from the symmetric and asymmetric scans of the reciprocal space maps over (004) and (115) planes.

The reciprocal space map (RSM) contains reflection from the GaAs substrate (top peak) and from the GaAsBi epitaxial film (bottom peaks). The visible vertical line ascribed to the GaAs reflex indicates that the GaAsBi layer is completely strained and has the same in-plane lattice parameter as the GaAs lattice. The diagonal red line is attributed

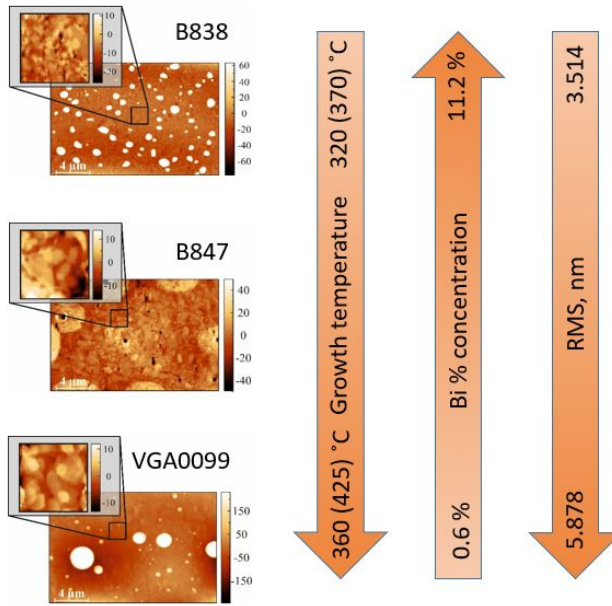


Figure 4.3 Surface morphology images of epitaxial GaAsBi layers with 11.2% (B838), 5.9% (B847), and 1.1% (VGA0099) Bi concentrations, grown using As/Ga pressure ratios of 1.075, 1.091 and 1.076, and substrate temperatures of 320 °C, 360 °C and 425 °C, respectively. The scanned area for images was $2 \times 12 \mu\text{m}^2$ and the highlighted area comprises $2 \times 2 \mu\text{m}^2$. The arrows indicate the summarised tendencies of correlations among the growth parameters for MBE SVT-C-V-2 (MBE Veeco GENxplor R&D) and Bi composition as well as surface roughness.

to the completely relaxed layer. The observed level of relaxation was found to be very low for all the grown samples, ranging from 0.6% to 3.3% for the GaAsBi layers with the lowest and highest Bi content, respectively (Table 4.3). The Bi content in the layers, calculated from RSM, was found to be in good agreement with the values calculated from XRD rocking curve measurements (Table 4.3). Analysis of the RSM peaks attributed to GaAsBi, as shown in Fig. 4.2, suggests that the relaxation of the 100 nm thick GaAsBi layers is caused by an ultra-thin GaAs buffer layer that exhibits sufficient surface roughness. AFM measurements were used to characterize the surface roughness of 100 nm-thick GaAsBi layers *ex situ*.

Several aspects of the AFM images are worth analyzing. Notably, the sample surface shown in Figure 4.3 is separated into areas of the smooth surface region ($2 \times 2 \mu\text{m}^2$) and regions containing pits and droplets on

the surface ($20 \times 12 \mu\text{m}^2$).

The obtained overall RMS roughness is larger for $20 \times 12 \mu\text{m}^2$ and varies from 10 to 40 nm depending on the parameters of As/Ga flux ratio, Bi flux, and growth temperature. The smoother surfaces were obtained at lower growth temperatures (320 – 350 °C) for GaAsBi layers with the higher Bi content. However, roughness of 18 nm was revealed for the 100 nm-thick GaAsBi layers grown at 425 °C. It is important to note that the pits observed in Figure 4.3 were caused by the lack of arsenide in the lattice and due to the formation of the Bi-Ga on the surface. The RMS values of 3.5 nm, 4.4 nm, and 5.9 nm have been evaluated from the $2 \times 2 \mu\text{m}^2$ scans in Figure 4.3 performed for samples B838, B847, and VGA0099, respectively (values for all samples are shown in Table 4.3). Based on these observations, the following assumptions can be deduced. The root-mean-square (RMS) surface roughness of GaAsBi layers is highly dependent on the growth conditions, including the As/Ga flux ratio, the Bi flux, and the growth temperature. The RMS is directly correlated to the growth temperature, while it exhibits a reciprocal function depending on the Bi concentration. Within the optimal growth window, lower growth temperatures and larger Bi flux lead to a greater amount of Bi incorporation and smaller RMS values. While the elevated growth temperatures and the enhanced Bi flux determine the less Bi incorporation and the higher RMS. These assumptions fit well the AFM analysis performed on $2 \times 2 \mu\text{m}^2$ area of GaAsBi layers by varying the determined Bi amounts grown and the applied growth regimes (visualised in Figure 4.3). The similar tendencies of the mentioned variations were reported by Bastiman *et al.* Ref. [70].

The optimal conditions for Bi% incorporation include reduced bismuth composition and elevated growth temperatures, achieved by reducing the Bi flux and enhancing the As/Ga ratio. On the other hand, reduced growth temperatures and As/Ga ratios close to unity, achieved by enhancing the bismuth flux, are more favorable for growing GaAsBi with a Bi amount of more than 6%. This is illustrated by the characteristics of sample B839, where the Bi content reaches only 2.9%.

A small Bi flux of 1.56×10^{-7} Torr and the elevated As/Ga ratio

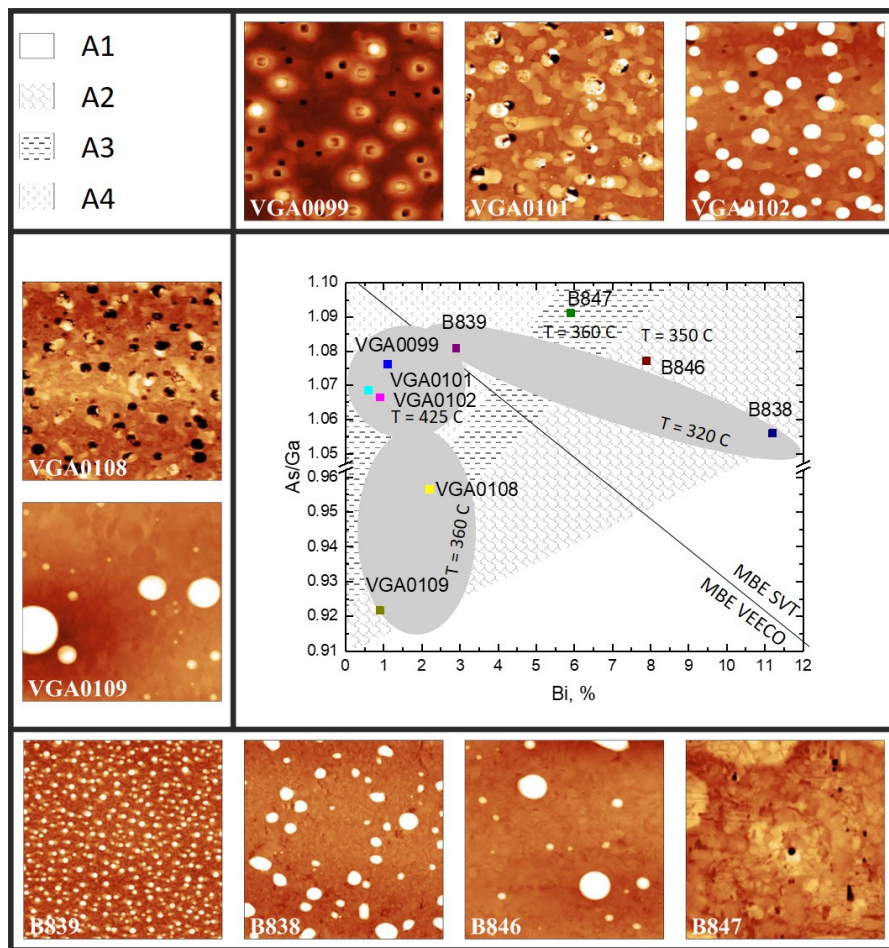


Figure 4.4 Correlations of the As/Ga ratio and Bi% with RMS values extracted from the illustrated AFM images, of layers grown using both the MBE *Veeco GENxplor R&D* and MBE SVT-C-V-2 reactors. The map has been created using different background patterns obtained on: A1 – empty area, A2 - smooth surface with Bi (Bi-Ga) droplets, A3 area with excess of As and pits, and A4 - Ga-terminated surface.

of 1.081 are limiting factors for the incorporated bismuth even when the substrate temperature is rather low (320 °C). The B838 sample was grown under the enhanced Bi flux of 1.86×10^{-7} Torr at a low temperature of 320 °C keeping the As/Ga ratio at 1.056. The highest Bi content of 11.2% was inherent for this sample. The samples grown with MBE *Veeco GENxplor R&D*, VGA0099, VGA0101, and VGA0102 were grown at a higher temperature of 425 °C. As a result, the Bi content in these materials reaches Bi incorporation amounts of 1.1%, 0.6%, and 0.9%, respectively. On the other hand, samples VGA0108 and VGA0109 were grown at 370 °C with the same Bi flux of 1.45×10^{-7} Torr but with different As/Ga BEPR values of 0.96 and 0.92, respectively. It has been revealed that the enhanced amount of Bi is incorporated within the sample grown keeping the As/Ga ratio close to unity. These regularities have been highlighted using the map that represents the incorporated bismuth amount dependence on the As/Ga ratio and growth temperatures, illustrated in Figure 4.4.

To achieve a high Bi content in the lattice, Bi atoms must be supplied before layer growth, which results in the formation of a wetting layer thus favorable for Bi incorporation. Moreover, the presence of a Bi wetting layer improves growth conditions. This has been demonstrated using AFM images of samples grown at high Bi fluxes (1.46×10^{-7} Torr and 1.86×10^{-7} Torr in samples B846 and B838, respectively) and sample VGA0109 with 0.9% Bi (area A2), where no pits are observed on the surface. Formation of Ga-Bi droplets is likely due to the limited presence of As₂ on the Ga-terminated surface, which appears during layer growth, with As/Ga ratios of 0.92 (VGA0109), 1.078 (B846), and 1.075 (B839), respectively. For samples B846 and B839, the As/Ga ratio and surface visualization are comparable, with the growth temperature being the only significant difference: at a lower temperature of 320 °C, more Bi (11.2%) is incorporated than at 350 °C (7.9%). The lower As/Ga ratio at 0.92 in formation of the sample VGA0109 affects the amount of the incorporated Bi in the epitaxial layer (0.9%). The 3D growth was inherent for samples B847 and VGA0108. There, the surface appeared to be smoother than that of samples with the reduced Bi content (RMS 4.4 nm for VGA0108 and 3.5 nm for B847), as obtained for area A3. Although the surface is free of droplets, the excess of As has caused

the formation of pits. The last group of samples, such as VGA0099, VGA0101, VGA0102, and B839, has the less amount of Bi (1.1%, 0.6%, 0.9%, and 2.9%, respectively). However, the latter group of samples was grown at the enhanced As/Ga ratios of > 1.068 (as inherent for areas of A4 type). Samples VGA0099, VGA0101, and VGA0102 were grown at the reduced Bi fluxes of 1.017×10^{-7} Torr, 1.17×10^{-7} Torr, and 1.03×10^{-7} Torr, respectively. It can be deduced from AFM images that the sample surface contains a lot of droplets and pits, indicating the RMS values of 5.9 nm, 3.4 nm, and 3.6 nm, respectively. Insufficient Bi incorporation occurs when there is too small wetting layer (inherent for areas of A3 and A4 types). The density and radius of Bi droplets there depend on the Bi flux. The larger Bi droplets were observed on sample B838, which appeared due to the higher Bi flux of 1.86×10^{-7} Torr. While, sample B839, grown using the reduced Bi flux of 1.56×10^{-7} Torr, exhibited smaller droplets. The same correlation between the wetting layer and Bi droplet formation has been reported by the Bastiman *et al.* and Goldman *et al.* groups in Refs. [70, 101]. The type A1 region in Figure 4.4 illustrates the non-optimal conditions for MBE growth with inherent Bi-Ga droplet formation, as reported in Ref. [34]. The regions are separated for ease of guidance, so the limits are not strictly fixed.

The optimal technological conditions of GaAsBi layer growth have been deduced from the above mentioned investigations. Those optimal conditions strictly depend on three crucial parameters such as substrate temperature, As/Ga BEPR, and bismuth flux. Due to the considerable size difference between the bismuth and arsenic atoms, the bismuth is prone to surface segregation at high temperatures, making it impossible to incorporate bismuth into the GaAs lattice under typical III-V growth conditions. The incorporation of a significant amount of Bi into the GaAs lattice requires the reduced growth temperatures (less than 400 °C) and the diminished arsenic overpressure (pressure ratio of As/Ga close to unity) [8, 35, 43]. Correlations between Bi content, calculated from HR-XRD ω -2 θ rocking curves and RSM as well as the sample growth temperature, are presented in Fig. 4.5. There, the black squares represent values calculated from ω -2 θ measurements, and the red circles represent values evaluated from RSM measurements on samples grown by MBE Veeco GEN x plor R&D (grey area) and MBE

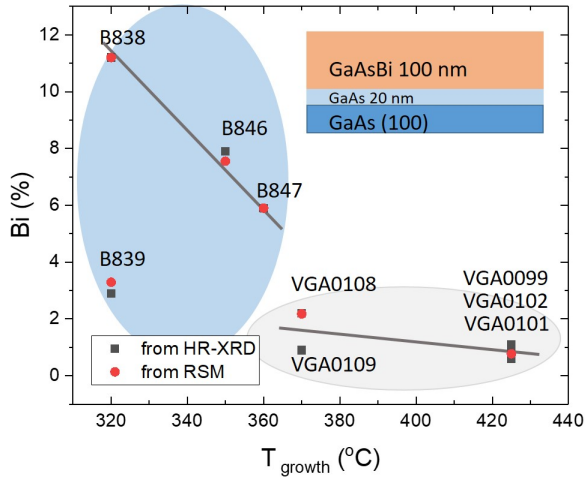


Figure 4.5 Dependence on Bi composition determined from HR-XRD ω - 2θ rocking curves (black squares) and RSM (red circles) measurements performed on epitaxial layers grown by both MBE reactors using different temperatures. The inset illustrates the principle structure of the GaAsBi sample.

SVT-C-V-2 (blue area) reactors. The inset in the figure illustrates the scheme of the 100 nm GaAsBi layer structure. For the samples B839 and B838, the obtained Bi content differed irrespective of the growth temperature, and the Ga flux were the same. The limitations on the incorporated bismuth amount have been deduced from the analysis of the sample B839. There the Bi content reaches only 2.9% due to the reduced Bi flux and the enhanced As/Ga ratio, despite the low substrate temperature. In contrary, the sample B838, grown at a low temperature of 320 °C using the elevated Bi flux and the As/Ga ratio close to unity exhibits better results. The difference in Bi% composition between the VGA0108 and VGA0109 samples comprises values of 2.2 and 0.9, respectively, when As/Ga ratio differs, irrespective of the growth temperatures as well as values of Ga and Bi fluxes are the same. For the VGA0108 sample, the ratio of As/Ga = 0.96 is closer to unity than that for sample VGA0109, where the value of As/Ga comprises 0.92. Therefore, the enhanced amount of bismuth was incorporated into the VGA0108 sample. The correlation between the Bi content and the sample growth temperature shows that more Bi is incorporated at the

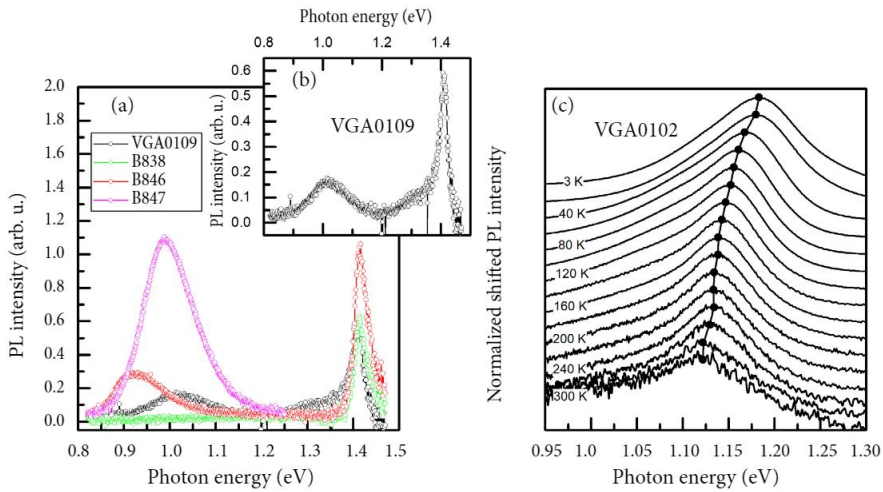


Figure 4.6 RTPL spectra of grown GaAsBi layers with different Bi concentrations (a) and a separated view of the GaAsBi layer with 0.9% of Bi (sample VGA0109) (b). Temperature-dependent PL spectra of the GaAsBi layer with 0.9% of Bi (sample VGA0102) measured at the temperatures ranging from 3 to 300 K (c).

reduced growth temperatures. The As/Ga ratio also plays a significant role in determining the incorporated Bi content. These correlations clearly imply the importance of the careful and simultaneous control of three technological parameters to get the desirable structures. This triad consists of the substrate temperature, the As/Ga BEPR, and the bismuth precursor flux.

4.2.2 Optical characteristics

Firstly, the PL spectra of all investigated 100 nm-thick GaAsBi layers were measured at RT. The selected RTPL spectra are presented in Fig. 4.6(a). It can be seen that the PL spectra of the samples in the B series, grown by SVT-C-V-2 MBE reactor, consist of two PL bands. A higher energy band centered at 1.42 eV is related to the optical transition in the bulk GaAs substrate. A lower energy band was assigned to the optical transitions within the GaAsBi layer. The room temperature GaAsBi-related emission was observed at 0.99 eV and 0.92 eV for the GaAsBi layers with higher Bi concentrations of 5.9% (sample B847) and 7.9% (sample B846), respectively. The higher PL intensity from the

GaAsBi layer containing 5.9% of Bi is related to a possibly lower concentration of non-radiative centers due to a higher growth temperature and a lower Bi concentration.

Unexpectedly, the room temperature PL spectra of VGA series GaAsBi layers containing 0.9% of Bi consisted of three PL components (see Fig. 4.6(b)). The PL band at 1.42 eV was assigned to GaAs, and a low-energy shoulder of the 1.42 eV PL band was assigned to the GaAsBi layer with 0.9% of Bi. The very low PL peak intensity of the GaAsBi layer could be explained by the thermal escape of photoexcited carriers from GaAsBi due to a small conduction band offset between GaAsBi and GaAs. The origin of the PL band at 1 eV could be related to the Bi-rich GaAsBi regions due to the prior introduction of a bismide growth-induced Bi wetting layer. The temperature-dependent PL spectra of the GaAsBi layer containing 0.9% of Bi (sample VGA0102) in the low-energy region are depicted in Fig. 4.6(c). It can be seen that the maximum position of the PL band changes minimally with temperature. It changes from 1.185 eV at 3 K to 1.122 eV at 300 K. Therefore, the thermal band-gap change value of 0.21 meV/K is much smaller than that reported for GaAs (0.52 meV/K [35]) and other conventional semiconductors. Moreover, this supports the assumption that the low-energy PL band is associated with optical transitions in Bi-rich GaAsBi regions.

4.3 Conclusions of the chapter

Formation of the GaAsBi layers with a thickness of 100 nm and Bi content ranging from 0.6% to 11.2% has been demonstrated by using MBE techniques and varying substrate temperatures in the range from 320 °C to 425 °C. The grown layers appeared to be almost compressively strained with relaxation from 0.6% to 3.3%, as revealed using the reciprocal space mapping of grown structures. The optimal growth conditions have been determined to be as follows: the As/Ga BEPR should be close to unity, while a low growth temperature of 320 °C and the enhanced Bi flux of 1.8×10^{-7} Torr should be kept. This growth regime enables to reach the highest contents of 11.2% of Bi incorporation. These findings are particularly relevant to fabrication

of the light-emitting diodes with active region of 100 nm thick bulk GaAsBi material layer.

5. GROWTH AND CHARACTERIZATION OF THE QW GaAsBi/(Al)GaAs STRUCTURES

Growing of high-quality GaAsBi/(Al)GaAs multiple quantum wells is essential for optoelectronic device fabrication. The significant progress has been made in the development of growth technology for GaAsBi quantum structures for optoelectronic applications over the past few years. The electrically driven lasing at room temperature obtained using the GaAsBi multiple quantum well diodes with 6% of Bi amount has been reported [13]. In this chapter, the conventional GaAsBi MQWs with (Al)GaAs barriers and GaAsBi quantum wells with parabolically graded AlGaAs barrier (PGB) structures are discussed. This chapter is also addressed to analysis of the morphological and light emission properties of the different barrier QW structures.

5.1 Growth and analysis of the rectangular GaAsBi quantum well structures

GaAsBi quantum well structures were grown using a *Veeco GENxplor R&D* molecular beam epitaxy system. The 2-inch substrates of SI GaAs(100) were quartered by cleaving. Prior to deposition, the native oxide from the SI GaAs substrate was outgassed at 700 °C under a maximum arsenic flux for 20 minutes. Subsequently, a GaAs buffer layer with a thickness ranging from 240 nm to 650 nm was deposited at 665 – 670 °C. The growth rate of the GaAs buffer layer was around 420 – 800 nm/h (where $T_{Ga} = 866 - 896$ °C) to ensure an atomically

flat surface for epitaxial growth. The thickness of the buffer layer was determined by monitoring the change in reflection of RHEED image from a bulk substrate pattern (1×1) towards the surface reconstruction of GaAs (2×4). The growth parameters applied in the formation of the rectangular quantum well structures are listed in Table 5.1. Source temperatures were set as follows: $T_{Ga} = 866 - 896$ °C, $T_{As} = 370 - 375$ °C, $T_{Bi} = 605 - 640$ °C, and $T_{Al} = 1028 - 1060$ °C. Growth temperatures for the quantum structures were controlled by a thermocouple. The first AlGaAs barrier was grown after the formation of the buffer layer. The As valve was fully opened, and at the same time, the Ga and Al shutters were opened, followed by their closure after a 10 nm thick barrier of AlGaAs had been grown. The AlGaAs growth rate varied in the range of 560 – 970 nm/h, and the Al content within the barrier was changed from 17% to 27% (based on by measuring RHEED oscillations). After the first barrier was grown, the temperature was lowered to 420 – 425 °C, which served as the main temperature regime selected for the quantum well growth. The As cracker valve opening was reduced to yield the As flux corresponding to an As/Ga BEPR close to unity. This ratio varied in the range of 0.874 – 1.083 (see Table 5.2), necessary for GaAsBi growth. For the first period of growth, bismuth played the role of a surfactant in the range of low temperatures. As a result, the sample was exposed to Bi flux for 10 seconds. At this step, the Ga and Bi source cell shutters were opened simultaneously. At the end of the QW growth (reaching a thickness of 7 – 11 nm), the Bi and Ga cell shutters were closed. The GaAsBi growth rate was evaluated from RHEED oscillations and varied in the range of 336 – 640 nm/h. Additionally, the surface reconstruction of (2×1) of QW GaAsBi was determined using the RHEED technique. After QW growth, the growth temperature was raised for the second low-temperature AlGaAs barrier growth by using temperatures in the range 425 – 500 °C. Simultaneously, the As valve was opened at 100 – 150 mils. The low-temperature AlGaAs barrier was grown implementing all the steps employed for QW growth, after the 425 – 500 °C temperature was stabilized. Finally, a 5nm thick GaAs capping was grown on top of the structure. The samples VGA0114, VGA0575, VGA0576, and VGA0577, have been grown forming the barriers made of GaAs.

Table 5.1 Growth temperature parameters kept in formation of the rectangular GaAsBi MQWs, where T_{Ga} , T_{As} , T_{Bi} and T_{Al} denote the temperatures of the sources, (T_{QW}) is the temperature of QW growth, and ($T_{sgrowth}$) is the temperature of the overall structure growth.

	$T_{QW}, ^\circ\text{C}$	$T_{sgrowth}, ^\circ\text{C}$	$T_{Ga}, ^\circ\text{C}$	$T_{As}, ^\circ\text{C}$	$T_{Bi}, ^\circ\text{C}$	$T_{Al}, ^\circ\text{C}$
VGA0113	425	500/670	896	375	635	1037
VGA0114	425	500/670	896	375	635	1037
VGA0116	425	500/670	896	375	640	1037
VGA0117	425	500/670	896	375	635	1037
VGA0118	425	500/670	886	375	625	1037
VGA0119	425	500/670	886	375	625	1037
VGA0121	425	500/670	866	375	625	1028
VGA0130	425	425/670	886	375	625	1028
VGA0575	420	665/665	881	370	605	1060
VGA0576	420	665/665	881	370	605	1060
VGA0577	420	665/665	881	370	605	1060

Table 5.2 Parameters kept in growth of the rectangular GaAsBi MQWs including material flux parameters and the calculated BEPRs.

	Ga flux, $\text{Torr} \times 10^{-7}$	As flux, $\text{Torr} \times 10^{-7}$	Bi flux, $\text{Torr} \times 10^{-7}$	As/Ga	Bi/Ga
VGA0113	3.36	3.58	1.07	1.066	0.319
VGA0114	3.33	3.49	1.03	1.049	0.309
VGA0116	3.33	3.61	1.32	1.083	0.395
VGA0117	3.29	3.55	0.93	1.083	0.283
VGA0118	3.06	3.20	0.76	1.047	0.250
VGA0119	2.79	2.99	0.75	1.073	0.269
VGA0121	1.81	1.94	0.74	1.074	0.411
VGA0130	2.79	3.01	0.76	1.077	0.273
VGA0575	1.23	1.10	0.61	0.895	0.500
VGA0576	1.23	1.10	0.61	0.895	0.500
VGA0577	1.21	1.06	0.61	0.874	0.504

Table 5.3 The main parameters of the produced rectangular GaAsBi MQWs, where N_{QW} denotes the number of quantum wells; x_{Bi} is the bismuth amount (%) evaluated calculating using the *nextnano3* simulation platform, d_{QW} and d_b are widths of the quatum well and barrier, respectively, E_P denotes the PL peak position (in eV) measured on GaAsBi QWs at RT, I_{PL} is the PL intensity obtained at the spectral peak.

	N_{QW}	x_{Bi} , %	d_{QW} , nm	d_b , nm	E_P , eV	I_{PL} a.u.
VGA0113	3	5.2	7	10	1.17	0.55
VGA0114	3	5.4	10	10	0.97	2
VGA0116	3	8.7	7	10	0.97	0.42
VGA0117	3	6.2	7	10	1.11	1.11
VGA0118	3	5.4	7	10	1.16	1.45
VGA0119	3	7.6	7	10	1.03	4.8
VGA0121	3	-	11	10	1	0.03
VGA0130	3	6.6	7	10	1.09	1.45
VGA0575	5	6.2	7	10	1.11	3.88
VGA0576	5	6	7	10	1.12	4.46
VGA0577	5	10.5	7	10	0.90	0.25

The determined parameters of the rectangular GaAsBi quantum wells are listed in Table 5.3. Bismuth content was estimated by fitting the recorded PL spectra using the calculated photon energies, emitted due to electronic transitions. Simulations were performed by employing the *nextnano3*, developed based on a single band effective mass approximation. Material parameters for GaAsBi layers were taken from Ref. [102], and the average value of band-gap reduction was assumed to be 65 meV per 1% of Bi.

5.1.1 Photoluminescence characteristics of rectangular GaAsBi QWs

The variations of parameters of the PL spectra determined for structures of 3 and 5 GaAsBi QWs are illustrated in Figure 5.1. A linear correlation between the PL intensity and the energy of emitted photons was found for 7 nm width QW structures. The position of the PL spectral peak ranged there from 0.97 eV to 1.16 eV. The Bi concentration within these 3 QWs and 7 nm thick GaAsBi has been evaluated using the *nextnano3*. The Bi amount variations in the range from 5.2 % to 8.7%

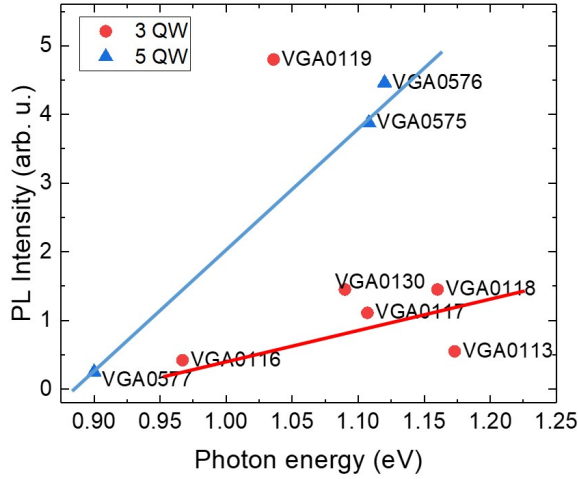


Figure 5.1 Photoluminescence intensity as a function of the PL peak position within PL spectra at room temperature on 7 nm QWs GaAsBi width QW structures containing 3 and 5 QWs. Parameter assignments to various structures can be found in Table 5.3.

have been extracted. Among the 3 QWs structures containing different QW widths, the structure VGA0119 with a 7 nm QW width exhibited the most intensive PL emitted at 1.03 eV photon energy. The Bi concentration of 7.6% has been extracted by simulation of this structure. While, a similar structure VGA0130 with 7 nm QW width exhibited the spectral peak at 1.09 eV photon energy, with a corresponding Bi content of 6.6%. The difference in spectral and Bi amount parameters obtained on these structures can be explained by the changed QW growth rate and Al% in the barrier. Namely, the structure VGA0119 GaAsBi was grown at 290 nm/h with 21% of Al amount, while, the device VGA0130 was grown at 350 nm/h with 16% Al content in the barrier. The device structure VGA0114 GaAsBi/GaAs grown with the 10 nm thick QWs width exhibited the PL spectral peak at 0.97 eV photon energy, while the structure VGA0113 containing GaAsBi/AlGaAs QW of nearly the same width emitted photons with a spectral peak at 1.17 eV. It was deduced from these spectral variations that the wider QW structures determine the weaker PL intensity. Additionally, it was found that the PL intensity scales up with an increased number of QWs, where GaAsBi/GaAs

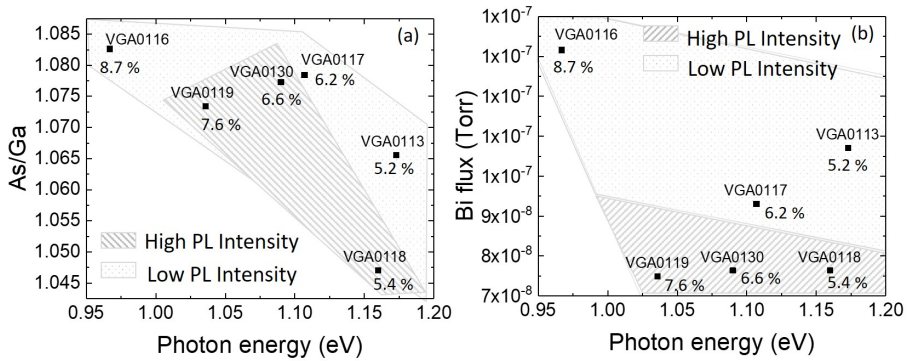


Figure 5.2 Dependence of the PL peak photon energy on growth parameters of As/Ga ratio (a) and Bi flux (b) for rectangular MQW structures with different amount of Bi in the QW. The striped areas in both plots highlight structures with the highest PL intensity.

structures VGA0576, VGA0575, and VGA0577, containing the 5 QWs, exhibited an enhanced PL intensity relative to those structures with 3 QWs. The tendencies between intensity and number of QWs were mentioned in Refs. [13,32,33,72].

The growth of GaAsBi quantum structures is limited by a triada of the optimal technological parameters, namely, the substrate temperature, the As/Ga BEPR, and the bismuth flux. Figure 5.2 represents the parameters of As/Ga ratio and Bi flux as functions of the emitted photon energy corresponding to the PL spectral peak.

Figure 5.2 (a) illustrates the As/Ga ratio dependent on the emitted photon energy within 3 QWs of 7 nm width, grown at 425 °C with Bi flux in the range of $0.75 - 1.3 \times 10^{-7}$ Torr. The window of As/Ga ratio values there ranged from 1.05 to 1.08. The PL intensity is closely related to the amount of Bi incorporated into the structure. Thereby, the QW structure with the higher Bi amount (VGA0116) exhibits a much lower intensity, reaching only 0.42 arb. units. The Bi/Ga ratio also impacts the PL intensity. Thereby, the VGA0113 and VGA0116 structures at Bi/Ga ratio of 0.3 and 0.4, respectively (refer to Table 5.2), exhibited the reduced PL intensity.

The optimal growth regime relative to the Bi flux, in order to obtain the highest PL intensity, is achieved by reducing Bi flux, Figure 5.2(b). It can be deduced from Figure 5.2 (b) that initially the bigger amount

of Bi is incorporated with enhancement of Bi flux. However, at some point within PL intensity dependence on Bi flux, the PL intensity drops down. This might be due to the enhanced formation of Bi clusters or non-radiative recombination centers. At this point of the PL, the excess Bi is no longer incorporated into the QW layer. This excess Bi becomes a generator of defects leading to a drop in the PL intensity. Figure 5.2(b) shows that the structures formed using Bi flux values ranging over BEP values of $(0.7 - 0.9 \times 10^{-7} \text{ Torr and } 0.95 - 1.20)$, respectively) exhibited the highest PL peak intensity and spectral peak photon energies in a wide spectral range of 1.45 – 4.8 eV. However, it has been observed that the reproducibility of the latter structures is low.

5.2 Growth and analysis of parabolic GaAsBi quantum well structures

5.2.1 Parabolic quantum wells

The parabolic quantum wells have unique physical properties that make them attractive from both the theoretical and practical perspectives [103–107]. The first PQWs were grown using MBE on the GaAs/AlAs material system employing the digital alloy grading technique [103]. This technique creates a parabolic effective potential profile by introducing GaAs layers of variable thickness obeying the parabolic law in the AlGaAs alloy of the constant invariable Al content. However, the extremely thin layers with angstrom-range-precision thickness are necessary to have an ideal shaped parabolic potential [108]. The high number of GaAs/AlGaAs interfaces with abrupt changes in Al content can create wavefunction perturbation and increase the carrier scattering time caused by interface roughness. Despite these drawbacks, the digital alloy grading technique has been invented as the primary growing technique to form the PQW structures [103]. A comparative study on the properties of inverse PQWs, performed by Chen *et al.*, showed that digital PQWs were superior to analog PQWs. Additionally, a few works have been done to compare the formation techniques or assess the precision of wide PQWs, using photoluminescence characteristics. The alone work by

Tabata *et al.* Ref. [109] addressed the characterization of the PQWs using photoluminescence, where the undoped PQWs grown using the digital alloy grading technique were analyzed. In contrast, the analog alloy grading technique enables the creation of a parabolic potential by gradually changing the Al content in the AlGaAs alloy [105]. However, this technique lacked attention due to limitations of control over the Al content distribution, necessary for accurate parabolic potential formation [110].

Recently, it has been shown in Ref. [111] that the analog alloy grading technique can be applied as an alternative technological tool to produce the high-precision PQWs for advanced optoelectronic devices. In the later research [111], the MBE growth of the smooth parabolic potential of GaAsBi/AlGaAs QWs has been proposed using the pulsed analog alloy grading (PAAG) technique. The precise calculations of the PAAG design of the AlGaAs PQWs have been reported in the article Ref. [112].

This grading there has been based on the potential energy modulations along the growth direction z and has been modeled using a parabolic function of :

$$x(z) = x \left(\frac{z - z_0}{26.1} \right)^2 + 0.039 \left(\frac{z - z_0}{26.1} \right)^4. \quad (5.1)$$

The PQW width z from 0 to 49.155 nm can be discretized by dividing it into $N = 51$ equally spaced points. The Al content x values at these points can be determined using an equation 5.1. If the interval is to be filled with constant values of x as steps, it is recommended to create the interval equally around the center points $z_{0,n}$. In this way, the beginning of the step is denoted as z_n , and the end of the step (and the beginning of the next step) is denoted as z_{n+1} . The approach of formation of the parabolic Al distribution, shown in Figure 5.3, and, consequently, of barrier potential is illustrated within the inset of Figure 5.3.

According to the simulation data, the Al content x in the barriers should be set to 30%. The width of a single step was fixed to be equal to a doubled AlGaAs lattice constant (approximately 11 or four monolayers). Thus, the simulated aluminum amount within pure GaAs should be decreased from 30% to 0% and then enhanced back to 30%.

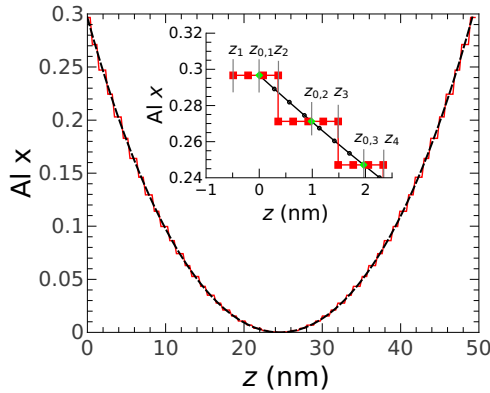


Figure 5.3 Discretization of PQW with 50 steps represented by equally spaced points along the width of the PQW from 0 to 49.155 nm. The inset shows a graphical representation of the discretization process.

5.2.1.1 Growth of the AlGaAs/GaAs parabolic quantum wells

The AlGaAs/GaAs PQW structures, designed using the above discussed model, have been grown employing a *Veeco GENxplor R&D* molecular beam epitaxy system. The 2-inch SI GaAs substrates were oriented within the (001) crystalline plane. These substrates were initially cleaved and outgassed at 700 °C under a maximum arsenic flux for 20 minutes. After the deoxidation procedure, the substrate temperature was maintained at 665 °C for the deposition of a GaAs buffer layer. This 50 nm – 100 nm thick buffer layer was deposited using the growth rates of 280 – 350 nm/h to obtain the relevant quality surfaces. The RHEED pattern obtained following this procedure indicated a strong (2×4) reconstruction, which justified a smooth layer surface and successive layer-by-layer growth. Subsequent to the growth of the buffer layer, the MBE system was programmed to perform the 50-step aluminum content grading along the epitaxial growth direction, as depicted in Fig. 5.3.

The graded PQW barrier was achieved by varying the Al source temperature from 1029 °C to 816 °C and keeping the temperature of the Ga source fixed at 901 – 881 °C. During the PQW growth, the width of each step within the quantum well profile was determined by increasing the exposition time maintained through to the growth rate. There, the Al cell temperature was modified while the Ga source temperature re-

Table 5.4 The numerical values x of the Al content of the versus coordinate Z along growth direction simulated using the 50 steps of discretization.

Step	z_1	x	Step	z_1	x
0	-0.49	0.297	26	25.07	0
1	0.49	0.271	27	26.05	0.002
2	1.47	0.247	28	27.04	0.004
3	2.46	0.224	29	28.02	0.007
4	3.44	0.203	30	29.0	0.011
5	4.42	0.183	31	29.98	0.015
6	5.41	0.164	32	30.97	0.021
7	6.39	0.146	33	31.95	0.028
8	7.37	0.13	34	32.93	0.035
9	8.36	0.114	35	33.92	0.043
10	9.34	0.1	36	34.9	0.053
11	10.32	0.086	37	35.88	0.063
12	11.31	0.074	38	36.87	0.074
13	12.29	0.063	39	37.85	0.086
14	13.27	0.053	40	38.83	0.1
15	14.25	0.0433	41	39.82	0.114
16	15.24	0.035	42	40.8	0.13
17	16.22	0.028	43	41.78	0.146
18	17.20	0.021	44	42.76	0.164
19	18.19	0.015	45	43.75	0.183
20	19.17	0.011	46	44.73	0.203
21	20.15	0.007	47	45.71	0.224
22	21.14	0.004	48	46.7	0.247
23	22.12	0.002	49	47.68	0.271
24	23.1	0	50	48.66	0.297
25	24.09	0	51	49.65	0.3

mained fixed. Due to the significant variation in the flux of group III and the subsequent changes in growth rate, the growth time of each step was recalculated and determined to be in the range of 8 – 13 s. It is important to note that, for the improvement of crystalline quality and material distribution in the PQW, the samples were grown using the lowest growth rate (of 1.0 – 0.5 Å/s) relative to the standard MBE growth regime. Additionally, the interruptions between the growth steps were made to facilitate the arrangement of the crystalline lattice through atom migration and to smoothen the interfaces under arsenic overpressure.

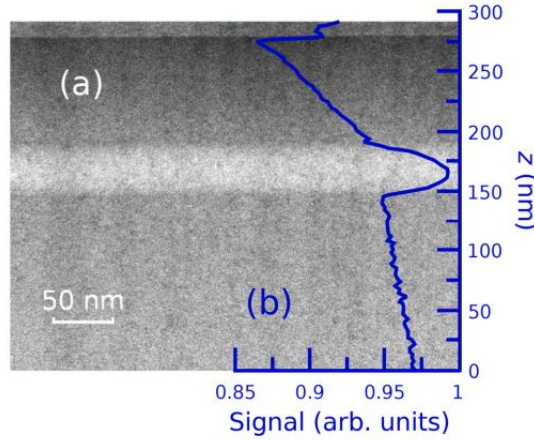


Figure 5.4 (a) STEM image recorded within a cross-section of the analog alloy graded PQW sample.(b) The normalized signal intensity profile (solid blue line) across the scanned area obtained along the growth direction.

This also served for the stabilisation of the Al source temperature. The duration of the interruption stops varied from 90 s to 180 s. The grown PQWs contained a width of 52 nm and were sandwiched between 200 nm thick $\text{Al}_{0.3}\text{Ga}_{0.7}\text{As}$ barriers grown at a rate of 400 nm/h. Finally, the structure was covered with a 5 nm thick GaAs capping layer. The entire growth process was conducted under standard conditions with a substrate temperature of 665 – 670 °C and the arsenic overpressure. This approach enabled to realise the design of an extremely smooth composition profile of the PQWs using the pulsed analog alloy grading (PAAG) epitaxy technique.

The quality of grown PQWs was controlled by STEM imaging, as illustrated in Figure 5.4 The cross-section STEM image in Fig.5.4(a) shows the bright stripe formed 100 nm below the upper-most capping layer. The STEM probe signal across the scanned area implemented along the z axis clearly indicates a parabolic Al content distribution going from the barriers to the center of PQW. As it can be seen from Fig. 5.4(b), the signal profile determined the PQW width being 51.5 ± 0.2 nm. It should be noted, that the increasing background signal raising from AlGaAs claddings is determined by the lamella wedge.

To analyze the quality of the grown structure, excitation power-dependent PL spectra were measured at 3 K using a 266 nm DPSS

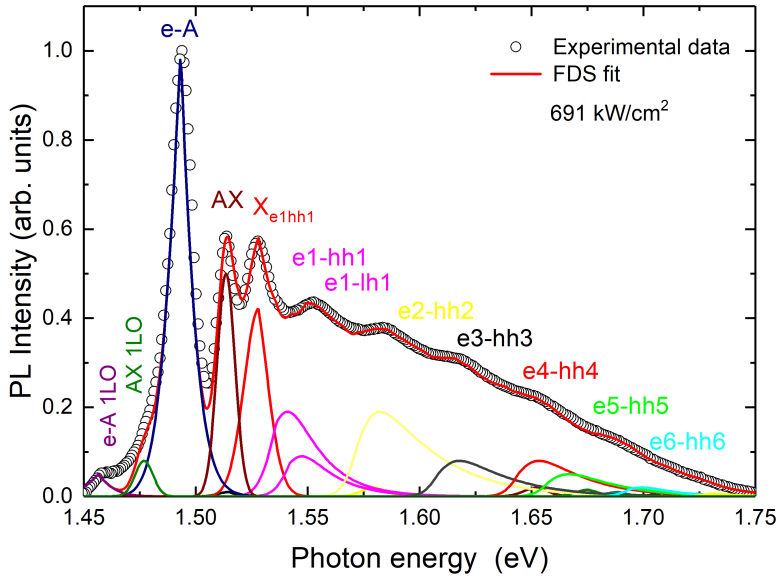


Figure 5.5 The FDS analysis attributes the calculated emission components to the high excitation PL spectrum with PQW related transitions e1-hh1, e1-lh1, e1-hh3, e2-hh2, e3-hh3, e4-hh4, e5-hh5, and e6-hh6.

pulsed laser. The measured PL positions of the identified PQW PL lines allow us to determine whether the grown PQW structure corresponds to the design. Several technological factors may contribute to deviations from the design, and this is particularly evident in analog grading techniques compared to digital grading techniques [110]. For instance, inaccurate Al content grading in the parabolic barrier, fluctuations in well width, and asymmetry of the well due to Al accumulation along the growth direction can all impact the subband arrangement of the PQW and result in a shift in the PL peak position from the expected transition energy.

To assign the PL bands to the specific radiative transitions the FDS calculations were performed on the designed PQW structure [112]. Figure 5.5 illustrates the transition energies together with the estimated peak positions of PL spectral lines.

The spectral range from bulk GaAs and PQW related emission accounts for the high excitation power density of 691 kW/cm². The

peak position at 1.528 eV photon energy is constant with the increasing excitation power density. As deduced by FDS analysis in Fig. 5.5, the line is attributed to PQW $e1 - hh1$ excitons. According to FDS analysis 1.5129 eV, can be attributed to GaAs excitonic recombination AX. Also, it meets the peak position of prominent GaAs excitonic line at 1.513 eV composed of bound GaAs excitons [113]. The dominant spectral line 1.4936 eV photon energy is $e - A$ emission. The visible weak line at 1.4582 eV photon energy is confirmed by FDS to be 1LO phonon replica of $e - A$ emission 35.4 meV what meets the phonon energy for GaAs with reasonable tolerance [114,115]. Note, that for FDS calculation the conventional GaAs phonon energy 36.6 meV was used. Moreover, FDS also finds the 1LO phonon replica of AX line 35.4 meV apart which manifest itself as a low energy shoulder of main $e - A$ recombination line. The GaAs PL originates from the substrate of the sample due to the reabsorption and in part from the capping layer. According to FDS analysis, the PL band at 1.5527 eV photon energy most probably is a superposition of fundamental electron to heavy hole subbands transition $e1 - hh1$, the electron to light hole subbands transition $e1 - lh1$, and electron to 3rd heavy hole subbands transition $e1 - hh3$. This assumption is based on the fact that all 3 FDS calculated bands are in the close vicinity of the peak, however non of it exactly meets the peak position of that PL band. In fact, light holes play substantial role in interband relaxation of excited carriers [109, 110] and parity-allowed $\Delta n = 2$ interband transitions in PQWs lead to “forbidden” transitions with strengths greater than that of “allowed” $\Delta n = 0$ transitions [103]. Other spectral features at the higher energy side in the PL spectrum, correspond to the emission from excited PQW states, namely, from $e2 - hh2$ up to $e5 - hh5$ according to FDS analysis. Therefore we observe the PL band involving the transition between 5 electron subband and 5 heavy hole subband of PQW grown using PAAG technique. Note, that all possible PQW radiative transitions, i.e. intersubband and excitonic as well as parity-allowed $\Delta n = 2$ transitions $e1 - hh3$, $e2 - hh4$, $e3 - hh5$, $e4 - hh6$, were taken into account in FDS calculations. However, only the transitions with considerable importance are discussed and shown in Fig. 5.5. Indeed, the slightly greater mismatch in peak position and rather broad shape of I6 PL band suggests that other

transitions like $e2 - hh4$ with peak energy 1.586 eV or $e2 - lh2$ with peak energy 1.591 eV can also have substantial contribution to the PL emission.

The PQWs grown adapting MBE PAAG technique exhibited a fine electronic energy structure. The PL study demonstrated the excellent agreement between the recorded PL spectra and the designed spectrum of transitions within PQWs. The close-to-ideal PQW fabrication technology enables to form the devices with unique properties.

5.2.1.2 Growth of the parabolic GaAsBi quantum wells

The developed technology of the parabolic QW growth enabled the formation of GaAsBi QWs inserted between AlGaAs PGBs. The growth process involved the interrupted stop of the GaAsBi QW growth after the deposition of the first barrier layer. This processing was implemented by the substrate temperature lowering to 415 – 425 °C and a reduction of the As/Ga BEPR to values of 0.77 – 1.03. Later, the temperature was set to parameter values inherent for QW growth, and the samples were exposed to Bi flux for 10 s. Ga, As, and Bi source shutters were opened to perform the QW growth. The QW growth process was terminated after 5 – 14 nm thick QW deposition. The entire structure was grown under standard conditions keeping the substrate temperature at 665 – 670 °C with arsenic overpressure. This technology approach allowed the designing of an extremely smooth composition profile of the PQWs similar to those obtained by the pulsed analog alloy grading epitaxy. The device structures VGA0361, VGA0436, and VGA0438 contained the MQWs of PGBs consisting of three GaAsBi QWs of 10 nm thick and GaAs barriers with an 8 nm width. For comparison, the device structure VGA0191 contained the double parabolic structure, which means that two parabolic structures with GaAsBi SQWs were successively grown one after the other (see Table 5.5).

Table 5.5 The temperature parameters kept during the growth of parabolic GaAsBi QWs, where (T_{QW}) is the temperature of QW growth, ($T_{sgrowth}$) represents the growth temperature in fabricating of the overall structure, (T_{Ga1}/T_{Ga2}) indicate the temperatures of Ga sources, (T_{As}) denotes the temperature of the Bi source, (T_{Bi}) denotes the temperature of the As source and (T_{Al}) denotes the temperature of the Al source.

	$T_{QW},$ °C	$T_{sgrowth},$ °C	$T_{Ga1}/T_{Ga2},$ °C	$T_{As},$ °C	$T_{Bi},$ °C	$T_{Al},$ °C
VGA0129	425	670	853/901	375	630	1012
VGA0143	425	670	851/901	380	630	1018
VGA0144	425	665	851/901	380	630	1018
VGA0145	425	665	851/901	380	630	1021
VGA0163	420	665	851/881	380	630	1029
VGA0172	415	665	851/881	380	630	1029
VGA0174	420	665	851/881	380	640	1029
VGA0176	420	665	851/881	380	640	1029
VGA0184	420	665	851/881	380	640	1029
VGA0333	425	665	851/881	340	630	1029
VGA0339	422	665	851/881	340	630	1029
VGA0341	425	665	851/881	340	650	1029
VGA0342	420	665	851/881	340	640	1029
VGA0349	420	665	851/881	340	620	1029
VGA0315	425	665	851/881	390	630	1029
VGA0328	422	665	851/881	390	630	1029
VGA0191	420	665	851/881	380	640	1029
VGA0361	420	665	851/901	340	610	1029
VGA0436	420	665	851/901	350	640	1026
VGA0438	420	665	851/901	350	640	1026

5 GROWTH AND CHARACTERIZATION OF THE QW GaAsBi/(Al)GaAs STRUCTURES

Table 5.6 Parameters kept within growth of the parabolic GaAsBi QWs, where flux values of Ga, As and Bi sources are denoted in units of Torr $\times 10^{-7}$ and also the the ratios of As/Ga and Bi/Ga are listed.

	Ga flux, Torr $\times 10^{-7}$	As flux, Torr $\times 10^{-7}$	Bi flux, Torr $\times 10^{-7}$	As/Ga	Bi/Ga
VGA0129	1.40	1.22	0.93	0.873	0.664
VGA0143	1.26	1.22	0.83	0.965	0.735
VGA0144	1.27	1.07	0.82	0.839	0.650
VGA0145	1.24	1.22	0.95	0.982	0.178
VGA0163	1.79	1.85	0.77	1.034	0.428
VGA0172	1.79	1.65	0.82	0.922	0.456
VGA0174	1.77	1.53	0.79	0.864	0.440
VGA0176	1.75	1.59	0.95	0.907	0.542
VGA0184	1.70	1.56	0.99	0.917	0.587
VGA0333	1.23	0.95	1.26	0.770	1.021
VGA0339	1.96	1.51	0.56	0.772	0.288
VGA0341	1.98	1.36	2.17	0.689	1.099
VGA0342	1.94	1.40	1.74	0.722	0.898
VGA0349	1.76	1.92	0.63	0.990	0.324
VGA0315	1.94	1.50	0.97	0.856	0.550
VGA0328	1.94	1.05	1.26	0.876	0.648
VGA0191	1.70	1.50	0.84	0.883	0.496
VGA0361	1.86	1.72	1.19	0.923	0.642
VGA0436	1.66	1.58	1.76	0.951	1.058
VGA0438	1.66	1.58	1.75	0.951	1.054

Table 5.7 The main technological parameters kept during growth of the parabolic GaAsBi QWs, where N_{QW} is the number of quantum wells, Bi denotes the bismuth content evaluated by using the *nextnano3* software platform, d_{QW} and d_b are the quantum well and barrier width (nm), respectively, E_P is the photon energy for the PL spectral peak position, recorded at room temperature, I_{PL} is the PL intensity registered at the spectral peak.

	N_{QW}	Bi, %	d_{QW} , nm	d_b , nm	E_P , eV	I_{PL} , a.u.
VGA0129	1	6.6	7	-	1.08	50
VGA0143	1	3.5	7	-	1.25	220
VGA0144	1	6.8	7	-	1.07	61
VGA0145	1	4.4	5	-	1.21	315
VGA0163	1	5.5	10	-	1.13	274
VGA0172	1	3.6	10	-	1.23	87
VGA0174	1	5.4	10	-	1.14	12.7
VGA0176	1	6.7	10	-	1.06	94.74
VGA0184	1	3.7	10	-	1.23	224.60
VGA0333	1	2.6	14	-	1.28	6.78
VGA0339	1	2.6	8	-	1.29	29.89
VGA0341	1	3.9	8	-	1.22	13.99
VGA0342	1	3.1	10	-	1.26	17.63
VGA0349	1	3.1	10	-	1.27	193.60
VGA0315	1	5.1	8	-	1.19	7.64
VGA0328	1	5.0	8	-	1.17	162.7
VGA0191	1+1	-	10	-	1.08	122.80
VGA0361	3	5.9	10	8	1.11	98.26
VGA0436	3	5.1	10	8	1.15	66.22
VGA0438	3	6.2	10	8	1.09	55.31

Table 5.7 presents the calculated and measured parameters of GaAsBi PQWs. A detailed description of all the methodologies used is available in Chapter 3. Bismuth content was estimated by fitting calculated electronic transition energies to that recorded within PL spectra. The simulations were performed using *nextnano3* software with a single-band effective mass approximation. The material parameters for GaAsBi layers were obtained from [102], and an average value of 65 meV per 1% of Bi was assumed for the band-gap reduction.

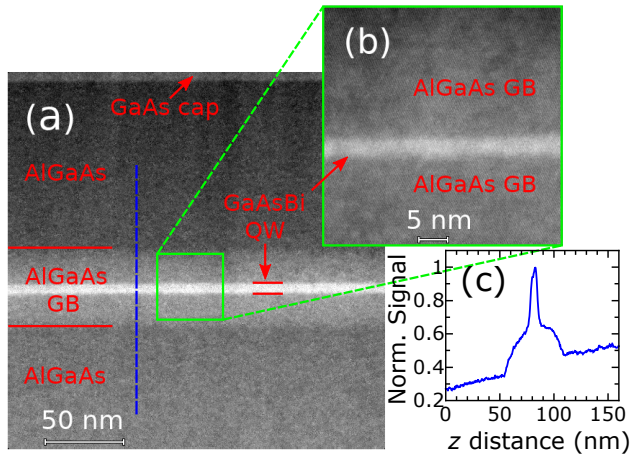


Figure 5.6 (a) Cross-section STEM images of GaAsBi SQW with AlGaAs PGBs. The enlarged area around GaAsBi SQW is presented in panel (b), while panel (c) shows the profile of the structure extended over a distance marked by a blue line within abscissa axis.

5.2.2 Characteristics of the parabolic GaAsBi QWs

5.2.2.1 STEM imaging

Samples for STEM imaging were prepared using the FIB method within FEI Helios Nanolab 650 dual beam SEM/FIB instrument. The sample thickness was estimated to be 40 ± 10 nm measured close to the capping layer, and getting slightly thicker onwards of a wedge, which can be deduced from Fig. 5.6 by considering the STEM images.

The STEM image of GaAsBi QW with parabolic AlGaAs barriers is shown in the Fig. 5.6 (a). The parabolic AlGaAs barrier layer is visible over the range of 50 nm. The capping layer of GaAs is also visible on the top. The enlarged area around the GaAsBi QW and its width of it is around 5 nm can be deduced from Fig. 5.6 (b).

5.2.2.2 Morphology characterisation

The AFM study of samples containing standard rectangular and step-like GaAsBi/AlGaAs QW structures revealed the surface roughness to be around 1 nm by an order of magnitude, which also depends on bismuth concentration. The morphology pictures of three GaAsBi SQWs with AlGaAs PGBs are shown in Figure 5.7. These structures

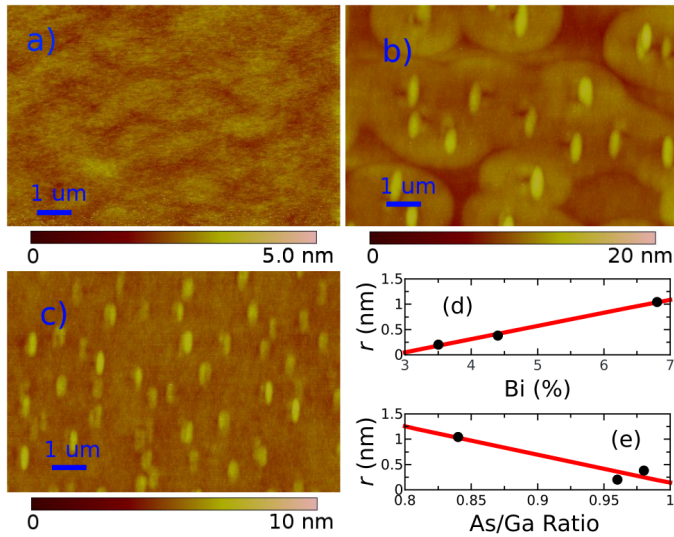


Figure 5.7 AFM surface images for samples with smallest surface roughness r 0.2 nm (a), medium surface roughness r 0.4 nm (b), and largest surface roughness r 1.0 nm (c). The surface roughness r dependence on Bi content in the QWs (d) and surface roughness r dependence on Ar/Ga ratio (e). In panels (d) and (e), the points are the experimental data and red lines show the linear fits.

were grown at the same temperature of 425 °C using different As/Ga BEPRs ranging from 0.84 to 0.98 thus, consequently, containing different Bi contents namely VGA0143 – 3.5%, VGA0144 – 6.8%, and VGA0145 – 4.4%.

The AFM scans show a rather smooth surface of roughness of less than 1.1 nm for all the samples. This proves a good crystal quality of the grown layers obtained by maintaining optimal growth conditions (i.e. As/Ga BEPR). The slightly different growth conditions resulted in differences in Bi amount in the QW with parabolic barriers. Indeed, the sample with the largest surface roughness contained the biggest amount of Bi in the QW, as implied from the PL peak position (see Fig. 5.7(d)). The roughness correlation with Bi content and roughness dependence on As/Ga BEPR are shown in Figures 5.7(d) and (e), respectively. These characteristics imply the increase of Bi amount within a well and reduction of As overpressure during the growth with enhancement of the surface roughness. These predictions are in good agreement with the conclusions of Puustinen *et al.* [116].

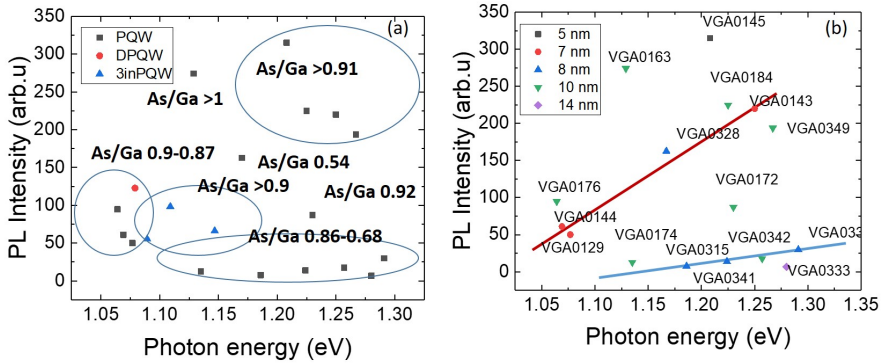


Figure 5.8 The dependence of PL intensity on PL peak position at room temperature for all investigated PQW structures in Table 5.7. Panel (a) represents the dispersion of PL spectral peak positions in correlation with As/Ga BEPRs, while (b) panel displays PL spectral peak intensities obtained for PQW structures with different QW widths of 5, 7, 8, 10, and 14 nm.

PQW structures also have a limited range of the optimal technological parameters namely, the substrate temperature, the As/Ga BEPR, and the Bi flux. Figure 5.8 illustrates the dependence of PQW PL intensity on PL peak photon energy. Different symbols represent different types of PQW in Figure 5.8(a). The trends can be deduced from Figure 5.8 those indicate that structures with As/Ga ratios closer to unity exhibit enhanced PL intensity. Also, the structures grown using As/Ga ratios in the range of 0.87 – 0.9, contain the enhanced amount of the incorporated Bi. Additionally, it can be deduced from Figure 5.8(b) that quantum well width correlates with PL intensity. The thinner quantum well is, the higher the PL intensity is observed, as in the case of VGA0145 with 5 nm QW width, which had a PL intensity of 315 arb. units, compared to VGA0333 with 14 nm width, which had a PL intensity of only 6.78 arb. units. The trend observed in structures with QW widths of 7 nm and 8 nm is that higher energy levels correspond to less Bi incorporation and higher PL intensity, whereas lower energy levels correspond to more Bi incorporation and lower PL intensity. However, for structures with 10 nm QWs, the correlation is dispersed. For VGA0315 and VGA0328, the As/Ga ratio is comparable, but the Bi flux differs, with 0.97×10^{-7} Torr and 1.26×10^{-7} Torr, respectively. As a result, VGA0328 has a higher PL intensity of 162.7 arb. units For VGA0163 and VGA0174,

growth parameters are comparable, with similar Bi flux numbers, but they differ in As/Ga ratio, which is 1.03 and 0.86, respectively. As a result, VGA0163 has an As/Ga BEPR closer to ideal technological conditions, and the PL intensity reaches 274 arb. units. For VGA0172 and VGA0176, the PL intensity is comparable in numbers, but the amount of Bi incorporated differs, with 3.6% and 6.7%, respectively. The QW in sample VGA0172 is grown at 415 °C, while the structure VGA0176 is grown at 420 °C.

The tendencies of variations of the performance characteristics obtained for PQW structures are similar to those determined for rectangular structures when comparing the dependences on As/Ga BEP ratio and Bi flux against photon energy, as shown in Figure 5.9. The structures with the highest PL intensity are dispersed in the 0.86 – 1.03 As/Ga BEPR range of values, as marked by the striped area for eye guidance. The structures with 8 nm QW width grown at reduced As/Ga BEPRs indicate the lower PL intensity, while structure VGA0333 with 14 nm width exhibited the reduced PL intensity due to the highly disordered distribution of Bi content. Looking at the dependence on Bi flux in Figure 5.9(b), the PQW structures grown using a reduced Bi flux exhibited the enhanced PL intensity. For the 3inPQW, which has three QWs in parabolic structures, in formation of the MQW parabolic structures, the larger Bi flux is required to incorporate Bi, ranging from 5.1% to 6.2% amount. This type of structure may have each QW with a channel where carriers combine and have radiative recombination. For the structure VGA0333 with 14 nm width, a higher Bi flux is needed for Bi incorporation. The area with the highest intensity for different GaAsBi SQW widths in PQW is marked for eye guidance and is in the range of $0.6 - 0.9 \times 10^{-7}$ Torr.

5 GROWTH AND CHARACTERIZATION OF THE QW GaAsBi/(Al)GaAs STRUCTURES

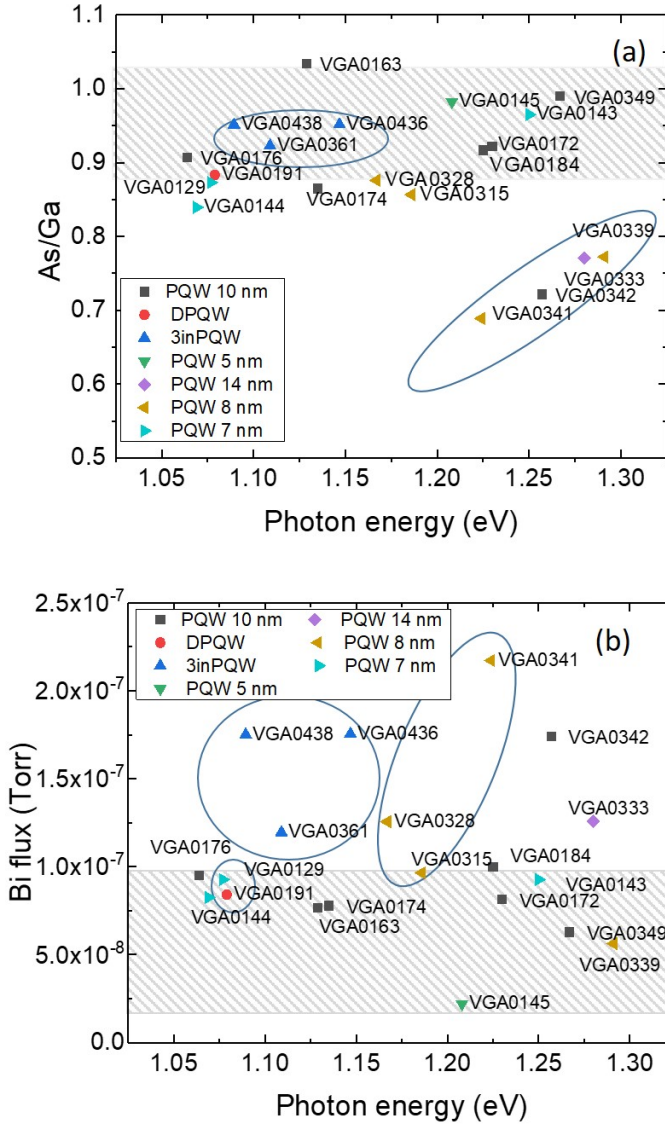


Figure 5.9 PQW growth parameters As/Ga BEPR (a) and Bi flux (b) dependent on PL peak photon energy. Striped areas of both plots mark structures with the highest PL intensity.

5.3 Comparison of QW structure characteristics with different barrier design

Three types of GaAsBi SQW and MQW structure designs were compared. The first design involved standard rectangular MQWs with AlGaAs barriers (approximately 30% Al), as shown in Figure 5.10(a). The second design featured a rectangular QW surrounded by two- or three-step AlGaAs barriers, with either AlGaAs (Figure 5.10(b)) or pure GaAs (Figure 5.10(c)) at the bottom, with 15% and 30% Al content in the barriers. The third design consisted of a GaAsBi SQW inserted between AlGaAs PGBs, with the Al content grading from 30% at the top to 0% at the bottom of the barriers. The structure design of GaAsBi SQW with AlGaAs PGBs is depicted in Figure 5.10(d). The growth of structures have been previously described in chapter devoted to GaAsBi/(Al)GaAs QWs. The main technological parameters for structure formation are presented in Table 5.8.

Table 5.8 The main technological parameters of GaAsBi/(Al, Ga)As QW structures. The most of abbreviations denoting the technological parameters have the same meaning as those mentioned within titles of the previous tables. Here, the rectangular (1) type of QWs, the QWs with step-like barriers (2), and with AlGaAs PGBs (3) is denoted additionally [117].

	Bi, %	As/Ga	N_{QW}	d_{QW} , nm	E_P , eV	I_{PL} , a.u.	Type of QW
VGA0113	5.2	1.07	3	7	1.17	0.55	1
VGA0114	5.4	1.05	3	10	0.97	2	1
VGA0116	8.7	1.08	3	7	0.97	0.42	1
VGA0118	5.4	1.05	3	7	1.16	1.45	1
VGA0119	7.6	1.07	3	7	1.03	4.8	1
VGA0141	3.6	1.04	1	7	1.27	7.5	2
VGA0142	6	0.96	1	7	1.11	5	2
VGA0129	6.6	0.9	1	7	1.08	50	3
VGA0143	3.5	0.96	1	7	1.26	220	3
VGA0144	6.8	0.84	1	7	1.07	62	3
VGA0145	4.4	0.98	1	5	1.21	315	3

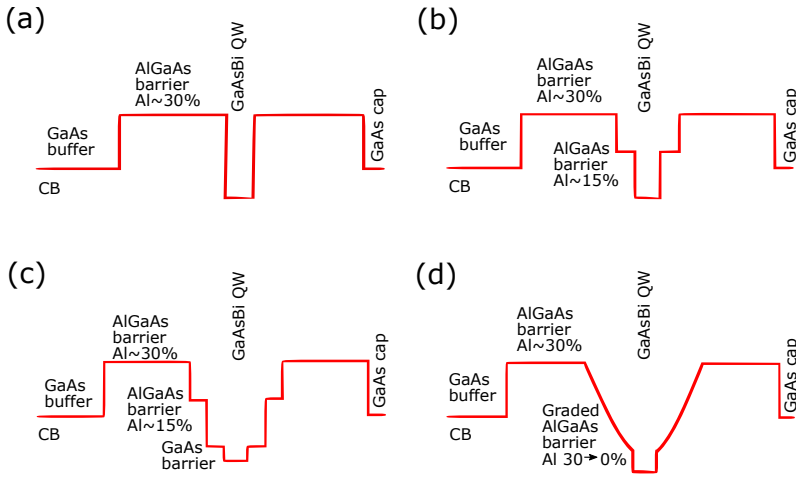


Figure 5.10 Design types of GaAsBi/(Al, Ga)As QW structures: (a) rectangular GaAsBi QW, (b) and (c) QW with the step-like barriers, and (d) GaAsBi QW with the PGBs. MQW structures were also included [117].

5.3.1 Characteristics of the room temperature photoluminescence

The PL spectra were measured at room temperature using 532 nm excitation wavelength and 19 mW output power diode pumped solid-state laser as the excitation source. PL signal was detected by InGaAs thermoelectrically cooled photodetector. Figure 5.11 shows the PL spectra peak position of QWs structures grown at the same substrate temperature (425 °C), As/Ga BEPR ranging from 0.84 to 1.08 and Bi effusion cell temperature T_{Bi} ranging from 625 °C to 640 °C. The PL spectra of all 3 types of samples consist of two PL bands: higher-energy PL band at 1.42 eV is related to emission from GaAs and lower-energy PL band can be assigned to optical transitions in GaAsBi QWs. The room temperature PL measurements demonstrate quite weak emission from standard rectangular barriers of GaAsBi QWs. Sample VGA0116 containing the largest bismuth content (up to 9%) exhibits the PL peak at spectral range of about 0.97 eV. However, one can point out that the relationship is ambiguous as the radiative recombination efficiency is very sensitive on the growth conditions. Even growth under the same conditions can result

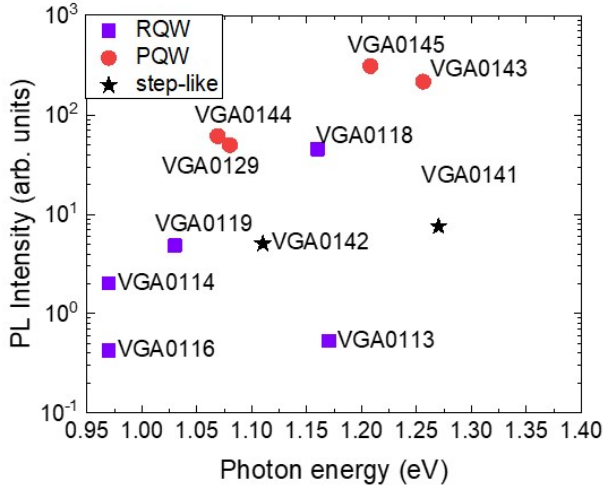


Figure 5.11 The room temperature PL spectra peak positions of GaAsBi QW structures with parabolic AlGaAs barriers, step-like AlGaAs barrier, and rectangular AlGaAs barriers dependence on PL intensity. The PL intensity drops down increase of emission wavelength which corresponds to higher Bi content within the QWs.

the QW emission intensity variation by several times. Typically, the PL intensity diminishes with Bi incorporation [26]. In our case, the sample VGA0113 containing smallest Bi amount exhibits 8 times lower PL intensity in comparison to emission of sample VGA0119 (GaAsBi MQW with 7.6%).

The second barrier layer with lower Al content was introduced to increase the carrier trapping from barrier layers into QWs. The PL peak position of samples with different Al content in the barriers is shown in Figure 5.11 (step-like). It demonstrates emission spectra for two 7 nm thick GaAsBi QW structures with step-like barriers grown under similar conditions (substrate temperature 425 °C and $T_{Bi} = 630$ °) although changing As/Ga BEPR from 0.96 (VGA0142) to 1.04 (VGA0141). From Figure, one can see, that VGA0142 sample which was grown supplying lower As flux exhibits the PL peak in the vicinity of 1.1 eV, while the emission of VGA0141 sample (grown with higher As flux) 1.27 eV. The PL intensity measured for both samples reveals that the introduction of second barrier layer allows better control over the optical properties,

although the radiative recombination efficiency is still insufficient for practical applications.

Nevertheless, the general trend is visible on Figure 5.11. The PL intensity tends to decrease with increase of Bi content peak wavelength. Moreover, the PL intensity is almost independent on the number of QWs, i.e. only small improvement in photoluminescent properties was observed by increasing QW quantity. On the other hand, it is known that the PL intensity of rectangular QWs can be controlled by Al content in the barriers [53]. The significant PL enhancement was achieved for QWs with higher than 30% of Al in the barriers.

The study of optical properties showed that radiative recombination efficiency enhances significantly in GaAsBi SQW with AlGaAs PGBs. Samples were grown at the same substrate temperature of 425 °C and constant Bi flux only at different As/Ga BEPR (see table 5.8). Therefore, Bi content in SQW varied from 3.5% to 6.8% which was evident by PL peak position at around 1.26 and 1.07 eV. The emission from such SQW design is more than 50 times intensive if compare to rectangular MQW and SQW structures with step-like barrier, as it can be seen in Figure 5.11.

5.3.2 Temperature and excitation power dependent photoluminescence

Temperature-dependent PL spectra of GaAsBi QW with PGBs are shown in Figure 5.12(a). The PL band at around 1.1 eV is attributed to the emission from GaAsBi QW with around 6.6% of Bi in the well. The PL intensity gradually decreases with temperature from 3 to 300 K with the measured 20 K step except for temperatures 120 and 140 K. The PL intensity of GaAsBi QW band suddenly increases at the temperature of 140 K together with the beginning of PL peak position blueshift and decreases further on up to 300 K. The PL peak position dependence on temperature is shown in Figure 5.12(b). The S-shape character of PL peak position dependence on temperature indicates the carrier localization effect [118]. The initial red-shift is attributed to the carriers redistribution over localized states through the hopping to lower energy states. The blue-shift appears due to the thermalization of carriers which re-

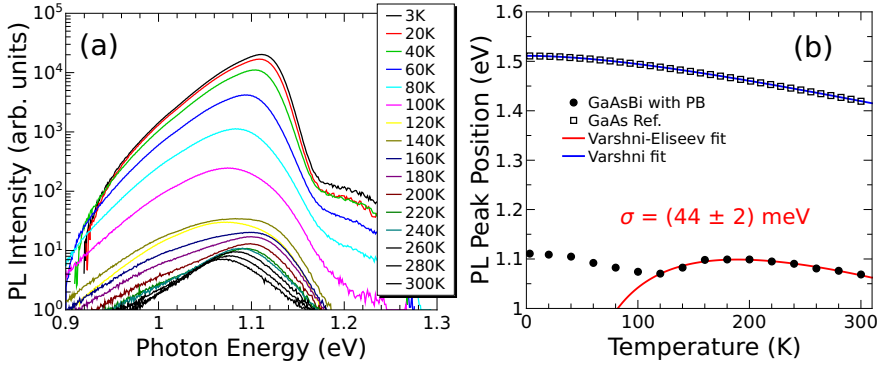


Figure 5.12 PL spectra dependence on temperature of the band attributed to GaAsBi quantum well of VGA0129 sample (a). PL peak position dependence on temperature of GaAsBi QW band (dots) and GaAs reference (empty squares). The best fit of higher temperature PL peak blueshift with combined Eq. (5.2) and (5.3) functions yielded the random potential field fluctuations scale σ 44 meV. The peak dependence on temperature of GaAs reference was fitted using function 5.3.

sults in filling the unoccupied higher energy states. This effect is overtaken by the band-gap shrinkage with further increasing temperature. The blue-shift of the S-shaped PL peak dependence on temperature can be fitted using the function:

$$E_P(T) = E_g(T) - \frac{\sigma^2}{k_B T}, \quad (5.2)$$

where σ is the dispersion of Gaussian density of states in the randomly disordered localizing potential field for carriers [119]. The $E_g(T)$ is the fundamental band-gap shrinkage of the semiconductor, which can be described by the empirical Varshni function [120].

$$E_P(T) = E_0(0) - \frac{\alpha T^2}{\beta + T}, \quad (5.3)$$

where $E_0(0)$ is the band-gap E_g at 0 K temperature limit, α and β are the Varshni fitting parameters.

The PL peak position dependence on temperature of pure GaAs as a reference is presented in Figure 5.12(b). The data of GaAs were best fitted using Varshni function with parameters $E_0(0) = 1.5110 \text{ eV}$, $\alpha = 0.52 \text{ meV K}^{-1}$, and $\beta = 212 \text{ K}$. The fitting parameters are in good agreement with those reported for GaAs before [35]. For S-shaped PL peak po-

sition temperature dependence the best fitting parameters combining equations 5.2 and 5.3 were $E_0(0) = 1.30$ eV, $\alpha = 0.87$ meV K⁻¹, and $\sigma = 44$ meV while β was set constant to 204 K. The data of non-graded GaAsBi MQW PL peak position dependence on temperature was fitted using only Varshni equation 5.3 taking into account the range between 3 K and 160 K due to the deviation from the trend in the higher temperature range. The best fitting parameters were achieved as $E_0(0) = 1.209$ eV, $\alpha = 0.70$ meV K⁻¹ while β was set to constant 204 K. Note, that fitting of higher temperature range with combined equations 5.2 and 5.3 have failed to produce reasonable parameter set. Therefore, the PL peak position of sample VGA0118 deviation from expected monotonous red-shift with temperature should be attributed to involvement of other PL processes, such as defect related PL, rather than localization effect. The best fitting parameters of PL peak position versus temperature data using Varshni or combined Varshni–Eliseev models for other samples are presented in Table 5.9.

Table 5.9 Best fitting parameters of PL peak position versus temperature curve using Varshni equation 5.3 or combined Varshni–Eliseev equations 5.2 and 5.3. Here, the rectangular (1) type of QWs, the QWs with step-like barriers (2), and with AlGaAs PGBs (3) is denoted additionally [117].

Samples	Type of QW	E_0 (eV)	α , meV K ⁻¹	β , K	σ , meV
GaAs	Substrate	1.51	0.52	212	0
VGA0118	1	1.21	0.70	204	0
VGA0142	2	1.15	0.99	204	0
VGA0129	3	1.30	0.87	204	44
VGA0144	3	1.24	0.70	204	36
GaAs	Vurgaftman <i>et al.</i> [35]	1.52	0.54	204	0

The room temperature PL spectra dependence on photoexcitation power allows the insight into carrier recombination mechanisms behind the PL. The general of the spectra of GaAsBi QW maintain single band without the shift of the peak position and noticeable broadening in the range of excitation power density increase up to two order of magnitude

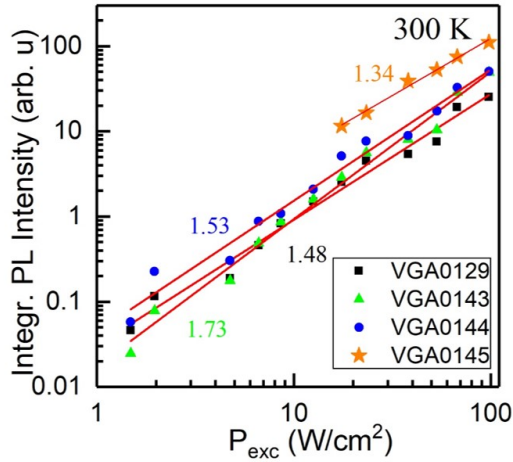


Figure 5.13. Integrated PL intensity dependence on excitation power in double logarithm scale for SQW with PGBs samples (dots) and the fitting with power law function (lines).

at the small/medium excitation conditions. The integrated PL intensity dependence on excitation power density in double logarithm scale in Figure 5.13 shows the linear increase. The slope of the line was estimated by fitting the experimental data with power law $I_{PL} \propto P_{exc}^b$ and the best fit yielded b between 1.5 and 1.8 for samples VGA0129, VGA0143 and VGA0144, as shown in Figure 5.13. Note that these samples contain quite different Bi amount in the QWs 6.6%, 3.5% and 6.8%, respectively. It suggests that band-to-band recombination of uncorrelated carriers is dominant and Auger non-radiative recombination processes can be neglected. Moreover, it confirms that analyzed PL band originates from GaAsBi QWs rather than due to defects or impurities related radiative recombination.

The index b value around 1.6 indicates that at room temperature the radiative recombination is of comparable rate with non-radiative recombination. Indeed, if non-radiative recombination is dominant then the index b equals 2 [76]. In contrast to other samples, the PL spectra of VGA0145 sample show very different behavior with increasing photoexcitation power. The slope b with the value of 1.3 indicates that radiative recombination is dominant even at room temperature. The strong evidence of filling of states with photoexcited carriers is the broaden-

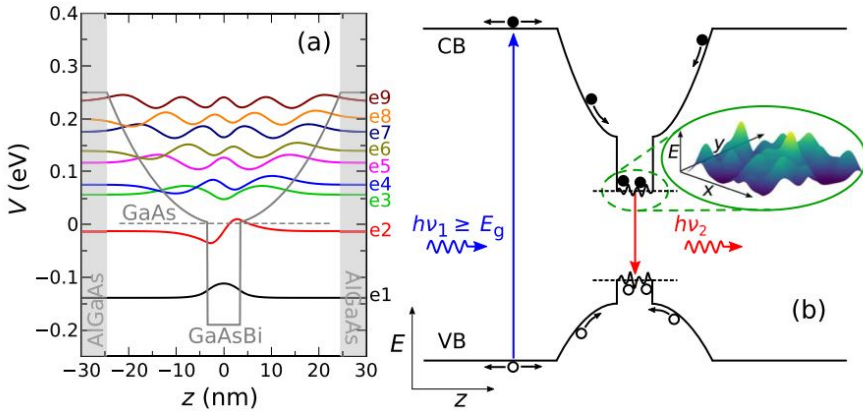


Figure 5.14 .(a) Energy subbands of coupled 7 nm width rectangular GaAsBi SQW with 6.5% of Bi and AlGaAs PQW with graded Al content from 30% in the claddings down to GaAs at 0 eV employed as PGBs. (b) Simplified model representation of the processes responsible for enhanced photoluminescence of GaAsBi SQW with PGBs: the carrier trapping enhancement and random fluctuating localization field for carriers in the well [117].

ing of PL band higher energy side with increasing power density at room temperature (not shown). It is worth noting, that QW width was 5 nm with 4.8% of Bi for this particular sample in contrast to other samples with 7 nm width QWs. The results are in a good agreement with other works [121]. The observed blue-shift of PL peak position with increasing power density at 3 K for all the samples (not shown) indicate the filling of density-of-state tails that are expanded in localizing randomly disordered potential field for carriers in GaAsBi QWs with PGBs.

5.4 Modeling of the main characteristics

To explain observed increase in PL (see Figure 5.11) for GaAsBi SQW with PGBs if compare to non-graded GaAsBi MQW and SQW designs one needs to determine the arrangement of quantum subbands for the rectangular QW coupled with parabolic, as PGBs contain its own structure of quantum energy subbands. Indeed, parabolic quantum wells (PQWs) were investigated extensively for exploitation of equidistant subband transitions taking advantage of unique properties of PQWs [103]. From the technological point of view the PQWs can be realized

by gradually changing the Al content by the quadratic law in defined layer or by inserting AlGaAs barrier layers with constant Al content yet of different thicknesses following the parabolic law in the GaAs, i.e. analog or digital alloy grading techniques, respectively. In contrast to other studies, the analog alloy grading technique was implemented in this work.

The electron energy subbands and the wavefunctions in the QW formed by the band edge potential variation $V(z)$ in AlGaAs structure with optional central GaAsBi SQW was modeled. The time-independent Schrödinger equation solving algorithm was applied [122]. The solver combines the preliminary estimations by the shooting method [123] with accurate and fast-converging coupled solution method for energies and wavefunctions (EWC method) based on Newton convergence scheme and internal bordered tri-diagonal matrix solver. In the present study, the 0.25 eV height barriers formed by Al content of 30% were used. The electron relative effective mass m^* increase with Al content in the alloy from pure , GaAs , 0.0592 m_0 to the barrier 0.0918 m_0 was calculated using linear approximation with 0.15 m_0 for AlAs.

In the case of GaAsBi QW, the band-gap shrinking was accounted by the coefficient 65 meV per 1% of Bi with 45% of narrowing associated with the conduction band. For GaAsBi, according to the reported constancy of electron mobility at low Bi concentrations [9], also the constancy of electron effective mass may be assumed. Following work on GaAs/GaAsBi laser structures [86], the reasonable estimation 0.0592 is used for electron effective mass at 6.5% Bi content. Selected parameter values for GaAsBi relay on our previous work with laser structures with different Bi content between 4.4% and 7.1% [86]. The potential energy in the AlGaAs graded barriers including the rectangular GaAsBi SQW at the center is specified as

$$V(z) = V_0 \left(\frac{2z}{l_{PQW}} \right)^2 + 0.13V_0 \left(\frac{2z}{l_{PQW}} \right)^4 \quad |z| > l_{QW}/2, \quad (5.4)$$

$$V(z) = 0.45V_1x_{Bi} \quad |z| < l_{QW}/2, \quad (5.5)$$

With limitation $V \leq V_0$ and parameters $V_0 = 0.25$ eV, $l_{PQW} = 52$ nm, where l_{PQW} is the PQW width, z is the coordinate accounted from the GaAsBi QW center, l_{QW} is the width of central rectangular GaAsBi QW layer, $V_1 = 6.5$ eV, and x_{Bi} is the Bi content in the SQW. For compensation of the carrier effective mass increase with increasing Al content, the quartic $\sim z^4$ term of relative size of 13% was added to the main parabolic potential term in order to maintain the constancy of energy steps [124].

Simulation results of 7 nm width and 6.5% Bi content in GaAsBi SQW with 52 nm width AlGaAs PGBs from 30% Al in the barriers to GaAs are shown in Figure 5.14. Nine energy subbands are found in the system and 2 lowest, namely e_1 and e_2 , are confined in GaAsBi SQW with the separation energy of 132.3 meV. Due to influence of the central rectangular GaAsBi QW potential to the parabolic one the energy subbands are not equidistant anymore. The subbands of PQW are rearranged closer to each other in pairs, namely e_3 and e_4 , e_5 and e_6 , and e_7 and e_8 . For the band-to-band transition determined photoluminescent properties the most important are the lowest subbands that are found in GaAsBi QW. Only conduction band potential is shown as for valence band the subband arrangement is much less resolved with 18 and 7 subbands for heavy and light holes, respectively, with few uppermost confined in 232 meV GaAsBi QW potential.

The room temperature PL intensity increase in the GaAsBi SQW with PGBs can be explained by more efficient photoexcited carrier trapping from the barriers into QW and the carrier localization of non-equilibrium carriers caused by Bi content fluctuation in GaAsBi and QW width deviation. Both processes are co-existing and contribute to the optical properties enhancement of PGB design. The simplified model is illustrated in Figure 5.14(b). The non-equilibrium carriers, whether photoexcited, as it is in this work, or can be injected electrically, reach the 50 nm width active area which consists of GaAsBi SQW and AlGaAs PGBs together. The carriers that reach the PGB layers can not escape the active area. As it is seen from the calculations, the electronic subband structure of PQW employed as graded barriers provides the favorable conditions for electrons to transit down to the lowermost energy subbands and recombine from the GaAsBi QW rather than from cladding or barrier layers. In the study by Gobel

et al., the trapping efficiency is shown to be $\sim 15\%$ higher for SQW with parabolically graded-index confinement than for the same QW without separate confinement or with nongraded confinement [125]. It was suggested that the enhancement of trapping efficiency in QW with graded barriers appears due to initial spatial distribution of the photocreated carriers. Also, built-in field in graded barriers prevent photoexcited carriers recombination from cladding and barrier layers. Finally, the electron–photon scattering is different for graded and non-graded structures.

The mobility of carriers that transit down to the energy subbands confined by GaAsBi QW is limited. It is due to the the randomly fluctuated potential field in the plane of QW shown in the Figure 5.14(b). The randomly distributed potential field fluctuations are caused by inhomogeneous Bi content distribution and well width variation. Indeed, for both conditions to facilitate the carrier localization the blurred well-barrier interface due the parabolic Al decrease towards the center of the active area is favorable if compare to abrupt interfaces in the case of non-graded barriers. The estimated scale σ of randomly distributed potential field fluctuations from the temperature dependent PL spectra shows considerable distortion between 36 and 44 meV. If compare to thermal energy 26 meV of carriers at room temperature the localization effect is still of great importance.

The probability for localized carriers to be captured by the non-radiative recombination centers is reduced and radiative recombination is significantly enhanced. The carrier localization effect have been reported in ternary alloys and QW structures based on dilute nitrides, such as GaNAs, GaInNAs, InGaN, and AlGaN [119, 126, 127] as well as other material systems, MgZnO for example [128]. In all cases, the enhancement in PL was observed. For MBE grown diluted GaAsBi structures the localization effect was reported as well. The work by Kudrawiec *et al.* presented the experimental evidences obtained by photomodulated transmittance and PL techniques of strong carrier localization phenomena in thick GaAsBi layers with 3% of Bi [121]. In the work by Mohmad *et al.* [71], the localization effect for rectangular GaAsBi/GaAs QWs was studied and the randomly distributed potential field fluctuation scale $\sigma = 14$ meV was estimated from the PL

peak position dependence on temperature. Another work by Kopaczek *et al.* also reported the carrier localization effect in GaAsBi QWs and the fitting of data provided slightly higher σ values for GaAsBi QWs if compare to GaAs [129], as is also the case in this work. Hence, one can note that the value of the random potential obtained in our work is much higher due to large Bi content in the designs and QWs width variation.

5.5 Conclusions for the chapter

In conclusion, it has been revealed that PL characteristics of GaAsBi QWs are significantly influenced by the optimal growth parameters. Structures grown under optimal parameters, such as the As/Ga BEPR close to unity, the relatively low Bi flux, and low QW growth temperature of 415 – 425 °C, exhibit the enhanced PL intensity. The technology, pulsed analog alloy grading technique, has been developed to grow highly precise 52-nm-width GaAsBi/AlGaAs parabolic quantum wells using molecular beam epitaxy. For the first time, the parabolically graded GaAsBi QW structures were grown with 2.6 – 6.8% Bi amount in the QWs, and the highest PL intensity was achieved for QWs with AlGaAs PGBs containing 30 % of Al in the barriers. The significant PL increase at room temperature is obtained due to the increased carrier trapping efficiency in the PGBs and due to the carrier localization effect in the GaAsBi QWs, where the inhomogeneous distribution of Bi amount leads to a random potential with energy fluctuations over the range of 36 – 44 meV. The PGBs create favorable conditions for carriers to be trapped and transit to the lowermost subbands, confined in GaAsBi QWs, while the blurred well-barrier interface enhances the carrier localization effect. The self-organized nature of carrier localization in the GaAsBi QWs serves for the stability of the photon emission. The enhanced band-to-band radiative recombination rate provides an opportunity for the fabrication of lasers based on GaAsBi quantum structures emitting wavelengths longer than 1.2 μm .

6. GaAsBi/GaAs BASED NEAR-INFRARED EMITTING QUANTUM DEVICES

Laser diodes are widely used in communication, scientific research, medicine, and other fields. They serve as light emitters for solid-state laser pumping and light sources in fiber optics as well as in wireless optical communication systems. In the region, there are organic and harmful molecule footprints, which increase the need for selective sensing systems applicable to environmental pollution monitoring. Despite of widespread usage of IR quantum devices further improvements of laser diodes are necessary in order to develop better stability and the longer functionality of laser emitters within the expanding applications. The peculiarities of fabrication of the NIR laser diodes made of AlGaAs, GaAs, and GaAsBi active region materials by implementing different active area designs such as quantum wells with standard rectangular and parabolic profiles are discussed within this chapter. There the electrical and optical characteristics of fabricated NIR laser diodes are also analysed.

6.1 Growth and fabrication of laser diode structures

6.1.1 Growth of laser diode structures

The enhanced optical efficiency of the GaAsBi PQW has been demonstrated in the previous chapter. Based on this technology a set of different laser diodes was fabricated. This includes the laser diodes with rectangular multiple AlGaAs and GaAs quantum wells as the active region of LDs and those with AlGaAs and GaAsBi parabolic

single quantum wells. The objective was to compare the impact of the shape of the active area on LD parameters. The characteristics of the parabolic GaAsBi structures have been then compared with those determined for the RQW GaAsBi laser diode structures, previously grown by Butkutė *et al.* (2014) [13].

The examined LD structures, sketched in Figure 6.1 (a), were grown using the n-type GaAs(001) substrates employing a *Veeco GENxplor R&D* molecular beam epitaxy system. The standard growth conditions of $T_{growth} = 665$ °C and arsenic overpressure (the As valve fully opened) were applied. Prior to growth, the native oxide was outgassed from the substrate by heating it to the temperature of 700 °C for 30 minutes under maximum arsenic flux. After removing the oxide, a silicon-doped (with the concentration of $2 \times 10^{18} \text{ cm}^{-3}$) GaAs buffer layer with a thickness of 50 – 100 nm was deposited to form a flat surface for epitaxial growth. The growth rate of the GaAs:Si buffer was 530 nm/h, and the temperatures were set to $T_{Ga} = 881$ °C and $T_{Si} = 1172$ °C, respectively. The thickness of the buffer layer was determined by monitoring the changes in RHEED surface reconstructions (2×4) of GaAs.

The 1.5 μm thick n-type and p-type AlGaAs cladding layers, doped with silicon ($2 \times 10^{17} \text{ cm}^{-3}$) and beryllium ($2 \times 10^{17} \text{ cm}^{-3}$), respectively, were initially formed. The growth rate for the cladding layers was kept at 1180 nm/h, and the Al content within the cladding layers was approximately 55% (calculated from RHEED oscillation). The source temperatures were set to such values: $T_{Ga_2} = 881$ °C, $T_{Al} = 1100$ °C, $T_{As} = 340$ °C, $T_{Si} = 1115$ °C, and $T_{Be} = 876$ °C, respectively. The following source fluxes of $P_{Ga_2} = 1.54 \times 10^{-7}$ Torr and $P_{Al} = 3.28 \times 10^{-7}$ Torr were kept. An undoped 200 nm AlGaAs waveguide with 30% Al composition was deposited after the formation of the AlGaAs cladding layer. The waveguide growth rate calculated at parameters of $T_{Al} = 1029$ °C and $P_{Al} = 8.07 \times 10^{-8}$ Torr, comprised value of 440 nm/h.

The active area contained either single or multiple QWs. These QWs were inserted between AlGaAs either parabolically graded or standard rectangular barriers, as shown in Figures 6.1 (b, c, d). To have the emission wavelengths in the range of 780 – 1100 nm, both the width and composition of the QWs were varied. The widths of AlGaAs and GaAs

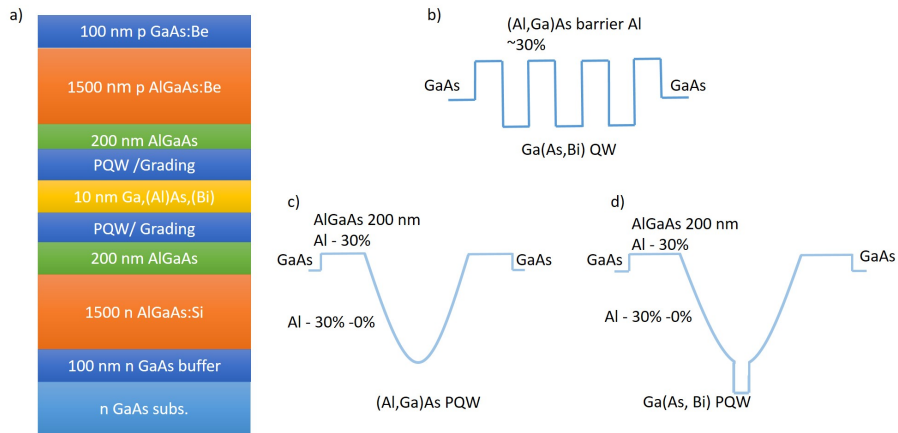


Figure 6.1 The schematic picture shows the laser diode structure (a) and various designs of the active area containing rectangular multi (b) and parabolic (c, d) single quantum wells of AlGaAs, GaAs and GaAsBi .

QWs were modified in the parameter range from 1.5 nm to 5 nm, while the thickness of the GaAsBi QWs reached the value of 10 nm. The LDs made by forming the AlGaAs and GaAs QWs were grown using the standard growth parameters of 650 °C temperature and arsenic overpressure. To incorporate the enhanced amounts of Bi into the GaAsBi QWs by retaining the high performance of the laser diodes, the two-temperature growth regime has been chosen. The specifics of the latter regime is comprised of the reduction of temperature. The temperature decrease down to 425 °C, during the growth of GaAsBi quantum wells, allowed for the control of Bi incorporation. Thereby, the growth of the waveguide layers using the standard high-temperature regime ensured high crystalline quality. The latter procedure would be a reason for the reduction of the alloy disorder and for the flattening of the bismuth distribution profile within a QW. The steps of QW growth in the formation of LD active region and optimization of these procedures have been described in Chapter 5. The 5 nm thick heavily p-doped ($3 \times 10^{18} \text{ cm}^{-3}$) GaAs layer was deposited on top of the AlGaAs:Be to form an electrode. The main parameters of the QW formation and growth of the structures examined in this study are summarized within Table 6.1.

Table 6.1 The main parameters of the investigated laser diodes characterize the quantum well (QW) material and the composition of the quantum wells. The QW shape indicates the profile of the quantum well, while the active region is determined by the number of quantum wells (N_{QW}) with a thickness of a single quantum well (d_{QW}) measured in nm. Additionally, I_{th} represents the threshold current measured in mA, and λ represents the lasing wavelength measured in nm at different lasing temperature.

	QW material	Type of QW	N_{QW}	d_{QW} , nm	I_{th} , mA	λ , nm (T, °C)
VGA0340	AlGaAs	Parabolic	1	1.5	71.5	817 (RT)
VGA0370	AlGaAs	Rectangular	2	5	98	829 (RT)
VGA0443	AlGaAs	Rectangular	2	1.5	51	781 (20 °C)
VGA0444	AlGaAs	Rectangular	2	2	66	787 (17 °C)
VGA0445	GaAs	Rectangular	2	2	43	800 (18 °C)
VGA0446	GaAs	Rectangular	2	1.5	54	783 (20 °C)
VGA0454	GaAsBi	Parabolic	1	10	80	1024-1031 (23 °C)
Butkute <i>et al</i> [13]	GaAsBi	Rectangular	3	8	120	1060 (23 °C)

6.1.2 Fabrication of laser diodes

The lasers fabricated in this study are metal-clad ridge waveguide (MCRW) lasers, also known as edge-emitting laser diodes. They consist of an n-GaAs substrate with active region and cladding layers, grown on the structure top. In the literature, two possible structures for the edge-emitting lasers are considered by attributing them to the gain-guided and index-guided (alternatively, quasi-index-guided) lasers. The gain-guided lasers contain the insulating regions at the top. These regions prevent current from flowing to the diode periphery. Thereby, the current can only flow through a narrow stripe in the middle of the laser

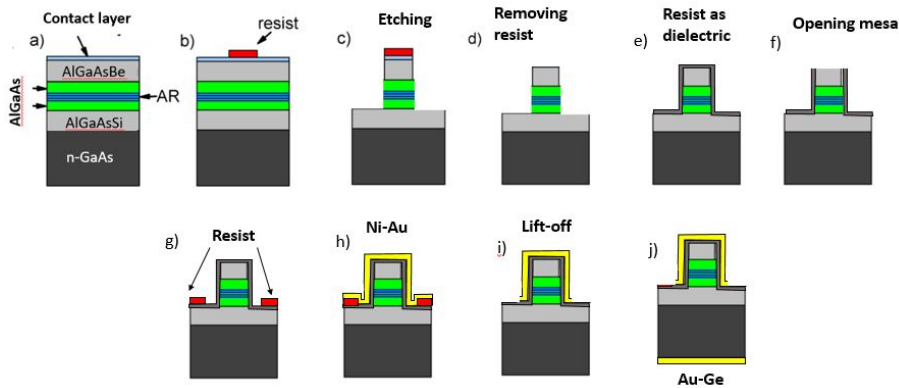


Figure 6.2 Schematic representation of the laser diode fabrication process, starting from the MBE growth of laser diode structure on the n-GaAs substrate, followed by various lithography and metallization steps, until the deposition of the final contact layer.

chip in between the two mirrors. In index-guided lasers, refractive index profiling is used to restrict the wave spreading outside the active volume of the LD. The waves propagating within a resonator of the index-guided laser are kept within active volume due to the refractive index differences of the active region and surrounding cladding layers, owing to an effect of complete internal reflection of radiation. Although gain-guided lasers are easier to fabricate, index-guided or quasi-index-guided lasers are preferential. The latter index-guided lasers exhibit better laser beam forming at the reduced threshold currents, resulting in lower radiation loss [130]. The LD devices fabricated in this study represented the index-guided laser type.

The first step of the LD formation involves an immersing of the material ingot into a solution of $H_2O:NH_4OH=10:1$ for approximately 30 seconds to remove organic contamination and native oxides. Next, the sample is rinsed using deionized water and dried at $120^\circ C$ on a hot-plate for 10 minutes. Then, the so-called Ti Prime, being an adhesion promoter, is deposited on the formed structure by using spin-coating means at 6000 RPM for 30 seconds. The sample is then baked on a hot-plate at $120^\circ C$ for two minutes to improve the adhesion of the resist to the GaAs surface, as sketched in Figure 6.2 (a).

The first photo-lithography step is performed in order to form the

mesa structures after the adhesion of the contact layer is finished. There, the AZ1518 resist is used for the implementation of this step. The spin-coating of the resist is carried out at 4000 RPM for 30 seconds. Finally, the resist is baked on a hotplate at 100 °C for one minute. The picture of the designed structure is obtained by using a mask. The resist is exposed to 75 mW/cm² UV light for 7 seconds through the mask. The picture-developing process is visually monitored for approximately 60 seconds and carried out using an H₂O:AZ351B=4:1 solution, as sketched in Figure 6.2 (b). The lithographically defined mesas are then etched layer-by-layer in order to remove the structure layers by reaching the AlGaAs:Si cladding layer, as sketched in Figure 6.2 (c). The obtained picture on the resist is employed as the etching mask. The etching of the top layers is carried out using either a citric acid solution of C₆H₈O₇:H₂O=1:10 for 8 minutes or H₂O:H₂O₂:H₃PO₄=10:1:1 for 3 minutes. After etching, any of the remaining resist on the sample is rinsed off using acetone, the isopropyl alcohol, and deionized water. The latter technological procedures are sketched in Figure 6.2 (d). The water is removed by drying the sample on a hotplate at 120 °C for 10 minutes. The surface is then coated with another resist layer, being a dielectric layer on the structure top, using the Ti35E for spin-coating at 4000 RPM performed for 30 seconds. Finally, the latter resist layer is baked on a hot plate at 95 °C for 2 minutes. The so processed sample is kept in a room ambient for rehydration before the second lithography step. The second lithography step is performed using 170 mW/cm² UV light exposure. The picture developing process is guided by the eye for approximately 130 seconds. This developing process is implemented using an H₂O:AZ351B=4:1 solution, as sketched in Figure 6.2 (f). To make the electrical insulation of the formed mesas, another photolithography step is required. This procedure is performed using a different mask. First, the AZ5214 resist is spin-coated onto the substrate at 4000 RPM for 30 seconds and baked on a hotplate at 110 °C for 50 s (see Figure 6.2(g)). The sample for rehydration is kept at room ambient for 5 min. The processing is accomplished by exposing the sample to 70 mW/cm² UV light through a mask intended for insulating layer formation. Also, the processed structure is later degassed for 10 min. After that, the post-exposure baking at 120 °C for 2 minutes is performed using the power density

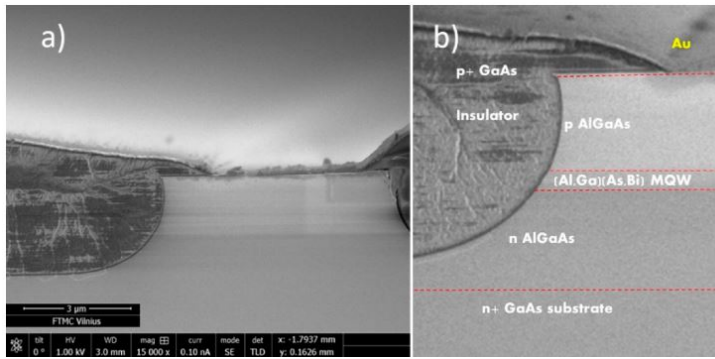


Figure 6.3 A SEM picture shows the view of the as-cleaved $5 \mu\text{m}$ width LD bar after UV lithography and metallization (a), along with a zoom-in image (b) with the red dashed lines as a visual guide indicating the details of the textured structure as a visual guide.

of exposure at 210 mW/cm^2 . The processed structure is then rinsed in $\text{H}_2\text{O}:\text{AZ351B}=4:1$ for 25 seconds after lithography procedures. Then, a Ni-Au contact is evaporated onto the top of the processed mesa structure. Prior to evaporation, the sample is cleaned using oxygen plasma in order to remove any remaining resist residues. The evaporation is carried out using a VST TFDS-870 electron-beam evaporation system (see Figure 6.2(h)). After lift-off in acetone, the sample is rinsed in isopropyl alcohol and deionized water (see Figure 6.2(i)). On the bottom of the structure, an Au-Ge metallic layer is deposited to form the n-type ohmic contact (see Figure 6.2(j)). As the later step, the edge emitter bars are cleaved with different lengths ($361 - 821 \mu\text{m}$) and mounted on a holder for further measurements. The facets are crucial for the coupling of light out of the device. Therefore, it is crucial to cleave the facets in order to have a clean and smooth surface. Figure 6.3 illustrates a SEM image of the LD bar after UV lithography and metallization technological steps, along with a zoom-in image with the red dashed lines as an eye-guides, to indicate the details of the textured structure.

6.2 Characterization of the fabricated laser diode structures

The main characteristic of laser diodes is the power-current curve. The electrical measurements of these characteristics were performed at room temperature using a Keithley 4200-SCS Parameter Analyzer (Keithley Instruments, Inc.) and a Summit Probe Station 11000B-AP (Cascade Microtech, Inc.).

Both rectangular and parabolic quantum well type LDs obey the typical p-n junction diode behavior, represented in their I-V and L-I characteristics. The slight slope observed at the beginning of the L-I curve, shown in Figure 6.5 corresponds to the increase in the spontaneous emission rate. As the threshold is reached, the emission intensity rapidly increases, and the lasing of the LD device begins. The rollover at the end of the curve is caused by the internal heating. The current density increases as the heating outcome. This leads to increased emission intensity loss. This phenomenon appears only during the CW lasing operation, as the LD junction is unable to heat up sufficiently during pulsed operation. The L-I curve indicates that there exists a range of current values where the threshold current can be extrapolated with a linear approach when fitting the lasing ascribed current part within the L-I characteristic.

To compare the performances of the LD devices fabricated using mesa structures of different geometric parameters, the threshold current densities should be evaluated. To make this, the current values should be normalized to the resonator length and width of the device:

$$J_{th} = \frac{I_{th}}{LW}. \quad (6.1)$$

Here L and W are the laser diode length and width, respectively, I_{th} denotes the threshold current. The threshold current of the fabricated lasers varied from 43 mA to 98 mA, with calculated current density J_{th} values ranging from 2.48 to 3.5 kA/cm². The main parameters of the fabricated LDs are listed in Table 6.2.

Table 6.2 The main parameters of the investigated laser diodes are the length and width of the diode (nm) structure, I_{th} being the threshold current, and the J_{th} representing the threshold current density of a laser diode.

	length, μm	width, μm	I_{th} , mA	J_{th} , kA/cm ²
VGA0340	821	3.5	71.5	2.49
VGA0370	800	3.5	98	3.50
VGA0443	588	3.5	51	2.48
VGA0444	638	3.5	66	2.96
VGA0445	361	3.5	43	3.40
VGA0446	578	3.5	54	2.67
VGA0454	600	3.5	80	3.8
Butkutė <i>et al.</i> [13]	-	-	120	30

In order to compare the LD performances, the laser diodes have been distributed into groups dependent on the shape and composition of QWs and on QW width, as well. Figure 6.4 illustrates the EL spectra recorded on LDs of the first group. The LDs VGA0443, VGA0444, VGA0445, and VGA0446 of this group were fabricated using QWs of different thicknesses. The GaAs QW structures exhibited lasing at 800 nm (VGA0445) and 783 nm (VGA0446) wavelengths, for QW widths of 2 nm and 1.5 nm and lasing temperature 18 °C and 20 °C, respectively. The PL intensity of the 2 nm width QW (VGA0445) is twice larger than that obtained for the 1.5 nm QW (VGA0446) structure. As for the AlGaAs QW structures, the lasing occurs at 781 nm (VGA0443) and 787 nm (VGA0444) light wavelengths for the QW widths of 1.5 nm and 2 nm and temperature of 20 °C and 17 °C, respectively.

The power-current measurements for the laser diode sample group presented in Fig.6.5 were investigated. The obtained threshold current values I_{th} extracted from the L-I characteristics, measured at room temperature on the VGA0443, VGA0444, VGA0445, and VGA0446 LDs, appeared to be 51 mA, 66 mA, 43 mA, and 54 mA, respectively, see Fig.6.5. The corresponding emitted light output powers were 5 mW, 2 mW, 4.5 mW, and 350 mW, respectively. These obtained values of LD parameters are close to those inherent for the laser devices commercially available. This result demonstrates that the laser diodes

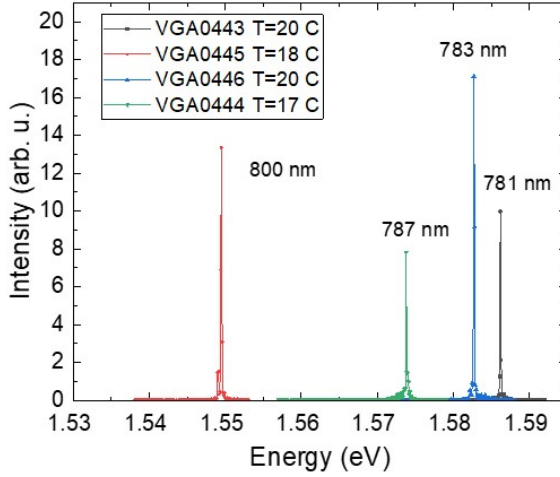


Figure 6.4 EL spectra of the laser diodes containing rectangular GaAs/AlGaAs QWs with 2 and 1.5 nm QW width.

fabricated in this study have the potential for practical applications.

In LDs of the second group, two LD mesa structures of different QW shape, namely, the VGA443 LD being the rectangular and VGA340 one, containing the parabolic QWs (sketched within insets of Figure 6.6) have been compared. These structures were made of the same material, namely AlGaAs, containing QWs of 1.5 nm width. The lasing spectra for the VGA0443 LD were recorded at different temperatures. The LD with rectangular QWs emitted wavelengths covering a spectrum range from 778 nm to 781 nm. For the LDs with parabolic QW structure, the emitted wavelengths ranged from 810 nm to 816 nm. The threshold current I_{th} values of 52 mA and 71.5 mA have been estimated for the rectangular and parabolic QW shaped LDs, respectively. The difference in the emitted wavelengths can be attributed to the different Al content within QWs, where the VGA0443 rectangular QW structure contained 15% of Al, while LD with parabolic QW structure had 6% of Al. To make a more precise comparison, it is necessary to calculate the threshold current density J_{th} to eliminate the impact of the geometric parameters of each LD device. Value of $J_{th} = 2.48 \text{ kA/cm}^2$ has been obtained for the LD VGA0443 with the rectangular QW. While for the LD with parabolic

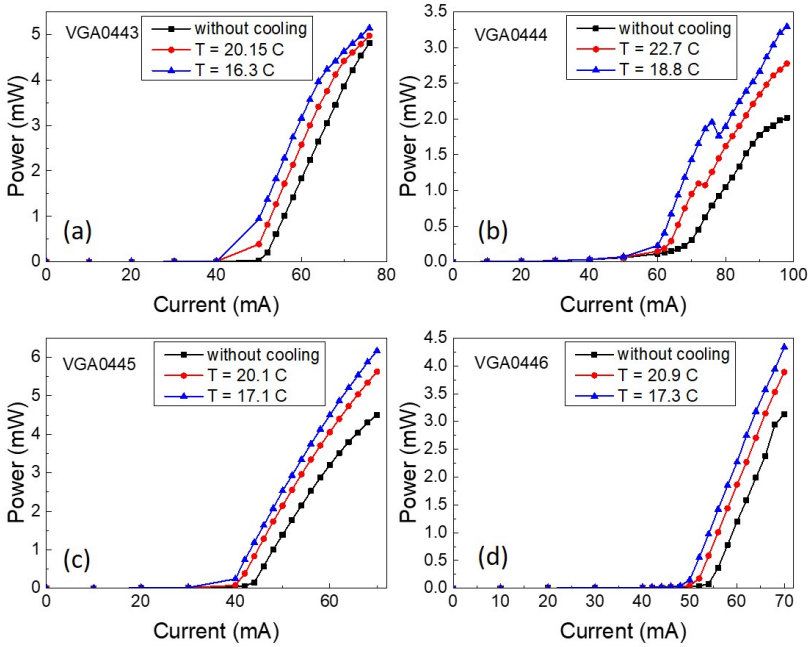


Figure 6.5 Laser diode output characteristics for VGA0443 (a), VGA0444 (b), VGA0445 (c) VGA0446 (d).

QW structure the $J_{th} = 2.49 \text{ kA/cm}^2$ has been evaluated. However, for comparison of the LD parameters dependent on the QW shape the important factor is the number of QWs which was ignored in the latter estimations. The parabolic structure had a single QW (SQW), while the rectangular structure contained the two-QWs structure in the active region. Therefore, the LDs with parabolic QW structure are the more promising devices for applications, as they exhibit the lower threshold current density. The lower threshold current density implies less current required to achieve lasing.

For comparison of the LDs made of GaAsBi and LDs with parabolic QWs made of AlGaAs material, the lasing spectra of AlGaAs recorded at different temperatures have been examined. The latter spectra are illustrated in Figure 6.7. The obtained lasing wavelength spectra ranged from 810 nm to 816 nm. For the SQW of GaAsBi with a 10 nm QW width, the broad spectra, ranging from 1024 nm to 1031 nm, were obtained at room temperature. Values of the I_{th} in the range of 80 mA and J_{th} of 3.8 kA/cm^2 have been estimated for the LDs made of GaAsBi PQW.

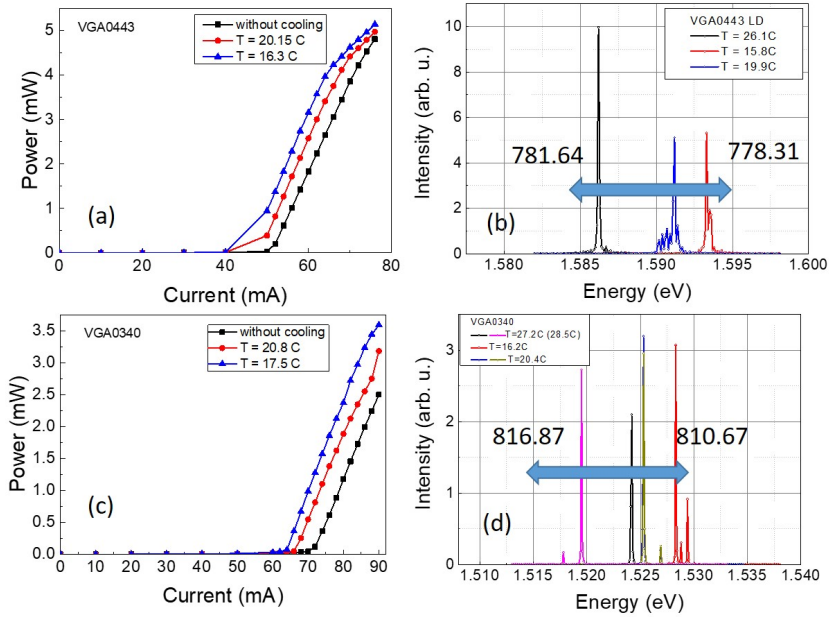


Figure 6.6 The output characteristics of the VGA0443 and VGA0340 LDs are shown in (a) and (c), respectively, while their lasing spectra are shown in figures (b) and (d), respectively.

It has been deduced from characteristics of LDs made of GaAsBi PQW that J_{th} is higher when compared with characteristics of the same structure made of AlGaAs. However, LD structures made by Butkutė *et al.* using the GaAsBi rectangular structure exhibited the higher I_{th} and J_{th} values than those obtained in this study. The appeared difference can be explained by the existence of the grading layers having steps of small activation energy. These activation energies determine the Fermi level positioning near the band edge for each grading step and thus leading to enhanced conductivity and reduced resistance of the material. Such a structure operates like the electron-blocking layer. Therefore, the parabolic QW structures appear to be more promising for applications.

6.3 Conclusions for the chapter

The laser diodes with different material active regions and the design of QWs have been fabricated and characterized in this study. Laser diodes made of AlGaAs with both PQW and RQW structures exhibited

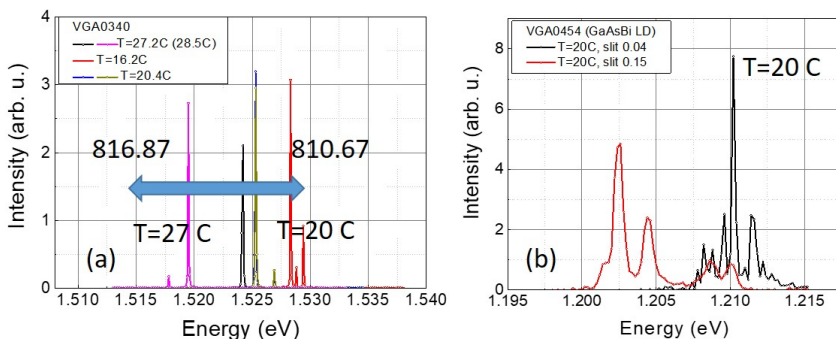


Figure 6.7 The lasing spectra were recorded on AlGaAs VGA0340 (a) and GaAsBi VGA0454 (b) LDs.

the typical I-V and L-I characteristics with emitted wavelengths ranging over the 780 – 829 nm spectrum. The laser diodes with parabolic QWs made of GaAsBi exhibited a broader lasing spectrum ranging from 1024 to 1031 nm wavelengths. The threshold currents of laser diodes made of AlGaAs RQW varied from 43 mA to 98 mA, while this current was close to 71 mA for AlGaAs PQW. Calculated threshold current densities (J_{th}) for AlGaAs RQW varied from 2.48 kA/cm² to 3.50 kA/cm² and for AlGaAs PQW – 2.49 kA/cm². The GaAsBi PQW laser diodes exhibited a threshold current of 80 mA and calculated $J_{th} = 3.8$ kA/cm². These results demonstrate the big potential for various applications of the laser diodes, fabricated varying the composition and QW shape within the active region. However, it appeared that further optimizations of LD performance are inevitable.

7. CONCLUSIONS OF THE STUDY

The latter conclusions provide a summary of the key findings and significant contributions to the science field considered in the dissertation.

1. The optimal MBE conditions for growing 100 nm thick GaAsBi layers with Bi content ranging from 0.6% to 11.2% on ultra-thin (up to 20 nm) buffers are as follows: temperature range of 320 – 425 °C, As/Ga BEPR from 0.95 to 1.18, and Bi equivalent pressure between 1.0×10^{-7} Torr and 1.8×10^{-7} Torr.
2. The 100 nm thick GaAsBi layers with 0.6 – 11.2% Bi are almost fully strained. The layer relaxation does not depend on Bi concentration and varies in range of 0.6 – 3.3%.
3. The experimentally evaluated sensitivity of the energy band-gap to temperature is in the order of 0.21 meV/K^{-1} , which is two times smaller in magnitude than that of GaAs.
4. GaAsBi QWs with Bi concentrations ranging from 2.6% to 6.8% were grown using AlGaAs parabolic graded barriers containing 30% Al on the top of the barrier and pure GaAs on the bottom.
5. The parabolic graded barriers and the carrier localization effect, which are responsible for the carriers trapping efficiency in the GaAsBi QWs due to the inhomogeneous distribution of Bi, have led to a significant room temperature emission enhancement. The established activation energies of 36 meV to 44 meV are attributed to the random potential disorder influenced by the inhomogeneities of Bi in the QW and the thickness of the QW.

6. Both type RQW and PQW AlGaAs and GaAs-based laser diodes demonstrated lasing at wavelengths ranging from 782 nm to 829 nm. The threshold current values were found to be approximately 70 mA for AlGaAs PQW-based LDs, 50 mA to 100 mA for AlGaAs RQW-based LDs, and 40 mA to 50 mA for GaAs RQW-based LDs. Calculated threshold current densities (J_{th}) were found 2.49 kA/cm², 2.48 – 3.50 kA/cm², 2.96 – 3.40 kA/cm², respectively.
7. The laser diodes with GaAsBi QWS and PGB demonstrated room temperature lasing spectra ranging from 1024 nm to 1031 nm, depending on the quality of the laser bar mirrors. The threshold current value registered for GaAsBi PQWs was approximately 80 mA and calculated $J_{th} = 3.8$ kA/cm².

8. SANTRAUKA

Įvadas

Infraraudonųjų spindulių (IR) spektro sritis yra plačiai naudojama įvairiems taikymams dėl sugerties ir emisijos juostų, susijusių su įvairių organinių molekulių vibracinėmis savybėmis. Tačiau komerciniai detektoriai, integruoti į šias sistemas, nėra pakankamai jautrūs. Lazeriniams diodams (LD) ir šviestukams (LED) trukdo nuostoliai, atsirandantys dėl Ože nespindulinės rekombinacijos, ir bangos ilgis jautrus temperatūros pokyčiams. Nors nemažai publikacijų skirta prietaisų, veikiančių viduriniojoje infraraudonųjų spindulių srityje (kur molekulių sugertis yra ryškesnė), gamybai ir tyrimams, komerciniai prietaisai, tinkami integruoti į sistemas, neturi pakankamo jautrumo. Priešingai, prietaisai, veikiantys artimojoje infraraudonojoje srityje (NIR), pasižymi labiau pageidautinomis savybėmis, o jų jautrumas yra šimtą kartų didesnis. Be to, NIR spinduliuotė yra saugi žmogaus organizmui ir leidžia atlikti spektroskopinius tyrimus odos audinių, kraujo analizei, gliukozės, deguonies ir hemoglobino koncentracijai įvertinti. Išpildyti prietaisams keliamus reikalavimus labai svarbu, nes jie vis dažniau naudojami neinvazinėje prevencinėje medicinoje, cheminiams ir biologiniams jutikliams, kurie naudoja šviesą molekulėms stimuliuoti [1–3]. Mokslininkai nuolat ieško naujų metodų infraraudonųjų spindulių jutiklių savybėms pagerinti, siekdami geresnio parametrų stabilumo, ilgesnio veikimo laiko ir platesnių taikymo galimybių. Dėl šios priežasties IR spinduliuotės šaltinių ir detektorių kūrimas tebėra aktualus – būtina kurti naujas medžiagas, tinkamas šiems IR prietaisams gaminti.

Didelė pažanga pasiekta kuriant GaAsBi kvantinių struktūrų

auginimo technologiją, kuri gali būti naudojama įvairiose optoelektroninėse srityse, įskaitant lazerinius diodus [4,5], šviesos diodus [6], fotodetektorius [7], spintronikos prietaisus [8] ir saulės elementus [9]. Bismidai sulaukė didelio dėmesio dėl savo unikalių fizikinių savybių, pavyzdžiui, didelio draustinių juostų tarpo (E_g) sumažėjimo, sukinio-orbitinio suskilimo ir mažesnio temperatūrinio jautrumo, lyginant su tradiciniais III-V puslaidininkiniais junginiais [10–12]. Nustatyta, kad E_g vertė GaAsBi junginyje sumažėja iki 90 meV įterpiant vieną procentą bismuto [8,10,26,43]. Tikimasi, kad bismidų panaudojimas formuojant aktyviąją prietaisų terpę leis pagaminti efektyvius lazerinius diodus veikiančius IR srityje.

GaAs_{0,975}Bi_{0,025} lazerį, užaugintą MBE būdu pirmą kartą pademonstravo 2010 m. Tominaga *et al.* [4]. Pirmąjį sėkmingą GaAs_{0,978}Bi_{0,022} vienos kvantinės duobės (SQW) lazerinio diodo, užauginto naudojant metalo-organinio cheminio nusodinimo iš garų fazės (MOCVD) būdu, veikimą 2013 m. pademonstravo Ludewig *et al.* [5]. Tuo tarpu elektra kaupinamo GaAsBi daugybinių kvantinių duobių (MQW) lazerinio diodo, užauginto molekulinės pluoštelių epitaksijos (MBE) būdu su 6% Bi, lazeriavimą 2014 m. pristatė Butkutė *et al.* [13].

Iššūkiai paminėti anksčiau reikalauja kurti naujas medžiagas tokias kaip GaAsBi ir tirti optines bei morfologines savybes, siekiant pritaikyti prietaisuose. Šioje disertacijoje dėmesys skiriamas auginimo sąlygų optimizavimui naudojant MBE. Tyrimas apima 100 nm storio GaAsBi epitaksinių sluoksnių su itin plonu GaAs buferiniu sluoksniu, analizę. Šiame tyrime didžiulis dėmesys taip pat skiriamas medžiagų sudėties ir kvantinių struktūrų geometrijos poveikiui optinėms savybėms tirti. Sukurtos naujovės apima parabolinio analoginio lydinio gradientinio kitimo metodą (PAAG), kuris yra galinga priemonė kvantinėms struktūroms auginti ir sukurti pagrindą GaAsBi lazeriniams diodams, skirtiems artimajai infraraudonajai sričiai.

Pagrindinis tikslas

Šių tyrimų tikslas - sukurti III-V-Bi nanostruktūrų MBE augimo technologiją naudojant GaAs platformą. Tai apima epitaksinių sluoksnių sudedamųjų dalių ir kvantinių struktūrų analizę, siekiant suprasti

jų poveikį epitaksinių sluoksnių savybėms. Tyrimai taip pat skirti infraraudonosios srities lazerinių diodų kūrimui. Atliekami išsamūs bismidinių kvantinių nanostruktūrų ir epitaksinių sluoksnių tyrimai, siekiant atskleisti kritinius technologinius auginimo parametrus. Šiam tikslui pasiekti buvo atlikti šie uždaviniai:

1. 100 nm GaAsBi sluoksnių ant GaAs padėklų auginimo technologijos sukūrimas naudojant MBE metodą. Eksperimentinis 100 nm GaAsBi sluoksnių struktūrinių ir optinių savybių tyrimas.
2. GaAsBi kvantinių duobių (QW) augimo technologijos sukūrimas naudojant įvairius: vienos ir (arba) kelių stačiakampių (RQW), laiptuotų ir parabolinių (PQW) kvantinių duobių tipus. Analoginio lydinio gradientinio kitimo metodo pritaikymas PQW formavimui.
3. Lazerinių diodų auginimo technologijos naudojant AlGaAs ir GaAsBi kaip aktyviasias sritis, leidžiančios veikti atitinkamai 780 – 830 nm ir 1000 – 1100 nm spektro diapazone, sukūrimas.
4. GaAsBi ir AlGaAs lazerinių diodų gamyba ir charakterizavimas naudojant skirtingo tipo aktyviasias sritis.

Mokslinis naujumas ir svarba

Šioje disertacijoje pateikiami išsamūs GaAsBi sluoksnių ir kvantinių struktūrų auginimo MBE metodu ant GaAs padėklų tyrimai. Tyrime daugiausia dėmesio skiriama auginimo parametrų optimizavimui, siekiant kontroliuoti medžiagos struktūrinės ir optinės savybes. Tyrime sėkmingai nustatytos optimalios auginimo sąlygos, kuriomis galima suformuoti 100 nm storio GaAsBi epitaksinius sluoksnius su 10 % Bi koncentracija, kurie gali būti naudojami GaAsBi detektoriams gaminti.

Šiame darbe pirmą kartą pademonstruotas analoginio lydinio gradientinio kitimo metodo naudojimas auginant parabolines kvantines GaAsBi duobes. Parodyta, kad parabolinės GaAsBi kvantinės duobės pasižymi daugiau nei 50 kartų didesniu fotoluminescencijos intensyvumu, palyginti su stačiakampėmis daugybinėmis GaAsBi kvantinėmis duobėmis. Šiuo tyrimu taip pat nustatyti optimalūs

augimo parametrai paraboliniems QW formuoti tiek AlGaAs, tiek GaAsBi lazeriniuose dioduose. Pirmą kartą pademonstruotas lazerinis diodas su paraboline GaAsBi kvantine duobe aktyviojoje srityje.

Ginamieji teiginiai

Pagrindiniai ginamieji teiginiai:

1. 100 nm storio GaAsBi sluoksniuose, kuriuose yra 2 – 8 % Bi, auginant stechiometrinėmis sąlygomis ant itin plono GaAs buferio (iki 20 nm), relaksacija yra nežymi - apie 0,5 – 3 %
2. Analoginio lydinio gradientinio kitimo metodas yra perspektyvus auginant parabolinį GaAsBi kvantinės duobės potencialo profilį. AlGaAs barjerą galima pasiekti keičiant Al šaltinio temperatūrą ir išlaikant pastovią Ga šaltinio temperatūrą.
3. Parabolinių kvantinių duobių taikymas lazerinių diodų aktyviojoje srityje leidžia sumažinti kvantinių duobių skaičių aktyviojoje srityje, todėl sumažėja slenkstinis srovės tankis.

Autorės indėlis

Autorė atliko visas MBE augimo procedūras, įskaitant padėklo paruošimą, auginimo stebėseną ir struktūros formavimą. Autorė taip pat padėjo atlikti daugumą matavimų, analizavo duomenis ir interpretavo rezultatus. Autorė atliko eksperimentinių duomenų analizę ir pirminį mokslinių publikacijų rengimą. Autorė pristatė mokslinių tyrimų rezultatus konferencijose žodiniuose ir stendiniuose pranešimuose. Visi neautoriniai darbai yra tinkamai cituojami.

4 skyriaus matavimai ir rezultatai paskelbti straipsnyje **S. Pūkienė**, A. Jasinskas, A. Zelioli, S. Stanionytė, V. Bukauskas, B. Čechavičius, E. Dudutienė, R. Butkutė, Influence of an ultra-thin buffer layer on the growth and properties of pseudomorphic GaAsBi layers, Lithuanian Journal of Physics, **62**, 93 (2022).

5 skyriaus matavimai ir rezultatai paskelbti straipsniuose **S. Pūkienė**, M. Karaliūnas, A. Jasinskas, E. Dudutienė, B. Čechavičius, J. Devenson, R. Butkutė, A. Udal and G. Valušis Enhancement of photoluminescence of GaAsBi quantum wells by parabolic design of AlGaAs

barriers, *Nanotechnology*, **30**, 455001 (2019) and M. Karaliūnas, E. Dudutienė, A. Čerškus, J. Pagalys, **S. Pūkienė**, A. Udal R. Butkutė, G. Valušis, High precision parabolic quantum wells grown using pulsed analog alloy grading technique: Photoluminescence probing and fractional-dimensional space approach, *Journal of Luminescence*, **239**, 118321 (2021). Šio straipsnio rezultatus galima rasti E. Dudutienės disertacijoje. Svarbu pabrėžti, kad šio straipsnio autorės indėlis yra MBE procesai - analoginio lydinio gradientinio kitimo metodo naudojimas kvantinių duobių auginimui. E. Dudutienė disertacijoje atliko optinius matavimus ir analizavo fotoluminescencijos rezultatus.

6 skyriaus matavimai ir rezultatai paskelbti straipsnyje S. Armalytė, J. Glemža, V. Jonkus, S. Pralgauskaitė, J. Matukas, **S. Pūkienė**, A. Zelioli, E. Dudutienė, A. Naujokaitis, A. Bičiūnas and R. Butkutė Low-Frequency Noise Characteristics of (Al, Ga)As and Ga(As, Bi) Quantum Well Structures for NIR Laser Diodes, *Sensors*, **23**, 2282 (2023) and J. Glemža, S. Pralgauskaitė, J. Matukas, **S. Pūkienė**, A. Zelioli, A. Bičiūnas, B. Čechavičius, V. Nargelienė and R. Butkutė Low frequency noise study for developing of AlGaAs and GaAsBi QW structures for NIR LDs, *IEEE Xplore: 24th International Microwave and Radar Conference (MIKON)*, Gdansk, Poland, 2022, pp. 1-4.

Publikacijų sąrašas

Pagrindiniai šio tyrimo rezultatai buvo paskelbti 5 moksliniuose straipsniuose ir asmeniškai pristatyti nacionalinėse ir tarptautinėse konferencijose bei doktorantų mokyklose. Autorė asmeniškai pristatė 12 mokslinių pranešimų taip pat buvo daugiau kaip 30 kitų konferencijų pranešimų bendraautorė.

P1 **S. Pūkienė**, M. Karaliūnas, A. Jasinskas, E. Dudutienė, B. Čechavičius, J. Devenson, R. Butkutė, A. Udal, G. Valušis, Enhancement of photoluminescence of GaAsBi quantum wells by parabolic design of AlGaAs barriers, *Nanotechnology*, **30** 455001 (2019).

P2 M. Karaliūnas, E. Dudutienė, A. Čerškus, J. Pagalys, **S. Pūkienė**, A. Udal R. Butkutė, G. Valušis, High precision parabolic quantum wells grown using pulsed analog alloy grading technique:

- Photoluminescence probing and fractional-dimensional space approach, *Journal of Luminescence*, **239**, 118321 (2021).
- P3 **S. Pūkienė**, A. Jasinskas, A. Zelioli, S. Stanionytė, V. Bukauskas, B. Čechavičius, E. Dudutienė, R. Butkutė, Influence of an ultra-thin buffer layer on the growth and properties of pseudomorphic GaAsBi layers, *Lithuanian Journal of Physics*, **62**, 93 (2022).
- P4 J. Glemža, S. Pralgauskaitė, J. Matukas, **S. Pūkienė**, A. Zelioli, A. Bičiūnas, B. Čechavičius, V. Nargelienė and R. Butkutė Low frequency noise study for developing of AlGaAs and GaAsBi QW structures for NIR LDs , *IEEE Xplore: 24th International Microwave and Radar Conference (MIKON)*, Gdansk, Poland, 2022, pp. 1-4.
- P5 S. Armalytė, J. Glemža, V. Jonkus, S. Pralgauskaitė, J. Matukas, **S. Pūkienė**, A. Zelioli, E. Dudutienė, A. Naujokaitis, A. Bičiūnas and R. Butkutė Low-Frequency Noise Characteristics of (Al, Ga)As and Ga(As, Bi) Quantum Well Structures for NIR Laser Diodes, *Sensors*, **23**, 2282 (2023)

8.1 GaAsBi apžvalga

Galio arsenido bismidas (GaAsBi) yra intensyviai tyrinėjamas dėl savo unikalių savybių. Buvo pastebėta jog įterpus bismuto (Bi) į galio arsenido gardelę (GaAs) 42 MeV/% – 90 meV % sumažėja junginio draustinių energijų tarpas (E_g) [8, 10, 11, 26, 42, 43] ir jo dydis nedaug priklauso nuo temperatūros pokyčių [10–12]. Didinant įterpiamo Bi kiekį į GaAsBi didėja spin-orbitinio suskilimo energija (Δ_{SO}) ir įterpus daugiau nei 10% Bi – $\Delta_{SO} > E_g$ [47,48], galima pašalinti nespindulinės rekombinacijos centrus, kurie lemia nuostolius naudojamuose prietaisuose. Šios savybės svarbios, kuriant stabilius prietaisus, veikiančius IR spektrinėje srityje. Didelė pažanga padaryta kuriant GaAsBi kvantines struktūras, kurios gali būti naudojamos įvairiose optoelektronikos srityse, įskaitant lazerius [4,5], šviestukus (LED) [6], fotodetektorius [7], saulės elementus [9], spintronikos prietaisus [8].

8.2 Eksperimentinės metodikos

Šiame darbe tirtos GaAsBi struktūros buvo augintos MBE metodu naudojant SVT-C-V-2 (JAV) ir Veeco GENxplor R&D (JAV) prietaisus. Didelės energijos atspindėtų elektronų difrakcija (RHEED) buvo naudojama *in situ* stebėti sluoksnio struktūrą viso epitaksinio auginimo proceso metu. Tyrime daugiausia dėmesio skiriama auginimo parametrų optimizavimui stebint padėklo temperatūros, Bi pluoštelio intensyvumo ir As/Ga ekvivalentinio srautų santykio (BEPR) įtaką epitaksiniam sluoksniams ir struktūroms. Bandinių paviršiaus morfologija tirta *ex situ* Dimension 3100 SPM/Nanoscope IVa (Veeco, JAV) atominių jėgų mikroskopu (AFM). Naudojant didelės skyros rentgeno spindulių difrakcijos metodą (HR-XRD), buvo nustatomas į gardelę įterpto Bi kiekis bei išmatuotas atvirkštinės gardelės žemėlapis (RSM). Matavimai buvo atliekami naudojant SmartLab (Rigaku, Japonija) HR-XRD difraktometrą. STEM matavimai buvo atliekami peršvečiuojamuoju elektroniniu mikroskopu FEI Tecna G20. Bandinių optiniai parametrai buvo nustatomi atliekant fotoluminescencijos (PL) ir temperatūrinės fotoluminescencijos (TDPL) matavimus. PL matavimai buvo atliekami žadinant DPSS 532 nm bangos ilgio, 5 kW/cm²

galios lazeriniu diodu, o signalas registruojamas GaInAs fotodetektoriuje. Lazerinių diodų elektriniai matavimai atliekami elektrinių parametų analizatoriumi (Keithly 4200-SCS Parameter Analyzer), esančiu zondinėje stotelėje (Summit Probe Station 11000B-AP).

8.3 Pagrindiniai rezultatai ir apibendrinimas

8.3.1 100 nm GaAsBi epitaksinių sluoksnių auginimo sąlygos ir rezultatai

Serija 100 nm GaAsBi storų sluoksnių užauginta MBE metodu ant pusiau izoliuojančių GaAs(100) padėklų. GaAsBi sluoksniai buvo auginami naudojant dvi molekulinę pluoštelių epitaksijos sistemas: *Veeco GENxplor R&D* (bandiniai pažymėti kaip VGA serija) ir SVT-A (bandiniai pažymėti kaip B serija). Svarbiausi technologiniai parametrai yra padėklo temperatūra, Bi/As ekvivalentinis pluoštelių srautų santykis ir Bi srautas. Yra žinoma, kad bismutas linkęs segreguoti į paviršių [131]. Prieš auginimą padėklas buvo kaitinamas 700 °C temperatūroje, siekiant pašalinti paviršiaus oksidus. Plonas iki 20 nm GaAs buferinis sluoksnis augintas 600 – 680 °C išlaikant 300 – 500 nm/h augimo greitį. Buferio augimo greitis ir storis nustatytas pagal RHEED vaizdo pokyčius. Padėklo temperatūra buvo sumažinta iki GaAsBi augimo temperatūros intervale 320 – 425 °C. Keičiant As plyšio vožtuvo padėtį, sumažintas As/Ga srautų santykis kito 0,922 iki 1,091. Siekiant pagerinti Bi įterpimą, bandiniai 10 sekundžių buvo veikiami Bi srautu, todėl buferis iš dalies padengtas Bi drėkinamuoju sluoksniu, kuris veikė kaip paviršinio aktyvumo medžiaga. Augimo temperatūra buvo stebima naudojant termoporos rodmenis. Augimo proceso metu paviršiaus kokybė ir augimo režimas buvo stebimi *in situ*.

Bismuto kiekis 100 nm epitaksiniuose sluoksniuose įvertintas naudojant HR-XRD matavimus. Optinės savybės nustatytos naudojant PL. Bandinių paviršiaus morfologija tirta AFM *ex situ*. Pagrindiniai išmatuoti parametrai pateikti lentelėje 8.1.

Esant skirtingai epitaksinių sluoksnio auginimo temperatūrai, As/Ga BEPR ir bismuto srautui, užauginti 100 nm sluoksniai, kuriuose Bi kiekis svyruoja nuo 0,6% iki 11,2%. HR-XRD ω -2 θ difraktogramos

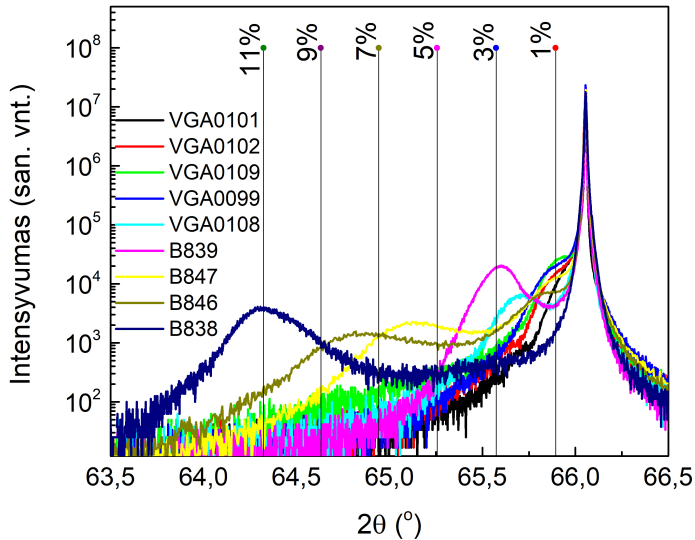
Lentelė 8.1 Pagrindiniai 100 nm GaAsBi sluoksnių išmatuoti parametrai: E_{PL} - GaAsBi PL smailės maksimumo vertės kambario temperatūroje. Bismuto kiekis įvertintas iš HR-XRD ω - 2θ matavimų. Relaksacija įvertinta iš RSM gardelės žemėlapių, o paviršiaus šiurkštumas (RMS) apskaičiuotas iš AFM matavimų.

	E_{PL} RT, eV	X_{Bi} , %	Relaksacija, %	RMS, nm
VGA0099	1,09	1,1 (0,95*)	0,6	5,9
VGA0101	-	0,6	-	3,4
VGA0102	1,12	0,9	-	3,6
VGA0108	1,09	2,2 (2,18*)	2,3	3,5
VGA0109	1,40	0,9	-	4,9
B838	0,95	11,2 (10,8*)	3,3	3,5
B839	1,20	2,9 (3,2*)	2,9	27,7
B846	0,92	7,9 (7,55*)	2,4	6,9
B847	0,99	5,9 (5,9*)	3,1	4,4

*Bismuto kiekis įvertintas iš RSM matavimų.

pavaizduotos pav. 8.1(a). Difraktogramos smailės, matomos ties $2\theta = 66^\circ$, atitinka GaAs, o smailės kairėje priskiriamos epitaksiniams GaAsBi sluoksniams, kiekvienam bandiniui. Statmenos linijos, žyminčios Bi koncentraciją įtemptame GaAsBi junginyje, parodytos kaip gairės. Sluoksnių sudėčiai nustatyti naudotas XRD skenavimo dinaminis modeliavimas. Šie modeliavimai buvo atliekami darant prielaidą, kad tetragoninių iškraipymų nėra ir Bi kiekiui (x) GaAsBi sluoksniuose nustatyti taikomas Vegardo dėsnis. Analizuojant duomenis buvo naudotos GaBi ir GaAs gardelės konstantos, kurių vertės atitinkamai yra 6,324 Å ir 5,653 Å [35].

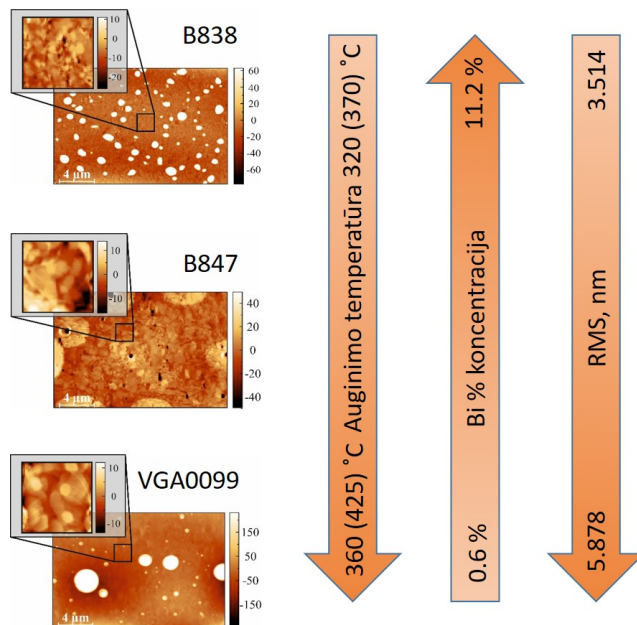
Tiksli bismuto koncentracija nustatyta iš RSM kito nuo 0,95% iki 10,8%. Nustatyta, kad visų bandinių relaksacijos lygis yra labai žemas ir svyruoja nuo 0,6% iki 3,3% GaAsBi sluoksniuose su mažiausiu ir didžiausiu Bi kiekiu atitinkamai (lentelė 8.1). Nustatyta, kad pagal RSM apskaičiuotas Bi kiekis sluoksniuose gerai sutampa su vertėmis, apskaičiuotomis pagal HR-XRD ω - 2θ difraktogramų matavimus (lentelė 8.1). GaAsBi epitaksinių sluoksnių matavimai rodo, kad sluoksnių relaksaciją lemia itin plonas GaAs buferinis sluoksnis,



Paveikslas 8.1 100 nm GaAsBi sluoksnių išmatuotos HR-XRD (004) plokštumos difraktogramos, kuriose Bi kiekis kito nuo 0,6% iki 11,2%. Vertikalios linijos žymi visiškai įtempto GaAsBi sluoksnio padėtį.

pasižymintis pakankamu paviršiaus šiurkštumu.

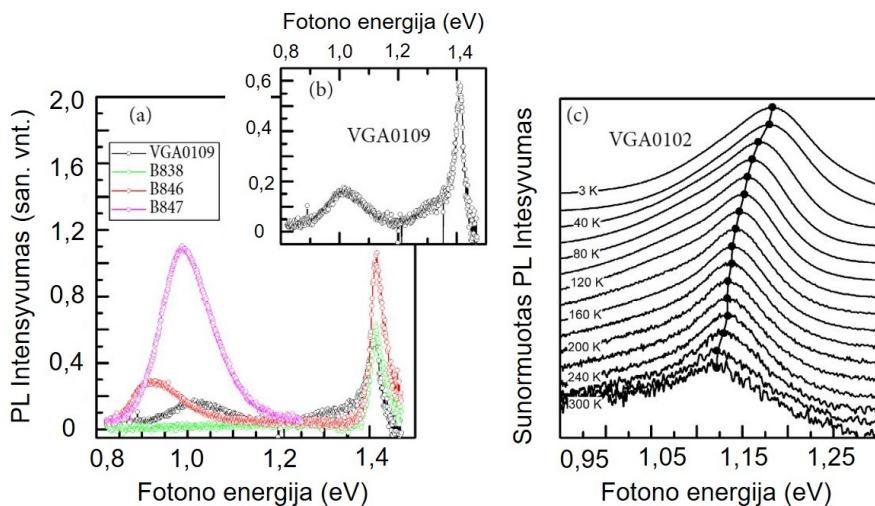
Bendras GaAsBi sluoksnių paviršiaus šiurkštumas, išmatuotas $20 \times 12 \mu\text{m}^2$ plote, svyruoja nuo 10 iki 40 nm, priklausomai nuo As/Ga srauto santykio, Bi srauto ir augimo temperatūros. Lygesnis paviršius pasiekiamas esant žemesnei augimo temperatūrai, ypač GaAsBi sluoksnių su didesniu Bi kiekiu, nors 100 nm storio sluoksnių. 8.2 paveikslėlyje matomos duobės ir lašai yra susiję su arseno trūkumu gardelėje ir Bi-Ga susidarymu paviršiuje, atitinkamai. B838, B847 ir VGA0099 bandinių paviršiaus šiurkštumas yra 3,5 nm, 4,4 nm ir 5,9 nm, atitinkamai, remiantis $2 \times 2 \mu\text{m}^2$ skenuojamo ploto dydžiu (visų bandinių vertės pateiktos lentelėje 8.1).



Paveikslas 8.2 Epitaksinių GaAsBi sluoksnių paviršiaus morfologiniai vaizdai su 11,2% (B838), 5,9% (B847) ir 1,1% (VGA0099) Bi kiekiu, augintų esant 1,075, 1,091 ir 1,076 As/Ga srautų santykiui ir 320 °C, 360 °C ir 425 °C padėklo temperatūroms. Rodyklės rodo apibendrintas augimo parametrų koreliacijos tendencijas MBE SVT-C-V-2 (MBE *Veeco GENxplor R&D*) aparaturoms: augimo temperatūros, įvesto bismuto kiekiui ir paviršiaus šiurkštumo atžvilgiu.

GaAsBi sluoksnių vidutinis paviršiaus šiurkštumas labai priklauso nuo augimo sąlygų, yra tiesiogiai susijęs su augimo temperatūra ir atvirkščiai proporcingas Bi srauto atžvilgiu. Žemesnė augimo temperatūra ir didesnis Bi srautas lemia didesnę įterptą Bi kiekį ir mažesnes RMS vertes optimalaus augimo lango ribose paveikslėlyje 8.2. Panašias tendencijas nurodė Bastimanas ir kt. [70].

PL spektrai kambario temperatūroje pateikti Pav.8.3(a). Matyti, kad



Paveikslas 8.3 100 nm GaAsBi sluoksnių su skirtingomis Bi koncentracijomis PL spektrai kambario temperatūroje (a), (b). Sluoksniu su 0,9% Bi (bandinys VGA0102) temperatūriniai PL spektrai, išmatuoti nuo 3 iki 300 K (c).

B serijos bandinių, išaugintų SVT-C-V-2 MBE reaktoriuje, PL spektrus sudaro dvi PL smailės. Didesnės energijos smailė, kurios maksimumas yra 1,42 eV, susijusi su optiniu perėjimu tūriniame GaAs padėkle. Žemesnės energijos smailė priskirta optiniams perėjimams GaAsBi sluoksnyje atitinka PL intensyvumo maksimumo padėtis ties 0,99 eV ir 0,92 eV GaAsBi sluoksniuose, kuriuose Bi koncentracija yra atitinkamai 5,9% (bandinys B847) ir 7,9% (bandinys B846). Didesnis PL intensyvumas B847 bandinyje, kuriame yra 5,9% Bi, susijęs su galimai mažesne nespindulinių centrų koncentracija dėl aukštesnės augimo temperatūros ir mažesnės Bi koncentracijos.

VGA serijos GaAsBi sluoksniai, kuriuose yra 0,9% Bi, PL spektrus kambario temperatūroje sudaro trys PL smailės (žr.pav 8.3(b)). PL smailė, esanti ties 1,42 eV, priskirta GaAs, o 1,42 eV PL smailės mažesnės energijos petys priskiriamas GaAsBi sluoksniui su 0,9% Bi. Mažą GaAsBi sluoksniu PL smailės intensyvumą galima paaiškinti fotosužadintų krūvininkų šiluminiais nuostoliais. PL smailės ties 1 eV kilmė nėra aiški ir gali būti susijusi su Bi praturtintomis GaAsBi sritimis dėl Bi drėkinamojo sluoksniu. GaAsBi sluoksniu, kuriame yra 0,9% Bi (bandinys VGA0102), temperatūriniai PL spektrai pavaizduoti pav.4.6(c). Matyti, kad PL smailės maksimumo padėtis, kintant tem-

peratūrai, kinta nuo 1,185 eV esant 3 K iki 1,122 eV esant 300 K. Pokyčio vertė 0,21 meV/K yra daug mažesnė nei GaAs (0,52 meV/K [35]) ir kitų įprastinių puslaidininkių. Be to, tai patvirtina prielaidą, kad mažos energijos PL smailė yra susijusi su optiniais perėjimais Bi praturtintose GaAsBi srityse.

Remiantis analize, nustatytos 100 nm GaAsBi sluoksnių optimalios augimo sąlygos MBE SVT-C-V-2 ir MBE *Veeco GENxplor R&D* aparatūroms. Esant As/Ga santykiui artimam vienetui ir žemai auginimo temperatūrai – 320 °C, bei padidintam Bi srautui – $1,8 \times 10^{-7}$ Torr - pasiekta didžiausia Bi koncentracija 11,2% Bi epitaksiniam sluoksnyje. Šie rezultatai ypač svarbūs gaminant šviesos diodus, kurių aktyvioji sritis yra 100 nm storio GaAsBi medžiagos sluoksnis.

8.3.2 GaAsBi/GaAs kvantinių duobių auginimo sąlygos ir rezultatai

Aukštos kokybės GaAsBi/(Al)GaAs daugybinių kvantinių duobių auginimas yra labai svarbus optoelektroninių prietaisų gamybai. Penktame disertacijos skyriuje aptariamos stačiakampių ir parabolinių GaAsBi kvantinių duobių auginimas ir analizė.

GaAsBi kvantinių duobių struktūros augintos naudojant *Veeco GENxplor R&D* MBE aparatūrą esant optimalioms augimo sąlygoms.

Išmatuoti stačiakampių GaAsBi kvantinių duobių PL spektrai. Bismuto kiekis apskaičiuotas naudojant *nextnano3* modeliavimą, remiantis vienos juostos efektyviosios masės aproksimacija. GaAsBi sluoksnių medžiagos parametrai buvo paimti iš Ref. [102], o vidutinė juostinės sandūros sumažėjimo vertė pasirinkta 65 meV 1%/Bi.

GaAsBi kvantinių struktūrų augimą riboja optimalių technologinių parametru rinkinys, t. y. padėklo temperatūra, As/Ga BEPR ir bismuto srautas. PL intensyvumas glaudžiai susijęs su į struktūrą įterptu Bi kiekiu. Todėl kvantinės struktūros su didesniu Bi kiekiu pavyzdžiui VGA0116 su 8,7% Bi, pasižymi daug mažesniu intensyvumu, kuris siekia tik 0,42 santykinių vienetų. Optimalus augimo režimas Bi srauto atžvilgiu, siekiant gauti didžiausią PL intensyvumą, pasiekiamas mažinant Bi srautą. Iš pradžių didesnis Bi kiekis įterpiamas didinant

Bi srautą. Tačiau tam tikrame PL intensyvumo priklausomybės nuo Bi srauto taške PL intensyvumas sumažėja. Taip gali būti dėl sustiprėjusio Bi klasterių arba nespindulinės rekombinacijos centrų susidarymo. Šis Bi perteklius tampa defektų generatoriumi, dėl kurio sumažėja PL intensyvumas. Augintos struktūros, suformuotos naudojant Bi srauto vertes, kurios svyruoja nuo BEPR verčių (atitinkamai $0,7 \times 10^{-7} - 0,9 \times 10^{-7}$ Torr ir 0,95 – 1,20), pasižymėjo didžiausiu PL smailės intensyvumu 1,45 – 4,8 eV. Tačiau pastebėta, kad pastarųjų struktūrų atsikartojamumas yra mažas todėl svarbu keisti kvantinės duobės architektūrą.

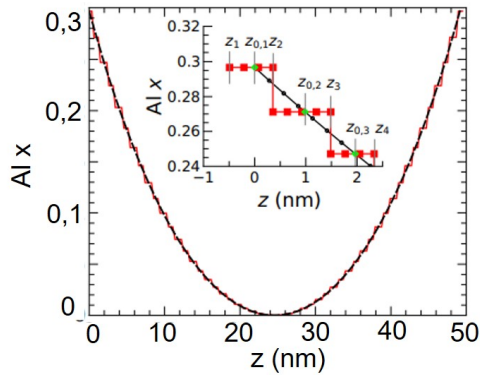
Neseniai Ref. [111] buvo parodyta, kad analoginis lydinio gradientinio kitimo metodas gali būti taikomas kaip alternatyvi technologinė priemonė, leidžianti auginti didelio tikslumo parabolines kvantines duobes, skirtas pažangiems optoelektroniniams prietaisams. Tyrimuose [111] buvo pasiūlyta MBE būdu auginti GaAsBi/AlGaAs QWs su paraboliniu potencialu, naudojant impulsinį analoginio lydinio gradientinio kitimo (PAAG) metodą. Tikslūs PAAG dizaino AlGaAs PQWs skaičiavimai pateikti straipsnyje Ref. [112].

Šis dizainas pagrįstas potencinės energijos moduliacijomis išilgai augimo krypties z ir buvo modeliuojamas naudojant parabolinę funkciją:

$$x(z) = x \left(\frac{z - z_0}{26,1} \right)^2 + 0,039 \left(\frac{z - z_0}{26,1} \right)^4. \quad (8.1)$$

PQW plotį z nuo 0 iki 49,155 nm galima diskretizuoti padalijus jį į $N = 51$ vienodais atstumais išdėstytus taškus. Al kiekio x reikšmės šiuose taškuose galima nustatyti pagal lygtį 8.1. Jei intervalą reikia užpildyti pastoviomis x reikšmėmis, reikia intervalą sudaryti tolygiai aplink centrinius taškus $z_{0,n}$. Tokiu būdu žingsnio pradžia žymima z_n , o žingsnio pabaiga (ir kito žingsnio pradžia) - z_{n+1} . Parabolinio Al pasiskirstymo, parodyto 8.4 paveiksle, ir, atitinkamai, barjero potencialo formavimosi būdas pavaizduotas 8.4 paveikslo intarpe.

Remiantis modeliavimo duomenimis, aliuminio kiekis x barjeruose turėtų būti 30%. Nustatyta, kad vienos pakopos plotis yra lygus dvigubai AlGaAs gardelės konstantai (apytiksliai 11 arba keturiems monosluoksniams). Taigi, modeliuojamas aliuminio kiekis turi kisti nuo 30% iki 0% ir vėl padidintas iki 30%.

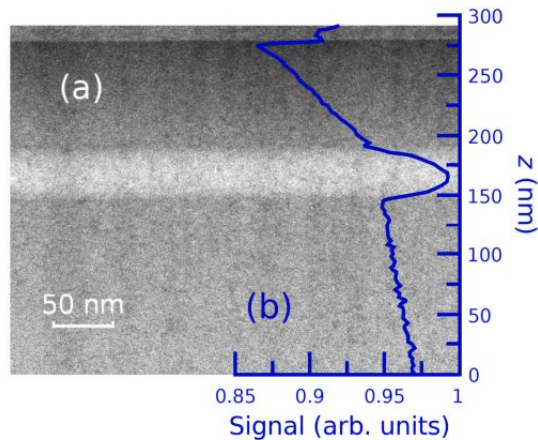


Paveikslas 8.4 PQW diskretizacija su 50 pakopų, kurias sudaro vienodai išsidėstę taškai išilgai PQW pločio nuo 0 nm iki 49,155 nm. Intarpe pavaizduotas grafinis diskretizacijos proceso vaizdas.

Remiantis skaičiavimais užaugintos parabolinės kvantinės struktūros naudojant *Veeco GENxplor R&D* MBE aparatūrą esant optimalioms augimo sąlygoms. STEM skerspjūvio nuotraukoje, pateiktoje 8.5(a) pav., matoma ryški juosta, susidariusi 100 nm žemiau viršutinio gaubiamojo sluoksnio. STEM signalas visoje nuskaitytoje srityje, išilgai z ašies, rodo parabolinį Al kiekio pasiskirstymą nuo barjerų į kvantinės duobės centrą. Kaip matyti iš 8.5(b) pav., pagal signalo profilį nustatyta, kad PQW plotis yra $51,5 \pm 0,2$ nm.

Norint išanalizuoti išaugintos struktūros kokybę, buvo išmatuoti PL spektrai esant skirtingam žadinimo intensyvumui naudojant 266 nm DPSS impulsinį lazerį, 3 K temperatūroje. Išmatuotos identifikuotų PQW PL smaيليų pozicijos leidžia nustatyti, ar užauginta PQW struktūra atitinka modeliavimą. Siekiant PL smailes priskirti konkretiems perėjimams, buvo atlikti suprojektuotos PQW struktūros FDS skaičiavimai. Išsami analizė pateikiama straipsnyje [112]. Analizė parodė, kad PQW išmatuoti PL spektrai puikiai sutampa su modeliavimu pav.8.6.

Buvo palyginti trijų tipų GaAsBi SQW ir MQW struktūrų dizainai. Pirmasis - standartiniai stačiakampiai MQW su AlGaAs barjeriais (apie 30% Al). Antrajame modelyje QW įterpta tarp dviejų arba trijų pakopų AlGaAs barjerių, kurių apačioje buvo AlGaAs arba grynas GaAs, o barjeruose buvo 15 ir 30% Al. Trečiąjį modelį sudarė GaAsBi SQW, įterptas

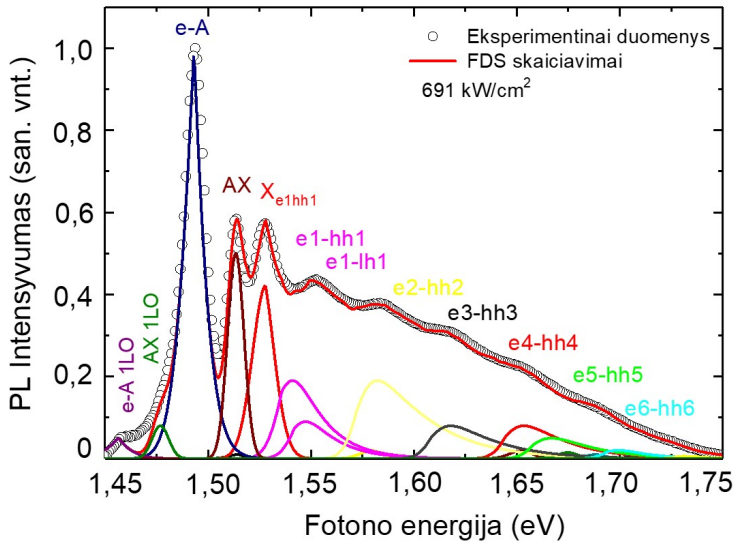


Paveikslas 8.5 (a) PQW struktūros skerspjūvio STEM vaizdas (b) normalizuotas signalo intensyvumo profilis (išsitiesinė mėlyna linija) visoje nuskaitytoje srityje, gautas išilgai augimo krypties.

tarp AlGaAs paraboliskai kintantis barjeras (PGB), su Al kiekiu nuo 30% viršuje iki 0% apačioje. Išsamus struktūrų auginimai aprašyti penktame disertacijos skyriuje. Pagrindiniai struktūros formavimo technologiniai parametrai pateikti lentelėje 8.2.

Lentelė 8.2 Pagrindiniai technologiniai GaAsBi/(Al, Ga)As QW struktūrų parametrai. Čia žymimi stačiakampio (1) tipo QWs, QWs su laiptuotais barjeriais (2) ir su AlGaAs PGBs (3).

	Bi, %	As/Ga	N_{QW}	d_{QW} , nm	E_P , eV	I_{PL} , san. vnt.	QW tipas
VGA0113	5,2	1,07	3	7	1,17	0,55	1
VGA0114	5,4	1,05	3	10	0,97	2	1
VGA0116	8,7	1,08	3	7	0,97	0,42	1
VGA0118	5,4	1,05	3	7	1,16	1,45	1
VGA0119	7,6	1,07	3	7	1,03	4,8	1
VGA0141	3,6	1,04	1	7	1,27	7,5	2
VGA0142	6	0,96	1	7	1,11	5	2
VGA0129	6,6	0,9	1	7	1,08	50	3
VGA0143	3,5	0,96	1	7	1,26	220	3
VGA0144	6,8	0,84	1	7	1,07	62	3
VGA0145	4,4	0,98	1	5	1,21	315	3

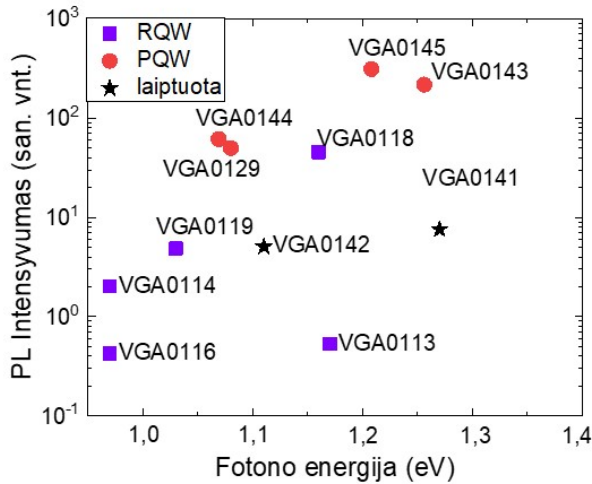


Paveikslas 8.6 PQW PL intensyvumo priklausomybė nuo fotono energijos esant 691 kW/cm^2 sužadinimo galiai, kur taškai atitinka eksperimentinį matavimą, o linijos - FDS teorinį modeliavimą.

Bendra tendencija, lyginant skirtingo dizaino struktūras, matoma paveikslėlyje 8.7. PL intensyvumas mažėja didėjant Bi kiekiui. Be to, PL intensyvumas beveik nepriklauso nuo QW skaičiaus, t. y. didėjant QW kiekiui fotoluminescencinės savybės pagerėjo nedaug. Kita vertus, žinoma, kad stačiakampių QWs PL intensyvumas gali būti kontroliuojamas Al kiekiu barjeruose [53].

PL matavimas parodė, kad GaAsBi SQW su AlGaAs PGB žymiai padidėja spindulinė rekombinacija. Parabolinių kvantinių duobių bandiniai buvo auginami toje pačioje $425 \text{ }^\circ\text{C}$ padėklo temperatūroje ir esant pastoviam Bi srautui, tik su skirtingais As/Ga BEPR. Todėl Bi kiekis SQW svyravo nuo 3,5% iki 6,8%, o tai matyti iš PL smailės padėties ties maždaug 1,26 ir 1,07 eV. Kaip matyti paveikslėlyje 8.7, tokios SQW konstrukcijos PL intensyvumas yra daugiau nei 50 kartų didesnis, palyginti su stačiakampio formos MQW ir SQW struktūromis su laiptuotu barjeru.

Sukurta technologija, skirta labai tikslioms 52 nm pločio GaAsBi/AlGaAs parabolinėms kvantinėms duobėms augini nau-

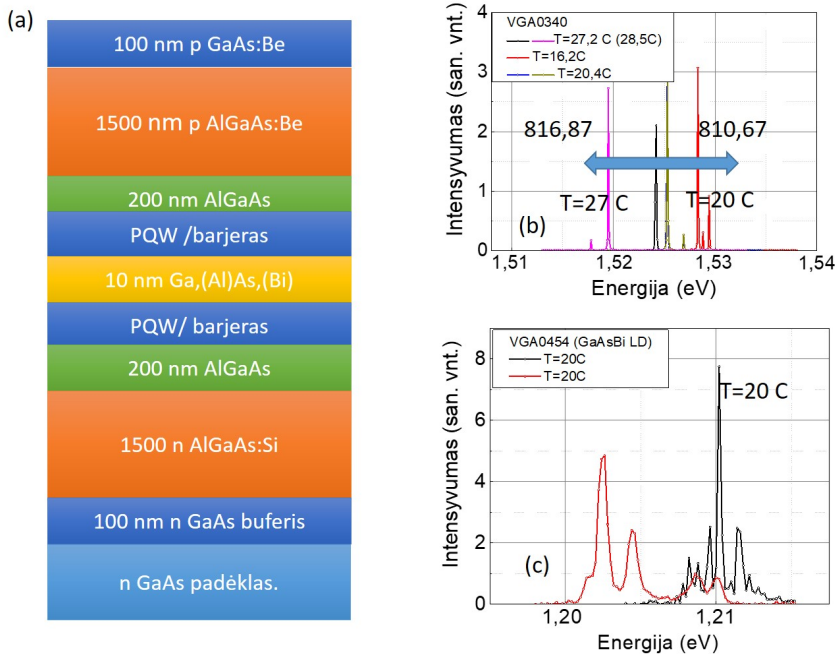


Paveikslas 8.7 GaAsBi QW struktūrų su paraboliniais AlGaAs barjeriais, laiptuotais AlGaAs barjeriais ir stačiakampiais AlGaAs barjeriais PL spektrų maksimumų smalių priklausomybės nuo PL intensyvumo kambario temperatūroje. PL intensyvumas mažėja didėjant emisijos bangos ilgiui, o tai atitinka didesnę Bi kiekį QWs.

dojant MBE. Pirmą kartą parabolinės GaAsBi QW struktūros buvo išaugintos su Bi kiekiu kvantinėje duobėje 2,6 – 6,8%, o didžiausias PL intensyvumas buvo pasiektas QW su AlGaAs PGB, kurių parabolėje buvo 30% Al. Žymus PL padidėjimas kambario temperatūroje gaunamas dėl padidėjusio lokalizacijos efekto GaAsBi QWs, kur dėl nehomogeniško Bi kiekio pasiskirstymo susidaro potencialas su energijos svyravimais 36 – 44 meV intervale. PGB sukuria palankias sąlygas krūvininkams įstrigti ir pereiti į apatines subjuostas, apribotas GaAsBi QWs, o neryški duobės ir barjero sąsaja sustiprina krūvininkų lokalizacijos efektą. Saviorganizuotas krūvininkų lokalizacijos pobūdis GaAsBi QWs lemia fotonų emisijos stabilumą. Tai suteikia galimybę gaminti GaAsBi kvantinių struktūrų pagrindu veikiančius lazerinius diodus, spinduliuojančius ilgesnes nei 1,2 μm bangas.

8.3.3 GaAsBi/GaAs NIR lazeriniai diodai

Remiantis parabolinių kvantinių duobių efektyvumu, buvo pagamintas skirtingų lazerinių diodų rinkinys. Palyginimui gam-



Paveikslas 8.8 Lazerinio diodo struktūra (a) ir išmatuoti lazeriavimo spektrai AlGaAs PQW VGA0340 (b) ir GaAsBi PQW VGA0454 (c) bandinams.

inti lazeriniai diodai su stačiakampėmis daugybinėmis AlGaAs ir GaAs kvantinėmis duobėmis kaip aktyviaja LD sritimi ir lazeriniai diodai su AlGaAs ir GaAsBi parabolinėmis pavienėmis kvantinėmis duobėmis. Buvo siekiama palyginti aktyviosios srities formos įtaką LD parametrų. Po to parabolinių GaAsBi struktūrų charakteristikos buvo palygintos su tomis, kurios nustatytos stačiakampėms GaAsBi lazerinių diodų struktūroms, anksčiau išaugintoms Butkutė *et al.* (2014) [13]. LD struktūros augintos ant n-tipo GaAs(001) padėklų, naudojant Veeco GENxplor R&D MBE. Taikytos standartinės augimo sąlygos: $T_{augimo} = 665 \text{ }^\circ\text{C}$ ir arseno perteklinis slėgis (visiškai atidarytas As vožtuvas), tuo tarpu GaAsBi QW žymiai žemesnėje temperatūroje ($415 - 425 \text{ }^\circ\text{C}$), kad būtų įvestas didesnis bismuto kiekis ir išvengta Bi segregacijos. Tiek n-tipo, tiek p-tipo bangolaidžio sluoksniai buvo $1,5 \text{ } \mu\text{m}$ storio legiruoti atitinkamai siliciu ir beriliu. Ni-Au metalo kontaktas ir Au-Ge kaip n-tipo ominis kontaktas nusodinti naudojant e-beam techniką. Maždaug $800 \text{ } \mu\text{m}$ ilgio ir $3.5 \text{ } \mu\text{m}$ pločio litografijos metodu

pagaminti lazeriniai diodai. Lazerinio diodo principinė struktūra pavaizduota pav.8.8(a).

Lazeriniai diodai, pagaminti iš AlGaAs su PQW ir RQW struktūromis, pasižymėjo tipiškomis I-V ir L-I charakteristikomis, o spinduliuojamos bangos ilgis siekė 780 – 829 nm. Lazeriniai diodai su parabolinėmis GaAsBi QW, pasižymėjo platesniu spinduliuotės spektru nuo 1024 nm iki 1031 nm pav.8.8(c). Lazerinių diodų, pagamintų iš AlGaAs RQW, slenkstinės srovės tankiai svyravo nuo 2,96 kA/cm² iki 3,50 kA/cm², o AlGaAs PQW ši srovė buvo artima 2,49 kA/cm². GaAsBi PQW lazerinių diodų slenkstinės srovės tankis buvo 3,8 kA/cm². Todėl LD su paraboline QW struktūra yra perspektyvesni, nes pasižymi mažesniu slenkstiniu srovės tankiu. Mažesnis slenkstinis srovės tankis reiškia, kad lazeriui pasiekti reikia mažesnės srovės. Šie rezultatai rodo, kad lazeriniai diodai, pagaminti keičiant aktyviosios srities sudėtį ir QW formą, turi didelį potencialą įvairiems taikymams.

8.4 Pagrindiniai rezultatai ir išvados

1. Optimalios MBE sąlygos auginant 100 nm storio GaAsBi sluoksnius, kuriuose Bi kiekis svyruoja nuo 0,6% iki 11,2% ant itin plonų (iki 20 nm) buferių, yra šios: auginimo temperatūra 320 – 425 °C, As/Ga slėgių santykis 0,95 – 1,18 ir Bi srautas 1.0×10^{-7} Torr – 1.8×10^{-7} Torr.
2. 100 nm storio GaAsBi sluoksniai su 0,6 – 11,2% Bi yra beveik įtempti. Sluoksnio relaksacija nepriklauso nuo Bi koncentracijos ir kinta nuo 0,6% iki 3,3%.
3. Eksperimentiškai įvertintas E_g jautrumas temperatūrai yra 0,21 meV/K⁻¹, t. y. du kartus mažesnis nei GaAs.
4. GaAsBi kvatinės duobės, kuriuose Bi koncentracija kinta nuo 2,6% iki 6,8%, buvo auginamos naudojant AlGaAs parabolinius gradientinius barjerus, kurių barjero viršuje yra 30% Al, o apačioje - grynas GaAs.
5. PL intensyvumo padidėjimas kambario temperatūroje PQW struktūrose susijęs su geresniu krūvininkų pagavimu GaAsBi

kvantinėje duobėje. Dėl parabolinės struktūros auginimo atsiradusi krūvininkų lokalizacija siekia 36 – 44 meV.

6. Skirtingų lazerinių diodų slenkstinės srovės buvo išmatuotos: 71 mA AlGaAs PQW, 51 – 98 mA AlGaAs RQW, 43 – 54 mA GaAs RQW ir 80 mA GaAsBi PQW, o galios vertės kambario temperatūroje svyruoja nuo 2 iki 10 mW.
7. Abiejų tipų RQW ir PQ WAlGaAs bei GaAs pagrindu pagaminti lazeriniai diodai pademonstravo lazeriavimą nuo 782 nm iki 829 nm. Nustatyta, kad slenkstinės srovės vertės AlGaAs PQW pagrindu veikiančiuose LD yra maždaug 70 mA, AlGaAs RQW pagrindu veikiančiuose LD - nuo 50 mA iki 100 mA, o GaAs RQW pagrindu veikiančiuose LD - nuo 40 mA iki 50 mA. Apskaičiuoti slenkstinės srovės tankiai (J_{th}) buvo atitinkamai 2,49 kA/cm², 2,48 – 3,50 kA/cm², 2,96 – 3,40 kA/cm².
8. Lazeriniai diodai su GaAsBi parabolinėmis QW struktūromis lazeriuoja 1024 – 1031 nm diapazone, priklausomai nuo LD veidrodžių kokybės. GaAsBi PQW slenkstinė srovės vertė buvo maždaug 80 mA o apskaičiuotas $J_{th} = 3,8$ kA/cm².

REFERENCES

- [1] Vladimir Liger, Vladimir Mironenko, Yury Kuritsyn, and Mikhail Bolshov. Advanced fiber-coupled diode laser sensor for calibration-free 1f-wms determination of an absorption line intensity. *Sensors*, **20**(21), 2020.
- [2] Zhimin Peng, Yanjun Du, and Yanjun Ding. Highly sensitive, calibration-free wm-das method for recovering absorbance—part i: Theoretical analysis. *Sensors*, **20**(3), 2020.
- [3] Catalin Palade, Ionel Stavarache, Toma Stoica, and Magdalena Lidia Ciurea. Gesi nanocrystals photo-sensors for optical detection of slippery road conditions combining two classification algorithms. *Sensors*, **20**(21), 2020.
- [4] Y. Tominaga, K. Oe, and M. Yoshimoto. Low temperature dependence of oscillation wavelength in $\text{GaAs}_{1-x}\text{Bi}_x$ by photo pumping. *Applied Physics Express*, **3**(6):062201, 2010.
- [5] P. Ludewig, N. Knaub, N. Hossain, S. Reinhard, L. Nattermann, I. P. Marko, S. R. Jin, K. Hild, S. Chatterjee, W. Stolz, S. J. Sweeney, and K. Volz. Electrical injection $\text{Ga}(\text{AsBi})/(\text{AlGa})\text{As}$ single quantum well laser. *Applied Physics Letters*, **102**(24):242115, 2013.
- [6] Pallavi Kisan Patil, Esperanza Luna, Teruyoshi Matsuda, Kohki Yamada, Keisuke Kamiya, Fumitaro Ishikawa, and Satoshi Shimomura. $\text{GaAsBi}/\text{GaAs}$ multi-quantum well LED grown by molecular beam epitaxy using a two-substrate-temperature technique. *Nanotechnology*, **28**(10):105702, feb 2017.
- [7] Chris J. Hunter, Faebian Bastiman, Abdul R. Mohmad, Robert Richards, Jo Shien Ng, Stephen J. Sweeney, and John P. R.

- David. Absorption characteristics of GaAs_{1-x}Bi_x/GaAs diodes in the near-infrared. *IEEE Photonics Technology Letters*, **24**(23):2191–2194, 2012.
- [8] B. Fluegel, S. Francoeur, A. Mascarenhas, S. Tixier, E. C. Young, and T. Tiedje. Giant spin-orbit bowing in GaAs_{1-x}Bi_x. *Phys. Rev. Lett.*, **97**:067205, Aug 2006.
- [9] R. N. Kini, L. Bhusal, A. J. Ptak, R. France, and A. Mascarenhas. Electron hall mobility in GaAsBi. *Journal of Applied Physics*, **106**(4):043705, 2009.
- [10] S. Francoeur, M.-J. Seong, A. Mascarenhas, S. Tixier, M. Adamcyk, and T. Tiedje. Band gap of GaAs_{1-x}Bi_x, $0 < x < 3.6\%$. *Applied Physics Letters*, **82**(22):3874–3876, 2003.
- [11] Junichi Yoshida, Takashi Kita, Osamu Wada, and Kunishige Oe. Temperature dependence of GaAs_{1-x}Bi_x band gap studied by photoreflectance spectroscopy. *Japanese Journal of Applied Physics*, **42**(Part 1, No. 2A):371–374, Feb 2003.
- [12] C A Broderick, M Usman, S J Sweeney, and E P O'Reilly. Band engineering in dilute nitride and bismide semiconductor lasers. *Semiconductor Science and Technology*, **27**(9):094011, aug 2012.
- [13] R. Butkutė, A. Geižutis, V. Pačebutas, B. Čechavičius, V. Bukauskas, R. Kundrotas, P. Ludewig, K. Volz, and A. Krotkus. Multi-quantum well Ga(AsBi)/GaAs laser diodes with more than 6% of bismuth. *Electronics Letters*, **50**(16):1155–1157, 2014.
- [14] A. M. Jean-Louis, B. Ayrault, and J. Vargas. Propriétés des alliages InSb_{1-x}Bi_x ii. absorption optique. *physica status solidi (b)*, **34**(1):341–350, 1969.
- [15] B. Joukoff and A.M. Jean-Louis. Growth of InSb_{1-x}Bi_x single crystals by czochralski method. *Journal of Crystal Growth*, **12**(2):169–172, 1972.
- [16] K. Y. Ma, Z. M. Fang, D. H. Jaw, R. M. Cohen, G. B. Stringfellow, W. P. Kosar, and D. W. Brown. Organometallic vapor phase epi-

- taxial growth and characterization of InAsBi and InAsSbBi. *Applied Physics Letters*, **55**(23):2420–2422, 1989.
- [17] Kunishige Oe, Seigo Ando, and Koichi Sugiyama. InSb_{1-x}Bi_x films grown by molecular beam epitaxy. *Japanese Journal of Applied Physics*, **20**(4):L303–L306, Apr 1981.
- [18] A. J. Noreika, W. J. Tekei, M. H. Francombe, and C. E. Wood. Indium antimonide bismuth compositions grown by molecular beam epitaxy. *Journal of Applied Physics*, **53**(7):4932–4937, 1982.
- [19] T. P. Humphreys, P. K. Chiang, S. M. Bedair, and N. R. Parikh. Metalorganic chemical vapor deposition and characterization of the InAsBi material system for infrared detection. *Applied Physics Letters*, **53**(2):142–144, 1988.
- [20] R. F. C. Farrow. The stabilization of metastable phases by epitaxy. *Journal of Vacuum Science & Technology B: Microelectronics Processing and Phenomena*, **1**(2):222–228, 1983.
- [21] Kunishige Oe and Hiroshi Okamoto. New semiconductor alloy GaAs_{1-x}Bi_x grown by metal organic vapor phase epitaxy. *Japanese Journal of Applied Physics*, **37**(Part 2, No. 11A):L1283–L1285, Nov 1998.
- [22] Kunishige Oe and Hiromitsu Asai. Proposal on a temperature-insensitive wavelength semiconductor laser. *IEICE Transactions on Electronics*, **79**:1751–1759, 1996.
- [23] Gan Feng, Masahiro Yoshimoto, Kunishige Oe, Akiyoshi Chayahara, and Yuji Horino. New III-V semiconductor InGaAsBi alloy grown by molecular beam epitaxy. *Japanese Journal of Applied Physics*, **44**(No. 37):L1161–L1163, Sep 2005.
- [24] J. P. Petropoulos, Y. Zhong, and J. M. O. Zide. Optical and electrical characterization of InGaBiAs for use as a mid-infrared optoelectronic material. *Applied Physics Letters*, **99**(3):031110, 2011.
- [25] S.K. Das, T.D. Das, S. Dhar, M. de la Mare, and A. Krier. Near infrared photoluminescence observed in dilute GaSbBi al-

- loys grown by liquid phase epitaxy. *Infrared Physics Technology*, **55**(1):156–160, 2012.
- [26] S. Tixier, M. Adamcyk, T. Tiedje, S. Francoeur, A. Mascarenhas, Peng Wei, and F. Schiettekatte. Molecular beam epitaxy growth of GaAs_{1-x}Bi_x. *Applied Physics Letters*, **82**(14):2245–2247, 2003.
- [27] Kunishige Oe. Characteristics of semiconductor alloy GaAs_{1-x}Bi_x. *Japanese Journal of Applied Physics*, **41**(Part 1, No. 5A):2801–2806, May 2002.
- [28] R. B. Lewis, D. A. Beaton, Xianfeng Lu, and T. Tiedje. GaAs_{1-x}Bi_x light emitting diodes. *Journal of Crystal Growth*, **311**(7):1872–1875, 2009. International Conference on Molecular Beam Epitaxy (MBE-XV).
- [29] A. Mascarenhas, Yong Zhang, Jason Verley, and M.J. Seong. Overcoming limitations in semiconductor alloy design. *Superlattices and Microstructures*, **29**(6):395–404, 2001.
- [30] Masahiro Yoshimoto, Satoshi Murata, Akiyoshi Chayahara, Yuji Horino, Junji Saraie, and Kunishige Oe. Metastable GaAsBi alloy grown by molecular beam epitaxy. *Japanese Journal of Applied Physics*, **42**(Part 2, No. 10B):L1235–L1237, oct 2003.
- [31] A. J. Ptak, R. France, D. A. Beaton, K. Alberi, J. Simon, A. Mascarenhas, and C.-S. Jiang. Kinetically limited growth of GaAsBi by molecular-beam epitaxy. *Journal of Crystal Growth*, **338**(1):107–110, 2017.
- [32] Xianfeng Lu, D. A. Beaton, R. B. Lewis, T. Tiedje, and Yong Zhang. Composition dependence of photoluminescence of GaAs_{1-x}Bi_x alloys. *Applied Physics Letters*, **95**(4):041903, 2009.
- [33] M. Masnadi-Shirazi, R. B. Lewis, V. Bahrami-Yekta, T. Tiedje, M. Chicoine, and P. Servati. Bandgap and optical absorption edge of GaAs_{1-x}Bi_x alloys with 0 < x < 17.8%. *Journal of Applied Physics*, **116**(22):223506, 2014.

- [34] R. B. Lewis, M. Masnadi-Shirazi, and T. Tiedje. Growth of high bi concentration GaAs_{1-x}Bi_x by molecular beam epitaxy. *Applied Physics Letters*, **101**(8):082112, 2012.
- [35] I. Vurgaftman, J. R. Meyer, and L. R. Ram-Mohan. Band parameters for III–V compound semiconductors and their alloys. *Journal of Applied Physics*, **89**(11):5815–5875, 2001.
- [36] D. L. Smith and C. Mailhot. Theory of semiconductor superlattice electronic structure. *Rev. Mod. Phys.*, **62**:173–234, Jan 1990.
- [37] M G Burt. The justification for applying the effective-mass approximation to microstructures. *Journal of Physics: Condensed Matter*, **4**(32):6651–6690, aug 1992.
- [38] Guobin Liu, Shun-Lien Chuang, and Seoung-Hwan Park. Optical gain of strained GaAsSb/GaAs quantum-well lasers: A self-consistent approach. *Journal of Applied Physics*, **88**(10):5554–5561, 2000.
- [39] R. L Moon, G. A. Antypas, and L. W. James. Bandgap and lattice constant of GaInAsP as a function of alloy composition. *Journal of Electronic Materials*, **3**(3):635–644, 1974.
- [40] U. Tisch, E. Finkman, and J. Salzman. The anomalous bandgap bowing in GaAsN. *Applied Physics Letters*, **81**(3):463–465, 2002.
- [41] A. Janotti, Su-Huai Wei, and S. B. Zhang. Theoretical study of the effects of isovalent coalloying of Bi and N in GaAs. *Phys. Rev. B*, **65**:115203, Feb 2002.
- [42] Z Chine, H Fitouri, I Zaied, A Rebey, and B El Jani. Photoreflectance and photoluminescence study of annealing effects on GaAsBi layers grown by metalorganic vapor phase epitaxy. *Semiconductor Science and Technology*, **25**(6):065009, may 2010.
- [43] K. Alberi, J. Wu, W. Walukiewicz, K. M. Yu, O. D. Dubon, S. P. Watkins, C. X. Wang, X. Liu, Y.-J. Cho, and J. Furdyna. Valence-band anticrossing in mismatched III-V semiconductor alloys. *Phys. Rev. B*, **75**:045203, Jan 2007.

REFERENCES

- [44] W. Shan, W. Walukiewicz, J. W. Ager, E. E. Haller, J. F. Geisz, D. J. Friedman, J. M. Olson, and S. R. Kurtz. Band anticrossing in GaInNAs alloys. *Phys. Rev. Lett.*, **82**:1221–1224, Feb 1999.
- [45] Muhammad Usman, Christopher A. Broderick, Andrew Lindsay, and Eoin P. O'Reilly. Tight-binding analysis of the electronic structure of dilute bismide alloys of GaP and GaAs. *Phys. Rev. B*, **84**:245202, Dec 2011.
- [46] Pierre Carrier and Su-Huai Wei. Calculated spin-orbit splitting of all diamondlike and zinc-blende semiconductors: Effects of $p_{1/2}$ local orbitals and chemical trends. *Phys. Rev. B*, **70**:035212, Jul 2004.
- [47] T. Tiedje, E.C. Young, and A. Mascarenhas. Growth and properties of the dilute bismide semiconductor GaAs $_{1-x}$ Bi $_x$ a complementary alloy to the dilute nitrides. *International Journal of Nanotechnology*, **5**(9-12):963–983, 2008.
- [48] Stephen J. Sweeney. Bismide alloys for higher efficiency infrared semiconductor lasers. In *22nd IEEE International Semiconductor Laser Conference*, pages 111–112, 2010.
- [49] V. Pačebutas, K. Bertulis, G. Aleksejenko, and A. Krotkus. Molecular-beam-epitaxy grown GaBiAs for terahertz optoelectronic applications. *Journal of Materials Science: Materials in Electronics*, **20**:1573, 2009.
- [50] D. G. Cooke, F. A. Hegmann, E. C. Young, and T. Tiedje. Electron mobility in dilute GaAs bismide and nitride alloys measured by time resolved terahertz spectroscopy. *Applied Physics Letters*, **89**(12):122103, 2006.
- [51] Muhammad Usman, Christopher A. Broderick, Zahida Batool, Konstanze Hild, Thomas J. C. Hosea, Stephen J. Sweeney, and Eoin P. O'Reilly. Impact of alloy disorder on the band structure of compressively strained GaAsBi. *Phys. Rev. B*, **87**:115104, Mar 2013.

- [52] Sebastian Imhof, Angela Thränhardt, Alexej Chernikov, Martin Koch, Niko S. Köster, Kolja Kolata, Sangam Chatterjee, Stephan W. Koch, Xianfeng Lu, Shane R. Johnson, Dan A. Beaton, Thomas Tiedje, and Oleg Rubel. Clustering effects in Ga(AsBi). *Applied Physics Letters*, **96**(13):131115, 2010.
- [53] Yu I Mazur, V G Dorogan, M Benamara, M E Ware, M Schmidbauer, G G Tarasov, S R Johnson, X Lu, S-Q Yu, T Tiedje, and G J Salamo. Effects of spatial confinement and layer disorder in photoluminescence of GaAs_{1-x}Bi_x/GaAs heterostructures. *Journal of Physics D: Applied Physics*, **46**(6):065306, jan 2013.
- [54] M. K. Shakfa, D. Kalincev, X. Lu, S. R. Johnson, D. A. Beaton, T. Tiedje, A. Chernikov, S. Chatterjee, and M. Koch. Quantitative study of localization effects and recombination dynamics in GaAsBi/GaAs single quantum wells. *Journal of Applied Physics*, **114**(16):164306, 2013.
- [55] A. R. Mohmad, F. Bastiman, J. S. Ng, S. J. Sweeney, and J. P. R. David. Photoluminescence investigation of high quality GaAs_{1-x}Bi_x on GaAs. *Applied Physics Letters*, **98**(12), 03 2011.
- [56] Chaturvedi Gogineni, Nathaniel A. Riordan, Shane R. Johnson, Xianfeng Lu, and Tom Tiedje. Disorder and the urbach edge in dilute bismide GaAsBi. *Applied Physics Letters*, **103**(4):041110, 2013.
- [57] M. K. Shakfa, M. Wiemer, P. Ludewig, K. Jandieri, K. Volz, W. Stolz, S. D. Baranovskii, and M. Koch. Thermal quenching of photoluminescence in Ga(AsBi). *Journal of Applied Physics*, **117**(2):025709, 2015.
- [58] T. Wilson, N.P Hylton, Y. Harada, P. Pearce, D. Alonso-Alvarez, A. Mellor, R.D. Richards, J.P.R. David, and N.J. Ekins-Daukes. Assessing the nature of the distribution of localised states in bulk GaAsBi. *Scientific Reports*, **8**(6457), 2018.
- [59] Andrew G. Norman, Ryan France, and Aaron J. Ptak. Atomic ordering and phase separation in mbe GaAs_{1-x}Bi_x. *Journal of Vacuum Science & Technology B*, **29**(3):03C121, 2011.

- [60] Mingjian Wu, Esperanza Luna, Janne Puustinen, Mircea Guina, and Achim Trampert. Formation and phase transformation of Bi-containing QD-like clusters in annealed GaAsBi. *Nanotechnology*, **25**(20):205605, apr 2014.
- [61] Jason A. Morgan and Gilbert M. Nathanson. Atom scattering from atomic surfactants: Collisions of argon with a dilute Bi:Ga solution. *The Journal of Chemical Physics*, **114**(5):1958–1961, 2001.
- [62] S. Tixier, M. Adamczyk, E.C. Young, J.H. Schmid, and T. Tiedje. Surfactant enhanced growth of GaNAs and InGaNAs using bismuth. *Journal of Crystal Growth*, **251**(1):449–454, 2003. Proceedings of the Twelfth International Conference on Molecular Beam Epitaxy.
- [63] Lijuan Wang, Liyao Zhang, Li Yue, Dan Liang, Xiren Chen, Yaoyao Li, Pengfei Lu, Jun Shao, and Shumin Wang. Novel dilute bismide, epitaxy, physical properties and device application. *Crystals*, **7**(3), 2017.
- [64] H. Fitouri, I. Moussa, A. Rebey, and B. El Jani. Study of GaAsBi MOVPE growth on (100) GaAs substrate under high Bi flow rate by high resolution X-ray diffraction. *Microelectronic Engineering*, **88**(4):476–479, 2011.
- [65] A.J. Ptak, R. France, D.A. Beaton, K. Alberi, J. Simon, A. Mascarenhas, and C.-S. Jiang. Kinetically limited growth of GaAsBi by molecular-beam epitaxy. *Journal of Crystal Growth*, **338**(1):107–110, 2012.
- [66] Vaidas Pačebutas, Renata Butkutė, Bronius Čechavičius, Julius Kavaliauskas, and Arūnas Krotkus. Photoluminescence investigation of GaAs_{1-x}Bi_x/GaAs heterostructures. *Thin Solid Films*, **520**(20):6415–6418, 2012.
- [67] G. Ciatto, M. Thomasset, F. Glas, X. Lu, and T. Tiedje. Formation and vanishing of short range ordering in GaAs_{1-x}Bi_x thin films. *Phys. Rev. B*, 82:201304, Nov 2010.

- [68] E.C. Young, S. Tixier, and T. Tiedje. Bismuth surfactant growth of the dilute nitride $\text{GaN}_x\text{As}_{1-x}$. *Journal of Crystal Growth*, 279(3):316–320, 2005.
- [69] X. Lu, D. A. Beaton, R. B. Lewis, T. Tiedje, and M. B. Whitwick. Effect of molecular beam epitaxy growth conditions on the bi content of $\text{GaAs}_{1-x}\text{Bi}_x$. *Applied Physics Letters*, 92(19):192110, 2008.
- [70] F. Bastiman, A.R.B. Mohmad, J.S. Ng, J.P.R David, and S.J. Sweeney. Non-stoichiometric $\text{GaAsBi}/\text{GaAs}$ (100) molecular beam epitaxy growth. *Journal of Crystal Growth*, 338(1):57–61, 2012.
- [71] A. R. Mohmad, F. Bastiman, C. J. Hunter, R. D. Richards, S. J. Sweeney, J. S. Ng, J. P. R. David, and B. Y. Majlis. Localization effects and band gap of GaAsBi alloys. *physica status solidi (b)*, 251(6):1276–1281, 2014.
- [72] T.B.O. Rockett, R.D. Richards, Y. Gu, F. Harun, Y. Liu, Z. Zhou, and J.P.R. David. Influence of growth conditions on the structural and opto-electronic quality of GaAsBi . *Journal of Crystal Growth*, 477:139–143, 2017.
- [73] Thomas Walther, Robert D. Richards, and Faebian Bastiman. Scanning transmission electron microscopy measurement of bismuth segregation in thin $\text{Ga}(\text{As},\text{Bi})$ layers grown by molecular beam epitaxy. *Crystal Research and Technology*, 50(1):38–42, 2015.
- [74] Vahid Bahrami-Yekta, Thomas Tiedje, and Mostafa Masnadi-Shirazi. Mbe growth optimization for $\text{GaAs}_{1-x}\text{Bi}_x$ and dependence of photoluminescence on growth temperature. *Semiconductor Science and Technology*, 30(9):094007, jun 2015.
- [75] Kyohei Kakuyama, Sho Hasegawa, Hiroyuki Nishinaka, and Masahiro Yoshimoto. Impact of a small change in growth temperature on the tail states of GaAsBi . *Journal of Applied Physics*, 126(4), 07 2019.
- [76] Chaturvedi Riordan, Nathaniel A. Gogineni, Sahne R Johnson, Xianfeng Lu, Tom Tiedje, Ding Ding, Yong-Hang Zhang,

- Rafael Fritz, Kolja Kolata, Sangam Chatterjee, Kerstin Volz, and Stephan W Koch. Temperature and pump power dependent photoluminescence characterization of MBE grown GaAsBi on GaAs. *Journal of Materials Science: Materials in Electronics*, **23**(1799), 2012.
- [77] C. Ryan Tait, Lifan Yan, and Joanna M. Millunchick. Spontaneous nanostructure formation in GaAsBi alloys. *Journal of Crystal Growth*, **493**:20–24, 2018.
- [78] Wenwu Pan, Lijuan Wang, Yanchao Zhang, Wen Lei, and Shumin Wang. MBE growth strategy and optimization of GaAsBi quantum well light emitting structure beyond 1.2 μm . *Applied Physics Letters*, **114**(15), 04 2019.
- [79] J. Puustinen, M. Wu, E. Luna, A. Schramm, P. Laukkanen, M. Laitinen, T. Sajavaara, and M. Guina. Variation of lattice constant and cluster formation in GaAsBi. *Journal of Applied Physics*, **114**(24), 12 2013.
- [80] C. Cornille, A. Arnoult, Q. Gravelier, and C. Fontaine. Links between bismuth incorporation and surface reconstruction during GaAsBi growth probed by *in situ* measurements. *Journal of Applied Physics*, **126**(9):093106, 2019.
- [81] Wolfgang Bennarndt, Gerhard Boehm, and Markus-Christian Amann. Domains of molecular beam epitaxial growth of Ga(In)AsBi on GaAs and InP substrates. *Journal of Crystal Growth*, **436**:56–61, 2016.
- [82] S. J. Sweeney, A. R. Adams, M. Silver, E. P. O’Reilly, J. R. Watling, A. B. Walker, and P. J. A. Thijs. Dependence of threshold current on QW position and on pressure in 1.5 μm InGaAs(P) lasers. *physica status solidi (b)*, **211**(1):525–531, 1999.
- [83] S. J. Sweeney and S. R. Jin. Bismide-nitride alloys: Promising for efficient light emitting devices in the near- and mid-infrared. *Journal of Applied Physics*, **113**(4):043110, 2013.
- [84] R.D. Richards, A. Mellor, F. Harun, J.S. Cheong, N.P. Hylton, T. Wilson, T. Thomas, J.S. Roberts, N.J. Ekins-Daukes, and J.P.R.

- David. Photovoltaic characterisation of GaAsBi/GaAs multiple quantum well devices. *Solar Energy Materials and Solar Cells*, **172**:238–243, 2017.
- [85] Takuma Fuyuki, Ryo Yoshioka, Kenji Yoshida, and Masahiro Yoshimoto. Long-wavelength emission in photo-pumped GaAs_{1-x}Bi_x laser with low temperature dependence of lasing wavelength. *Applied Physics Letters*, **103**(20):202105, 2013.
- [86] I P Marko, P Ludewig, Z L Bushell, S R Jin, K Hild, Z Batool, S Reinhard, L Nattermann, W Stolz, K Volz, and S J Sweeney. Physical properties and optimization of GaBiAs/(al)GaAs based nearinfrared laser diodes grown by MOVPE with up to 4.4% bi. *Journal of Physics D: Applied Physics*, **47**(34):345103, aug 2014.
- [87] Takuma Fuyuki, Kenji Yoshida, Ryo Yoshioka, and Masahiro Yoshimoto. Electrically pumped room temperature operation of diodes with low temperature dependence of oscillation wavelength. *Applied Physics Express*, **7**(8):082101, jul 2014.
- [88] Christopher A. Broderick, Patrick E. Harnedy, and Eoin P. O'Reilly. Theory of the electronic and optical properties of dilute bismide quantum well lasers. *IEEE Journal of Selected Topics in Quantum Electronics*, **21**(6):287–299, 2015.
- [89] Xiaoyan Wu, Wenwu Pan, Zhenpu Zhang, Yaoyao Li, Chunfang Cao, Juanjuan Liu, Liyao Zhang, Yuxin Song, Haiyan Ou, and Shumin Wang. 1.142 μm GaAsBi/GaAs quantum well lasers grown by molecular beam epitaxy. *ACS Photonics*, **4**(6):1322–1326, 2017.
- [90] Juanjuan Liu, Wenwu Pan, Xiaoyan Wu, Chunfang Cao, Yaoyao Li, Xiren Chen, Yanchao Zhang, Lijuan Wang, Jinyi Yan, Dongliang Zhang, Yuxin Song, Jun Shao, and Shumin Wang. Electrically injected gaasbi/gaas single quantum well laser diodes. *AIP Advances*, **7**(11):115006, 2017.
- [91] Justinas Glemža, Vilius Palenskis, Andrejus Geižutis, Bronislovas Čechavičius, Renata Butkutė, Sandra Pralgauskaitė, and Jonas

- Matukas. Low-frequency noise investigation of 1.09 μm GaAsBi laser diodes. *Materials*, **12**(4), 2019.
- [92] Xiu Liu, Lijuan Wang, Xuan Fang, Taojie Zhou, Guohong Xiang, Boyuan Xiang, Xueqing Chen, Suikong Hark, Hao Liang, Shumin Wang, and Zhaoyu Zhang. Continuous wave operation of GaAsBi microdisk lasers at room temperature with large wavelengths ranging from 1.27 to 1.41 μm . *Photon. Res.*, **7**(5):508–512, May 2019.
- [93] Honghyuk Kim, Yingxin Guan, Kamran Forghani, Thomas F. Kuech, and Luke J. Mawst. Strain-compensated Ga(AsP)/Ga(AsBi)/Ga(AsP) quantum-well active-region lasers (Conference Presentation). In Alexey A. Belyanin and Peter M. Snowton, editors, *Novel In-Plane Semiconductor Lasers XVI*, volume **10123**, page 1012304. International Society for Optics and Photonics, SPIE, 2017.
- [94] P. Ludewig, Z.L. Bushell, L. Nattermann, N. Knaub, W. Stolz, and K. Volz. Growth of Ga(AsBi) on GaAs by continuous flow MOVPE. *Journal of Crystal Growth*, **396**:95–99, 2014.
- [95] A. Y. Cho. Film deposition by molecular-beam techniques. *Journal of Vacuum Science and Technology*, **8**(5):S31–S38, 1971.
- [96] A. Y. Cho. GaAs epitaxy by a molecular beam method: Observations of surface structure on the (001) face. *Journal of Applied Physics*, **42**(5):2074–2081, 1971.
- [97] Ahn lab - subpage 2. <https://ahnlab.yale.edu/subpage-2>.
- [98] C.T. Foxon and B.A. Joyce. Growth and characterisation of semiconductors. *P Publishing Ltd*, 1990.
- [99] M. Masnadi-Shirazi, D.A. Beaton, R.B. Lewis, Xianfeng Lu, and T. Tiedje. Surface reconstructions during growth of GaAs_{1-x}Bi_x alloys by molecular beam epitaxy. *Journal of Crystal Growth*, **338**(1):80–84, 2012.

- [100] J. Ralston, G. W. Wicks, and L. F. Eastman. Reflection high energy electron diffraction intensity oscillation study of Ga desorption from molecular beam epitaxially grown $\text{Al}_x\text{Ga}_{1-x}\text{As}$. *Journal of Vacuum Science & Technology B: Microelectronics Processing and Phenomena*, 4(2):594–597, 1986.
- [101] G. Vardar, S. W. Paleg, M. V. Warren, M. Kang, S. Jeon, and R. S. Goldman. Mechanisms of droplet formation and Bi incorporation during molecular beam epitaxy of GaAsBi. *Applied Physics Letters*, 102(4):042106, 2013.
- [102] V. Karpus, R. Norkus, R. Butkutė, S. Stanionytė, B. Čechavičius, and A. Krotkus. THz-excitation spectroscopy technique for band-offset determination. *Opt. Express*, 26(26):33807–33817, Dec 2018.
- [103] R. C. Miller, A. C. Gossard, D. A. Kleinman, and O. Munteanu. Parabolic quantum wells with the GaAs-AlGaAs system. *Phys. Rev. B*, 29:3740–3743, Mar 1984.
- [104] L. Brey, N. F. Johnson, and B. I. Halperin. Optical and magneto-optical absorption in parabolic quantum wells. *Phys. Rev. B*, 40:10647–10649, Nov 1989.
- [105] R. F. Kopf, M. H. Herman, M. Lamont Schnoes, A. P. Perley, G. Livescu, and M. Ohring. Band offset determination in analog graded parabolic and triangular quantum wells of GaAs/AlGaAs and GaInAs/AlInAs. *Journal of Applied Physics*, 71(10):5004–5011, 1992.
- [106] F. Kyrychenko and J. Kossut. Excitons in parabolic quantum wells. *Semiconductor Science and Technology*, 13(10):1076, Oct 1998.
- [107] Emine Ozturk and Ismail Sokmen. Nonlinear intersubband transitions in a parabolic and an inverse parabolic quantum well under applied magnetic field. *Journal of Luminescence*, 145:387–392, 2014.
- [108] B. Paulillo, J.-M. Manceau, L. H. Li, A. G. Davies, E. H. Linfield, and R. Colombelli. Room temperature strong light-matter cou-

- pling in three dimensional terahertz meta-atoms. *Applied Physics Letters*, **108**(10):101101, 2016.
- [109] A Tabata, J B B Oliveira, E C F da Silva, T E Lamas, C A Duarte, and G M Gusev. Excitons in undoped AlGaAs/GaAs wide parabolic quantum wells. *Journal of Physics: Conference Series*, **210**(1):012052, feb 2010.
- [110] W. Q. Chen, S. M. Wang, T. G. Andersson, and J. Thordson. Inverse parabolic quantum wells grown by molecular-beam epitaxy using digital and analog techniques. *Phys. Rev. B*, **48**:14264–14268, Nov 1993.
- [111] C. Deimert and Z.R. Wasilewski. Mbe growth of continuously-graded parabolic quantum well arrays in AlGaAs. *Journal of Crystal Growth*, **514**:103–108, 2019.
- [112] Mindaugas Karaliūnas, Evelina Dudutienė, Aurimas Čerškus, Justas Pagalys, Simona Pūkienė, Andres Udal, Renata Butkutė, and Gintaras Valušis. High precision parabolic quantum wells grown using pulsed analog alloy grading technique: Photoluminescence probing and fractional-dimensional space approach. *Journal of Luminescence*, **239**:118321, 2021.
- [113] E. Hal Bogardus and H. Barry Bebb. Bound-exciton, free-exciton, band-acceptor, donor-acceptor, and auger recombination in gaas. *Phys. Rev.*, **167**:993–1002, Dec 1968.
- [114] D. J. Lockwood and Z. R. Wasilewski. Optical phonons in $\text{Al}_x\text{Ga}_{1-x}\text{As}$: Raman spectroscopy. *Phys. Rev. B*, **70**:155202, Oct 2004.
- [115] G. Irmer, M. Wenzel, and J. Monecke. The temperature dependence of the $\text{lo}(t)$ and $\text{to}(t)$ phonons in gaas and inp. *physica status solidi (b)*, **195**(1):85–95, 1996.
- [116] J. Puustinen, J. Hilska, and M. Guina. Analysis of GaAsBi growth regimes in high resolution with respect to As/Ga ratio using stationary MBE growth. *Journal of Crystal Growth*, **511**:33–41, 2019.

- [117] S Pūkienė, M Karaliūnas, A Jasinskas, E Dudutienė, B Čechavičius, J Devenson, R Butkutė, A Udal, and G Valušis. Enhancement of photoluminescence of GaAs quantum wells by parabolic design of AlGaAs barriers. *Nanotechnology*, **30**(45):455001, aug 2019.
- [118] V K Dixit, S Porwal, S D Singh, T K Sharma, Sandip Ghosh, and S M Oak. A versatile phenomenological model for the s-shaped temperature dependence of photoluminescence energy for an accurate determination of the exciton localization energy in bulk and quantum well structures. *Journal of Physics D: Applied Physics*, **47**(6):065103, jan 2014.
- [119] Petr G. Eliseev, Piotr Perlin, Jinhyun Lee, and Marek Osiński. “Blue” temperature-induced shift and band-tail emission in InGaN-based light sources. *Applied Physics Letters*, **71**(5):569–571, 1997.
- [120] Y.P. Varshni. Temperature dependence of the energy gap in semiconductors. *Physica*, **34**(1):149–154, 1967.
- [121] R. Kudrawiec, M. Syperek, P. Poloczek, J. Misiewicz, R. H. Mari, M. Shafi, M. Henini, Y. Galvão Gobato, S. V. Novikov, J. Ibáñez, M. Schmidbauer, and S. I. Molina. Carrier localization in GaBiAs probed by photomodulated transmittance and photoluminescence. *Journal of Applied Physics*, **106**(2):023518, 2009.
- [122] Andres Udal, Reeno Reeder, E. E. Velmore, and Paul Harrison. Comparison of methods for solving the Schrodinger equation for multi-quantum well heterostructure applications. 2006.
- [123] Paul Harrison. *Quantum Wells, Wires and Dots*, pages i–xxvi. John Wiley Sons, Ltd, 2005.
- [124] Reeno Reeder, Zoran Ikonić, Paul Harrison, Andres Udal, and Enn Velmore. Laterally pumped GaAs/AlGaAs quantum wells as sources of broadband terahertz radiation. *Journal of Applied Physics*, **102**(7):073715, 2007.

REFERENCES

- [125] E.O. Gobel, J. Feldmann, and G. Peter. Non-equilibrium carrier kinetics in quantum wells. *Journal of Modern Optics*, **35**(12):1965–1977, 1988.
- [126] E. Kuokstis, J. Zhang, M.-Y. Ryu, J. W. Yang, G. Simin, M. Asif Khan, R. Gaska, and M. S. Shur. Localization of carriers and polarization effects in quaternary AlInGaN multiple quantum wells. *Applied Physics Letters*, **79**(26):4375–4377, 2001.
- [127] M.-A. Pinault and E. Tournié. On the origin of carrier localization in GaInNAs/GaAs quantum wells. *Applied Physics Letters*, **78**(11):1562–1564, 2001.
- [128] Mindaugas Karaliunas, Edmundas Kuokstis, Shao-Ying Ting, Jeng-Jie Huang, and C. C. Yang. Temperature dependent double blueshift of photoluminescence peak position in MgZnO epitaxial layers. *Journal of Applied Physics*, **116**(12):123501, 2014.
- [129] J Kopaczek, W M Linhart, M Baranowski, R D Richards, F Bastiman, J P R David, and R Kudrawiec. Optical properties of GaAsBi/GaAs quantum wells: Photoreflectance, photoluminescence and time-resolved photoluminescence study. *Semiconductor Science and Technology*, **30**(9):094005, jun 2015.
- [130] Matthias Pospiech and Sha Liu. *Laser Diodes, an Introduction*. University of Hannover, 2004.
- [131] D. L. Young, J. F. Geisz, and T. J. Coutts. Nitrogen-induced decrease of the electron effective mass in GaAs_{1-x}N_x thin films measured by thermomagnetic transport phenomena. *Applied Physics Letters*, **82**(8):1236–1238, 2003.

9. CURRICULUM VITAE

About the author

Simona Pūkienė was born on October 19, 1991. She pursued higher education at Vilnius University, where she obtained a Bachelor's degree in Physics with a focus on Physics of Nuclear Energy in 2014. After that, she completed a Master's degree in Physics with a specialization in Materials Science and Semiconductors Physics in 2016. From 2016 started doctoral studies in the Optoelectronics department at the Center for Physical Sciences and Technology. During her academic journey, she had the opportunity to undertake scientific internships at prestigious institutions such as the UCSB, USA, the University of Copenhagen in Denmark, the Ludwig Maximilian University of Munich and the Walter Schottky Institut at the TUM in Germany.

Apie autorę

Simona Pūkienė gimė 1991 m. spalio 19 d. Aukštąjį išsilavinimą įgijo Vilniaus universitete, kur 2014 m. jai suteiktas fizikos bakalauro laipsnis, specializacija - branduolinės energetikos fizika. Vėliau, 2016 m., baigė fizikos magistrantūros studijas, kurių specializacija - medžiagų mokslas ir puslaidininkų fizika. Nuo 2016 m. pradėjo studijas doktorantūroje Fizinių ir technologijos mokslų centro Optoelektronikos skyriuje. Akademinės kelionės metu ji turėjo galimybę atlikti mokslines stažuotes tokiose prestižinėse institucijose kaip UCSB (JAV), Kopenhagos universitetas Danijoje, Miuncheno Liudviko Maksimiliano universitetas ir TUM Walterio Schottky institutas Vokietijoje.

NOTES

NOTES

Vilniaus universiteto leidykla
Saulėtekio al. 9, III rūmai, LT-10222 Vilnius
El. p. info@leidykla.vu.lt,
www.leidykla.vu.lt
bookshop.vu.lt, journals.vu.lt
Tiražas 20 egz.